



Production of Identified Hadrons in Au+Au Collisions at $\sqrt{s_{NN}} = 54.4$ GeV and Performance Study of the Forward Tracking System at STAR

Thesis submitted in partial fulfilment of the requirements
of the degree of
Doctor of Philosophy

By

Krishan Gopal
(20173406)

Physical Science
Indian Institute of Science Education and Research (IISER) Tirupati

December 2024

Declaration

I declare that this written submission of the thesis represents my idea in my own words and where others' ideas have been included, I have adequately cited and referenced the original sources.

The work reported in this thesis is the original work/study done by me under the guidance of **Dr. Chitrasen Jena**, and this has not been submitted elsewhere for the award of any degree or diploma.

I also declare that I have adhered to all principles of academic honesty and integrity and have not misrepresented or fabricated or falsified any idea/data/fact/source in my submission.

I understand that violation of the above will call for disciplinary action by the Institute and may evoke action from the sources which have thus not been properly cited or from whom proper permission has not been obtained.

Krishan Gopal

Name of student
(20173406)



Signature of student:

Date: 18/12/2024

CERTIFICATE

I certify that the thesis with the title Production of Identified Hadrons in Au+Au Collisions at $\sqrt{s_{NN}} = 54.4$ GeV and Performance Study of the Forward Tracking System at STAR submitted by Mr. Krishan Gopal represents his original work/study, which was carried out by him at IISER Tirupati under my guidance and supervision. The work presented here or any part of it has not been included in any other thesis submitted previously for the award of any degree or diploma from any other University or Institution.

Dr. Chitrasen Jena

Name of Supervisor:

Date: 18/12/2024



Signature of Supervisor:

To My Beloved Family

Acknowledgements

Completing this thesis was made possible through the support of many individuals. I would especially like to extend my deepest gratitude to my supervisor, Dr. Chitrasen Jena, for his invaluable guidance and support throughout this journey. I am continually inspired by his unwavering dedication and commitment to excellence in his work. Dr. Jena's mentorship has enriched my academic experience and significantly contributed to my personal and professional growth.

I wish to extend my deepest gratitude to the members of my Research Advisory Committee (RAC), Prof. Bedangdash Mohanthly, Dr. Sandeep Chaterjee, and Dr. Sunil Kumar, for their invaluable guidance and the insightful discussions that have significantly enriched my PhD journey. I am also profoundly grateful to our Director, Professor Santanu Bhattacharya, and Professor Krishnarajanagar Nagappa Ganesh, our former Director at IISER Tirupati, as well as the Academic staff, Administrative staff, Medical staff, and all the daily operational staff for their unwavering support and assistance throughout this journey. Additionally, I express my sincere thanks to all the faculty members in the Physics Department at IISER Tirupati for their continuous encouragement and support.

I sincerely thank Prof. Zhangbu Xu and Dr. Zhenyu Ye for hosting me at Brookhaven National Laboratory. During my stay in 2020, despite the challenges posed by the Covid-19 pandemic, Prof. Xu generously shared insights into the operation of the STAR detector while serving as a shift leader. Additionally, I am deeply thankful to Dr. Daniel Brandenburg for his expert guidance on Forward Silicon Tracking (FST) codes. His dedication and structured approach to work were truly commendable, and his support was invaluable throughout our collaboration.

I would also like to express my appreciation to the FST group for providing me with the opportunity to contribute to and learn from the development of a new detector system.

Furthermore, I am grateful to Ms. Liz Mogavero for her assistance throughout the visa application process, as well as for her support during my stay and departure from the United States. I would also like to acknowledge the efforts of Rashmi Sinha, Linda Sinatra, and Angela Melocoton for their diligent efforts in securing a one-month visa extension for me during the challenging circumstances of the Covid-19 pandemic.

I am deeply grateful to the STAR collaboration for affording me multiple opportunities to collaborate with esteemed professionals in the field. Specifically, I extend my thanks to the conveners, both current and past, of the Light Flavor Spectra and Ultra-Peripheral Collisions (LFS-UPC) group, namely Yue-Hang Leung, Shuai Yang, Zaochen Ye, Daniel Brandenburg, Daniel Cebra, and Md Nasim, as well as all the members of LFS-UPC. Additionally, I would like to acknowledge Physics Analysis Coordinator Rongrong Ma for his valuable input in finalizing the slides for SQM-2022.

I would like to express my sincere gratitude to my seniors, Dr. Noor Alam and Dr.

Kishora Nayak, for their invaluable assistance in helping me navigate coding issues at various levels of analysis. I am also deeply thankful to my friends, both within and outside IISER Tirupati, including Dr. Jagbir Singh, Mr. Vivek Kumar Singh, Mr. Prabhupada Dixit, Mrs. Arushi Dhamija, Dr. Sanjeev Kumar Pandey, Mr. Ganesh Narayan, Dr. Saumya Gupta, Dr. Arka Bhattacharya, Dr. K. Aditya, and my close friend Dr. Souren Adhikary. I sincerely thank Dr. Ashish Pandav for his timely support and Dr. Huihui Liu for her valuable discussions and assistance during the analysis.

I extend my heartfelt gratitude to my juniors who have become good friends: Mr. Parth Rajoria, Mr. Vaishak B. R., Mr. Subham Sinha, Mr. Sachin Rathod, Mr. Mrigaraj Goswami, and Md. Adil Aman, for their companionship and engaging conversations during my PhD. I would also like to extend my thanks to Mr. Hao Huang for our fun coffee breaks and conversations about the COVID-19 pandemic and vaccine politics during our stay at BNL during the lockdown.

I am grateful to the current EHEP group members at IISER Tirupati, including Priyanshi Sinha, Rishabh Sharma, Sharang Rav Sharma, Sibaram Behera, and Santanu Prodhan, as well as the past EHEP group members Meenakshi V, Swarda Deshpande, Yukta Ajay, Preet Bhanjan Pati, Sanket Ajay Munishwar, Surya Narayana Sangitra, Omkar Vinayak Nippanikar, N. S. Chirannjeevi, Abjashree S, Tushar Ranjan Satapathy, Aman Kumar Desai, Debasish Parida, and Prabhupada Dixit. Our productive group meetings and discussions have significantly enhanced my understanding of various aspects of heavy-ion physics.

A special thanks to my junior, Mr. Rishabh Sharma. His help and support have made this journey much more manageable.

Finally, I would like to express my deepest gratitude to my parents, brothers, sister, and in-laws for their unwavering encouragement, support, and inspiration throughout my research journey. Their understanding and patience have been invaluable, especially in allowing me the time needed to complete my PhD. I owe everything to them and am profoundly grateful for their constant presence and belief in me during this significant phase of my life.

Additionally, I would like to extend my gratitude to everyone who has contributed, both knowingly and unknowingly, to the successful completion of this project.

Abstract

Quantum Chromodynamics (QCD) predicts a transition from a hadronic phase to Quark-Gluon Plasma (QGP) under extreme temperature and/or energy density conditions, which are believed to have existed shortly after the Big Bang. Experimental facilities like the Relativistic Heavy Ion Collider (RHIC) and the Large Hadron Collider (LHC) help study the deconfined state of quarks and gluons through heavy-ion collisions. This thesis aims to investigate the particle production mechanism in heavy-ion collisions at RHIC.

The thesis is divided into six chapters. The first chapter provides a brief introduction to heavy-ion collisions and the signatures of QGP. Chapter 2 details the Solenoidal Tracker at RHIC (STAR) detector, focusing on its capabilities for particle tracking and identification. Chapter 3 presents systematic measurements of bulk properties in Au+Au collisions at $\sqrt{s_{NN}} = 54.4$ GeV using the STAR detector, analyzing transverse momentum (p_T) spectra of identified hadrons (π^\pm , K^\pm , p , and \bar{p}) across various collision centralities. Chapter 4 discusses the application of the A Multi-Phase Transport (AMPT) model to study the particle production mechanism in Au+Au collisions over a wide collision energy range ($\sqrt{s_{NN}} = 7.7 - 200$ GeV). Chapter 5 focuses on the STAR forward upgrade covering a pseudo-rapidity (η) range from 2.5 to 4.0, involving simulations for the tracking efficiency of the Forward Silicon Tracker (FST) and small-strip Thin Gas Chambers (sTGC) in various configurations, including adjustments to the position resolution, radii of the silicon discs and primary vertex resolution. Chapter 6 summarizes the results and findings of the thesis.

Chapter 1: The Standard Model of particle physics provides a comprehensive framework for understanding the fundamental particles and their interactions, excluding gravity. In high-energy heavy-ion collisions at facilities like RHIC and LHC, we study the properties of strongly interacting matter. The QCD phase diagram is important for understanding the QGP medium formed in heavy-ion collisions. At high temperatures, the diagram predicts a transition from a confined phase, where quarks and gluons are bound within hadrons, to a deconfined phase, allowing them to move freely. The formation of QGP in heavy-ion collisions is established by several key signatures. One of the signatures of QGP is jet quenching, indicated by the suppression of high- p_T particles as energetic partons lose energy in the dense medium. Another signature is the observation of the number of constituent quark (NCQ) scaling of the elliptic flow (v_2), which has been interpreted as evidence of the dominance of partonic degrees of freedom in the initial stages of heavy-ion collisions. The p_T -spectra of identified hadrons helps to understand the bulk properties and freeze-out dynamics of the produced medium. Additionally, strangeness enhancement and quarkonia (e.g., J/ψ and Υ states) suppression are also some well-known signatures of QGP.

Chapter 2: The RHIC at Brookhaven National Laboratory is a premier facility for studying the fundamental properties of matter under extreme conditions. It can collide a wide range of ion species, including p, d, He, O, Al, Cu, Ru, Zr, Au, and U at energies up to 100 GeV per nucleon for heavy-ion collisions and 250 GeV per nucleon for p+p collisions, providing unique insights into the behavior of strongly interacting matter. The STAR detector includes different sub-detectors for high-precision tracking and particle identification. The Time Projection Chamber (TPC) is crucial for tracking charged particles and identifying them based on their ionization energy loss. It provides comprehensive momentum measurements and covers a large acceptance range. The Time-Of-Flight (TOF) detector complements the TPC by extending particle identification capabilities, especially for high- p_T particles, using precise timing information to determine particle velocity. Trigger detectors, such as the Zero Degree Calorimeters (ZDCs) and Beam-Beam Counters (BBCs), play a vital role in event selection and luminosity measurement. The Vertex Position Detectors (VPDs) provide an accurate determination of the collision vertex position, which is crucial for understanding the collision dynamics. The combination of versatile beam capabilities at RHIC and the advanced particle detection system at STAR makes this facility fundamental for understanding medium formation across various collision systems and energies.

Chapter 3: The study of transverse momentum spectra is crucial for understanding the properties of matter produced in heavy-ion collisions. Identified particle spectra provide valuable information about bulk properties, such as integrated particle yields (dN/dy), average transverse momentum ($\langle p_T \rangle$), particle ratios, and freeze-out properties. A comprehensive study of identified hadron spectra offers insights into the underlying dynamics and behavior of the system formed in these collisions. In this chapter, we present the systematic measurements of bulk properties of the system created in Au+Au collisions at $\sqrt{s_{NN}} = 54.4$ GeV recorded by the STAR detector at RHIC. We have studied the p_T -spectra of π^\pm , K^\pm , p , and \bar{p} at mid-rapidity ($|y| < 0.1$) for different centrality classes. Our analysis includes the measurement of dN/dy , $\langle p_T \rangle$, particle ratios, and kinetic freeze-out parameters across nine centralities in Au+Au collisions at $\sqrt{s_{NN}} = 54.4$ GeV. These results are then compared with published results from STAR ranging from 7.7 to 200 GeV. The values of dN/dy normalized by half of the average number of participating nucleons ($\langle N_{\text{part}} \rangle / 2$) for π^\pm , K^\pm , and p increase from peripheral to central collisions, while for \bar{p} , it remains nearly constant across centrality classes. The $\langle p_T \rangle$ increases from peripheral to central collisions for π^\pm , K^\pm , p , and \bar{p} indicating the effect of stronger radial flow in central collisions. The ratios π^-/π^+ and K^-/K^+ show minimal dependence on centrality, whereas the \bar{p}/p ratio decreases with centrality.

The antiparticle-to-particle ratios in the most central collisions exhibit a consistent trend with collision energy, and the latest result at $\sqrt{s_{NN}} = 54.4$ GeV aligns with previous measurements at AGS, SPS, RHIC, and LHC energies. A blast wave model is used to extract the freeze-out parameters by fitting the particle spectra. The kinetic freeze-out temperature (T_{kin}) decreases, whereas the average flow velocity ($\langle\beta\rangle$) increases from peripheral to central collisions.

Chapter 4: We have also studied the AMPT model to investigate the bulk properties of the medium produced in Au+Au collisions across a range of energies from $\sqrt{s_{NN}} = 7.7 - 200$ GeV. Both versions (default and string melting) of the AMPT model are used with three different sets of input parameters. We study the particle spectra of π^\pm , K^\pm , p , \bar{p} , K_S^0 , Λ , and ϕ to understand the particle production mechanism. In this study, Set 1 has Lund string fragmentation parameters $a = 0.55$, $b = 0.15$ GeV⁻², and parton-parton cross section $\sigma = 3$ mb. In Set 2, a is changed to 2.2 while keeping other parameters same as in Set 1, while in Set 3, both a and b are changed to 0.5 and 0.9 GeV⁻² respectively, and σ is modified to 1.5 mb. This analysis shows that the spectra of π^\pm , K^\pm , p , and \bar{p} are well described by specific parameter sets of the string melting version at higher energies and the default version at lower energies. Moreover, a specific set of input parameters of the default version accurately describes the spectra of K_S^0 , Λ , and ϕ across all energies.

Systematic effects of model parameters tend to cancel out in particle ratios. All three sets exhibit similar behavior in the centrality dependence of T_{kin} . However, none of the sets effectively capture the behavior of $\langle\beta\rangle$. The decrease in T_{kin} with increasing $\langle\beta\rangle$ observed in the model is consistent with the observation from experimental data.

Chapter 5: The STAR forward upgrade is essential for probing QCD physics across a wide range of Bjorken x . By precisely imaging gluons and sea quarks inside protons and nuclei, we aim to explore their spatial and momentum distributions, enhancing our understanding of their contributions to nucleon spin and the emergence of nuclear properties from QCD. A key focus is determining whether gluon density within nuclei saturates as energy rises and identifying the universal characteristics of gluonic matter in this state. Additionally, we try to understand how quarks transition into colorless hadrons within nuclear environments. The forward physics program at STAR explores these questions with upgrades to detectors, including a Forward Calorimeter System (FCS) and an enhanced Forward Tracking System (FTS). We studied the tracking efficiency of the forward silicon tracker by varying the spatial resolution and radius of the silicon (Si) discs. We also assessed the effect of including the primary vertex in track reconstruction. We analyzed the impact of different hit arrangements, including 3 Si discs and 4 sTGCs, on tracking efficiency as a function of p_T , η , and azimuthal angle (φ), as well as on momentum resolution,

and inverse momentum resolution. Our analysis with the STAR Simulator and PYTHIA8 explains the effect of silicon refit on momentum resolution and the relationship between primary vertex resolution and inverse momentum resolution. We also investigated the effects of adjusting the z-location of silicon discs and the reconstruction geometry, which provides insights into how disc positions influence simulation outcomes.

Chapter 6: In this chapter, we summarize the key findings from Chapters 3, 4, and 5, focusing on the physics results. Chapter 3 highlights the analysis of p_T -spectra of π^\pm , K^\pm , p , and \bar{p} in Au+Au collisions at $\sqrt{s_{NN}} = 54.4$ GeV, where $(dN/dy)/(\langle N_{\text{part}} \rangle/2)$ for π^\pm , K^\pm , and p shows centrality dependence, while \bar{p} remains nearly constant. The results show an increase in $\langle p_T \rangle$ with centrality for all particles, indicating stronger radial flow in central collisions. Additionally, T_{kin} decreases, and $\langle \beta \rangle$ increases from peripheral to central collisions. Chapter 4 discusses the use of the AMPT model to study bulk properties across energies from 7.7 to 200 GeV in Au+Au collisions. It is observed that the string melting with Set-2 accurately describes particle yields at higher energies, while the default version is more accurate at lower energies for π^\pm , K^\pm , p , and \bar{p} . Set-1 of the default version accurately describes the spectra of K_S^0 , Λ , and ϕ across all energies. The analysis shows that T_{kin} consistently decreases with increasing $\langle \beta \rangle$, in line with experimental data. Chapter 5 focuses on the role of the STAR forward upgrade in probing QCD physics, particularly in understanding gluon and sea quark distributions. We studied the tracking efficiency of the forward silicon tracker by varying the spatial resolution and radius of the silicon discs, including sTGCs and primary vertex. It was observed that tracking efficiency remains stable for spatial resolutions between 1 and 9 μm , decreases from 10 to 90 μm , and drops to zero beyond that. Additionally, while the momentum resolution remains constant at approximately 24% with increasing primary vertex resolution, the inverse momentum resolution increases and saturates for higher primary vertex resolution.

Contents

Declaration	i
Certificate	ii
Acknowledgements	iv
Abstract	vi
Contents	x
List of Figures	xiii
List of Tables	xviii
1 Introduction	1
1.1 The Standard Model of Particle Physics	1
1.2 Quantum Chromodynamics	3
1.3 Quark-Gluon Plasma (QGP)	4
1.4 QCD Phase Diagram	5
1.5 Kinematic Variables	8
1.5.1 Center-of-mass Energy (\sqrt{s})	8
1.5.2 Transverse Momentum (p_T)	9
1.5.3 Azimuthal Angle (ϕ)	9
1.5.4 Rapidity (y)	9
1.5.5 Pseudorapidity (η)	10
1.5.6 Natural unit	10
1.6 Heavy-Ion Collisions at Relativistic Energies	10
1.7 Signatures of Quark-Gluon Plasma	13
1.7.1 Particle Yields and Spectra	13
1.7.2 Anisotropic Flow	15
1.7.2.1 Directed flow (v_1)	16

1.7.2.2	Elliptic flow (v_2)	18
1.7.3	Direct Photons	19
1.7.4	Strangeness Enhancement	21
1.7.5	Quarkonia Suppression	23
1.7.6	High p_T Probes	24
1.8	Outline of the Thesis	27
2	STAR Experiment	28
2.1	The Relativistic Heavy Ion Collider	28
2.2	STAR Experiment	31
2.2.1	Time Projection Chamber (TPC)	32
2.2.1.1	Track Reconstruction in TPC	33
2.2.1.2	Particle Identification in TPC	34
2.2.2	Time-Of-Flight (TOF)	36
2.2.3	Trigger Detectors	37
2.2.3.1	Zero Degree Calorimeters (ZDC)	37
2.2.3.2	Beam-Beam Counter (BBC)	38
2.2.3.3	Vertex Position Detectors (VPD)	38
2.2.3.4	ElectroMagnetic Calorimeters (EMCs)	39
3	Identified Particle Production in Au+Au Collisions at $\sqrt{s_{NN}} = 54.4$ GeV in the STAR Experiment	42
3.1	Introduction	42
3.1.1	Data Set and Analysis Selection Criteria	43
3.1.1.1	Event Selection	43
3.1.1.2	Track Selection	44
3.1.1.3	Centrality Selection	45
3.2	Particle Identification	45
3.3	Correction Factors	48
3.3.1	Track Energy-Loss Correction	49
3.3.2	TPC Tracking Efficiency	50
3.3.3	Pion Feed-down Correction	51
3.3.4	Proton Background Correction	51
3.4	Systematic Uncertainties	53
3.5	Results and Discussions	56
3.5.1	Transverse Momentum Spectra	56
3.5.2	Average Transverse Momentum ($\langle p_T \rangle$)	58
3.5.3	Particle Yields (dN/dy)	59
3.5.4	Particle Ratios	61

3.5.5	Freeze-out Properites	64
3.6	Summary	66
4	Energy dependence of particle production in Au+Au collisions using AMPT model	69
4.1	Introduction	69
4.2	Analysis Details	73
4.3	Results and Discussion	74
5	STAR Forward Upgrade	85
5.1	Introduction	85
5.2	Forward Upgrade	89
5.2.1	Forward Tracking System	90
5.2.1.1	Forward Silicon Tracker	90
5.2.1.2	small-strip Thin Gap Chambers	91
5.2.2	Forward Calorimeter System	92
5.3	Details of Tracking Algorithm	93
5.3.1	Track reconstruction	94
5.4	Analysis Method	97
5.5	Results and Discussion	99
5.5.1	Position Resolution Study	99
5.5.2	Tracking Efficiency	101
5.6	Summary	107
6	Conclusion	109
	Summary and Outlook	112
	References	112

List of Figures

3.1	Distribution of the z-component of the vertex (V_z) (left panel) and the V_y versus V_x distributions (right panel) after applying all event cuts in Au+Au collisions at $\sqrt{s_{NN}} = 54.4$ GeV in the STAR experiment.	44
3.2	The distribution of charged particle multiplicity (not corrected for efficiency and acceptance) measured by the TPC within $ \eta < 0.5$ in Au+Au collisions at $\sqrt{s_{NN}} = 54.4$ GeV in the STAR experiment. The vertical lines represent the centrality selection criteria employed. Errors are statistical.	46
3.3	The distribution of specific energy loss ($\langle dE/dx \rangle$) of charged particles as a function of momentum-to-charge ratio (p/q) obtained from the TPC in Au+Au collisions at $\sqrt{s_{NN}} = 54.4$ GeV. The curves represent the expected mean value of dE/dx for the corresponding particle.	47
3.4	The z_π , z_K , and z_p distributions of π^+ , K^+ , and p at mid-rapidity ($ y < 0.1$) for p_T range 0.40-0.45 GeV/c in 0–5% centrality from TPC in Au+Au collisions at $\sqrt{s_{NN}} = 54.4$ GeV. The curves represent Gaussian fits corresponding to contributions from pions, electrons, kaons, and protons. The uncertainties are purely statistical.	47
3.5	The z_π , z_K , and z_p distributions of π^+ , K^+ , and p at mid-rapidity ($ y < 0.1$) for p_T range 0.60-0.65 GeV/c in 0–5% centrality from TPC in Au+Au collisions at $\sqrt{s_{NN}} = 54.4$ GeV. The curves represent Gaussian fits corresponding to contributions from pions, electrons, kaons, and protons. The uncertainties are purely statistical.	48
3.6	We compare the DCA, nHits, and nHitsdEdx distributions between reconstructed embedding tracks and real tracks, focusing on the π^+ embedding sample in Au+Au collisions at $\sqrt{s_{NN}} = 54.4$ GeV. The errors considered are purely statistical.	49
3.7	The difference between the reconstructed momentum (p_T^{REC}) and the Monte Carlo generated momentum (p_T^{MC}) is plotted as a function of p_T^{REC} for pions (left panel), kaons (middle panel), and protons (right panel) in Au+Au collisions at $\sqrt{s_{NN}} = 54.4$ GeV. These plots show the statistical errors only.	50

3.8	Track reconstruction efficiency and acceptance as a function of p_T^{MC} for reconstructed pions (left), kaons (middle), and protons (right) derived from embedding in Au+Au collisions at $\sqrt{s_{\text{NN}}} = 54.4$ GeV. The lines represent the functional fit to the data, with statistical errors being depicted.	51
3.9	The total background fraction to the yield of pions as a function of p_T , illustrating contributions from weak decay and muon contamination in Au+Au collisions at $\sqrt{s_{\text{NN}}} = 54.4$ GeV. The errors are statistical only.	52
3.10	The DCA distributions of protons and antiprotons for $0.45 < p_T$ (GeV/c) < 0.50 and $0.50 < p_T$ (GeV/c) < 0.55 in the 0–5% centrality range in Au+Au collisions at $\sqrt{s_{\text{NN}}} = 54.4$ GeV. The dashed curve represents the fit to the proton background, the dotted histogram depicts the antiproton DCA distribution scaled by $r_{\bar{p}}/p$, and the solid histogram shows the fit to the proton DCA distribution. The errors are statistical only.	53
3.11	The DCA distributions of protons and antiprotons for $0.85 < p_T$ (GeV/c) < 0.90 and $0.90 < p_T$ (GeV/c) < 0.95 in the 0–5% centrality range in Au+Au collisions at $\sqrt{s_{\text{NN}}} = 54.4$ GeV. The dashed curve represents the fit to the proton background, the dotted histogram depicts the antiproton DCA distribution scaled by $r_{\bar{p}}/p$, and the solid histogram shows the fit to the proton DCA distribution. The errors are statistical only.	54
3.12	The total background fraction to the yield of proton as a function of p_T , for different centralities in Au+Au collisions at $\sqrt{s_{\text{NN}}} = 54.4$ GeV. The errors are statistical only.	54
3.13	p_T spectra of π^\pm , K^\pm , and $p(\bar{p})$ measured at mid-rapidity ($ y < 0.1$) in Au+Au collisions at $\sqrt{s_{\text{NN}}} = 54.4$ GeV in STAR using TPC. Spectra are plotted for nine centrality classes, with some scaled for clarity. Uncertainties represent total systematic and statistical uncertainties added in quadrature, primarily dominated by systematic errors.	57
3.14	p_T spectra of π^\pm , K^\pm , and $p(\bar{p})$ measured at mid-rapidity ($ y < 0.1$) in Au+Au collisions at $\sqrt{s_{\text{NN}}} = 54.4$ GeV in STAR using TPC and TOF. Spectra are plotted for nine centrality classes, with some scaled for clarity. Fits to the p_T spectra are shown for 30-40% centrality using a Levy function for pions and kaons and a double exponential for (anti)protons. Uncertainties represent total systematic and statistical uncertainties added in quadrature, primarily dominated by systematic errors.	57

3.16	dN/dy of π^+ , π^- , K^+ , K^- , p , and \bar{p} scaled by $0.5 \times \langle N_{\text{part}} \rangle$ as a function of $\langle N_{\text{part}} \rangle$ for Au+Au collisions at $\sqrt{s_{\text{NN}}} = 54.4$ GeV. The results are compared with Au+Au collisions at $\sqrt{s_{\text{NN}}} = 200$ GeV, along with dN/dy values at various other beam energies from STAR [108, 113, 115]. The uncertainties represent total systematic and statistical uncertainties added in quadrature.	60
3.17	The scaled yields, dN/dy , of π^+ , π^- , K^+ , K^- , p , and \bar{p} , normalized by $\langle N_{\text{part}} \rangle / 2$ are presented as a function of $\sqrt{s_{\text{NN}}}$ for Au+Au collisions at $\sqrt{s_{\text{NN}}} = 54.4$ GeV. These results are compared with data from AGS, SPS, and RHIC at various collision energies. The statistical and systematic uncertainties have been combined in quadrature [108, 113, 115].	60
3.18	Ratios of π^-/π^+ , K^-/K^+ , and \bar{p}/p as a function of p_T in 0-5% central Au+Au collisions at $\sqrt{s_{\text{NN}}} = 54.4$ GeV, measured by the STAR detector at RHIC.	61
3.19	Ratios of π^-/π^+ , K^-/K^+ , and \bar{p}/p as a function of $\langle N_{\text{part}} \rangle$ in Au+Au collisions at $\sqrt{s_{\text{NN}}} = 54.4$ GeV. The results are compared with Au+Au collisions at $\sqrt{s_{\text{NN}}} = 200$ GeV, along with corresponding values for various other beam energies from STAR. The uncertainties represent total systematic and statistical uncertainties added in quadrature.	62
3.20	Ratios of K^+/π^+ , K^-/π^- , p/π^+ , and \bar{p}/π^- as a function of $\langle N_{\text{part}} \rangle$ in Au+Au collisions at $\sqrt{s_{\text{NN}}} = 54.4$ GeV. The results are compared with Au+Au collisions at $\sqrt{s_{\text{NN}}} = 200$ GeV, along with corresponding values for various other beam energies from STAR. The uncertainties represent total systematic and statistical uncertainties added in quadrature.	63
3.21	Ratios of π^-/π^+ , K^-/K^+ , and \bar{p}/p at midrapidity ($ y < 0.1$) in central 0-5% Au+Au collisions at $\sqrt{s_{\text{NN}}} = 54.4$ GeV, compared to previous results from AGS [133-139], SPS [140-143], RHIC [113, 144], and LHC [145]. AGS results correspond to 0-5%, SPS to 0-7%, top RHIC to 0-5% (62.4 and 200 GeV) and 0-6% (130 GeV), and LHC to 0-5% central collisions. Errors shown are the quadrature sum of statistical and systematic uncertainties.	64
3.22	Simultaneous blast-wave fit to the p_T spectra of π^\pm , K^\pm , $p(\bar{p})$ in Au+Au collisions at $\sqrt{s_{\text{NN}}} = 54.4$ GeV in the 0-5% centrality class within $ y < 0.1$. The uncertainties represent the total systematic and statistical uncertainties added in quadrature.	66
3.23	The variation of kinetic freeze-out temperature (T_{kin}) with the mean transverse velocity ($\langle \beta \rangle$) in Au+Au collisions at $\sqrt{s_{\text{NN}}} = 54.4$ GeV. The uncertainties shown include both total systematic and statistical uncertainties added in quadrature.	67

4.1	Configuration of the Default (Left) and String Melting (Right) AMPT model [150].	73
4.2	Invariant yield of π^+ (upper row), K^+ (middle row) and proton (lower row) as a function of p_T for 0 – 5% centrality in Au+Au collision at $\sqrt{s_{NN}} = 7.7, 27, 39, 62.4$ and 200 GeV using AMPT-Def versions. The AMPT results are compared with the corresponding experimental data which is fitted with a Levy function [161]. The ratio of data to fit function is also shown in the lower panels for each pad.	74
4.3	Invariant yield of π^+ (upper row), K^+ (middle row) and proton (lower row) as a function of p_T for 0 – 5% centrality in Au+Au collision at $\sqrt{s_{NN}} = 7.7, 27, 39, 62.4$ and 200 GeV using AMPT-SM versions. The AMPT results are compared with the corresponding experimental data which is fitted with a Levy function [161]. The ratio of data to fit function is also shown in the lower panels for each pad.	75
4.4	Invariant yield of K_S^0 (upper row), Λ (middle row) and ϕ (lower row) as a function of p_T for most central events in Au+Au collision at $\sqrt{s_{NN}} = 7.7, 27, 39, 62.4$ and 200 GeV are shown in each column using AMPT-Def. The ratio of data to fit function is also shown in the lower panels for each pad.	76
4.5	Invariant yield of K_S^0 (upper row), Λ (middle row) and ϕ (lower row) as a function of p_T for most central events in Au+Au collision at $\sqrt{s_{NN}} = 7.7, 27, 39, 62.4$ and 200 GeV are shown in each column using AMPT-SM. The ratio of data to fit function is also shown in the lower panels for each pad.	77
4.6	Energy dependence of $(dN/dy)/(\langle N_{part} \rangle/2)$ for particle (π^+, K^+, p) and anti-particle (π^-, K^-, \bar{p}) for central (0-5%) Au+Au collisions using AMPT-Def (a) and AMPT-SM (b). The AMPT results shown in open markers are compared with the corresponding experimental data (solid marker).	78
4.7	Energy dependence of $(dN/dy)/(\langle N_{part} \rangle/2)$ for $K_S^0, \Lambda, \phi,$ and $\bar{\Lambda}$ for central Au+Au collisions using AMPT-Def (a) and AMPT-SM (b). The AMPT results shown in open markers are compared with the corresponding experimental data (solid marker).	79
4.8	$\langle m_T \rangle - m_0$ of $\pi^\pm, K^\pm, p,$ and \bar{p} as a function of $\sqrt{s_{NN}}$ at midrapidity ($ y < 0.1$). Results are presented for 0-5% central Au+Au collisions using AMPT-Def (a) and AMPT-SM (b). The AMPT results shown in open markers are compared with the corresponding experimental data (solid marker).	80

4.9	$\langle m_T \rangle - m_0$ of K_S^0 , Λ , ϕ , and $\bar{\Lambda}$ as a function of $\sqrt{s_{NN}}$ at midrapidity. Results are presented for 0–5% central Au+Au collisions using AMPT-Def (a) and AMPT-SM (b). The AMPT results shown in open markers are compared with the corresponding experimental data (solid marker).	80
4.10	π^-/π^+ , K^-/K^+ , and \bar{p}/p ratios at midrapidity ($ y < 0.1$) in central 0–5% Au+Au collisions at $\sqrt{s_{NN}} = 7.7, 27, 39, 62.4$ and 200 GeV using AMPT-Def (upper panel) and AMPT-SM (lower panel). The AMPT results shown in open markers are compared with the published experimental data (solid marker).	81
4.11	Centality dependence of kinetic freeze-out temperature (T_{kin} in MeV) in different collision energies for three different Sets in Au+Au collisions using AMPT.	82
4.12	Centality dependence of $\langle \beta \rangle$ in different collision energies for three different Sets in Au+Au collisions using AMPT.	83
4.13	Variation of T_{kin} with $\langle \beta \rangle$ for three different Sets for different collision energies. The centrality increases from left to right for a given energy. . . .	83
5.9	Schematic of MC track passing through 3 Si and four sTGC. MC (Truth) and Reconstructed (Reco.) hits are shown.	97
5.10	Flowchart summarizing the simulation and analysis pipeline.	99
5.11	Tracking efficiency with 3 silicon disks and no sTGC layers. σ_X and σ_Y values are given in mm.	100
5.12	Tracking efficiency with 3 silicon disks and 4 sTGC layers. σ_X and σ_Y values are given in mm.	101
5.13	Summary plot for position resolution study.	102
5.14	QA plots for tracking using four sTGC hits	102
5.15	Tracking efficiency of sTGCs as a function of p_T , η , and ϕ using the STAR simulator (STAR SIM).	104
5.16	Tracking efficiency of sTGCs as a function of p_T , η , and ϕ using the PYTHIA8.	104
5.17	Momentum ($\sigma(p_T)$) and inverse momentum ($\sigma(1/p_T)$) resolution.	105
5.18	Momentum ($\sigma(p_T)$) and inverse momentum ($\sigma(1/p_T)$) resolution as a function of radius values of Silicon discs.	105
5.19	Momentum ($\sigma(p_T)$) and inverse momentum ($\sigma(1/p_T)$) resolution as a function of primary vertex resolution.	106
5.20	combined Z-distribution of Si discs.	106

List of Tables

1.1	Time, length, and mass in natural units.	10
2.1	Overview of RHIC Operations [70].	29
3.1	Trigger Id and Event cuts	44
3.2	Track Selection Criteria for Tracks in Au+Au Collisions at $\sqrt{s_{NN}} = 54.4$ GeV	44
3.3	Default and modified values of event and track cuts to measure systematic uncertainties.	55
4.1	Values of a and b related to the Lund string fragmentation function, as well as α_s and μ , significant for the parton scattering cross section [160].	73

List of Papers/Proceedings

- *1. Production of pions, kaons, and (anti-)protons in Au+Au collisions at $\sqrt{s_{NN}} = 54.4$ GeV at RHIC,
Krishan Gopal (for the STAR Collaboration), EPJ Web of Conf. 276 (2023) 03009.
- *2. Production of identified hadrons in Au+Au collisions at $\sqrt{s_{NN}} = 54.4$ GeV at RHIC,
Krishan Gopal (for the STAR Collaboration), DAE Symp. Nucl. Phys. 66 (2023) 918-919.
- *3. Production of identified hadrons in Au+Au collisions Identified hadron production at mid-rapidity in Au+Au collisions at $\sqrt{s_{NN}} = 54.4$ GeV at STAR,
Krishan Gopal (for the STAR Collaboration), Springer Proc. Phys. 304 (2024) 786-788.
- 4. Effect of nuclear structure on particle production in relativistic heavy-ion collisions using a multiphase transport model,
P. Sinha, V. Bairathi, **K. Gopal**, C. Jena, and S. Kabana, Phys. Rev. C 108, 024911 (2023).

Papers under review (as a primary author):

- *1. **Paper title:** Identified charged hadron production in Au+Au collisions at $\sqrt{s_{NN}} = 54.4$ GeV with STAR detector,
Authors: **Krishan Gopal** *et al.*, (STAR Collaboration)
Target Journal: Phys. Rev. C
- *2. Energy dependence of particle production in Au+Au collisions at $\sqrt{s_{NN}} = 7.7-200$ GeV using a multiphase transport model,
Krishan Gopal, Chitrasen Jena, and Kishora Nayak,
[arXiv:2406.13520](https://arxiv.org/abs/2406.13520) [nucl-th]
- 3. System size dependence of thermodynamic variables at kinetic freeze-out in high-energy collisions using the Tsallis distribution,
Rishabh Sharma, **Krishan Gopal**, Sharang Rav Sharma, and Chitrasen Jena,
[arXiv:2401.13629](https://arxiv.org/abs/2401.13629) [hep-ph]

Selected List of Publications/Preprints as a part of STAR Collaboration:

1. K^*0 production in Au+Au collisions at $\sqrt{s_{NN}} = 7.7, 11.5, 14.5, 19.6, 27$ and 39 GeV from RHIC beam energy scan,
M. Abdallah et al. (STAR Collaboration), Phys. Rev. C 107, 034907 (2023).
2. Beam Energy Dependence of Triton Production and Yield Ratio ($N_t \times N_p/N_{2d}$) in Au+Au Collisions at RHIC,
M. I. Abdulhamid et al. (STAR Collaboration), Phys. Rev. Lett. 130, 202301 (2023).
3. Pion, kaon, and (anti)proton production in U+U collisions at $\sqrt{s_{NN}} = 193$ GeV measured with the STAR detector,
M. S. Abdallah et al. (STAR Collaboration), Phys. Rev. C 107, 024901 (2023).
4. Azimuthal anisotropy measurement of (multi-)strange hadrons in Au+Au collisions at $\sqrt{s_{NN}} = 54.4$ GeV,
M. S. Abdallah et al. (STAR Collaboration), Phys. Rev. C 107, 024912 (2023).
5. Centrality and transverse-momentum dependence of higher-order flow harmonics of identified hadrons in Au+Au collisions at $\sqrt{s_{NN}} = 200$ GeV,
M. S. Abdallah et al. (STAR Collaboration), Phys. Rev. C 105, 064911 (2022).
6. Collision-System and Beam-Energy Dependence of Anisotropic Flow Fluctuations,
M. S. Abdallah et al. (STAR Collaboration), Phys. Rev. Lett. 129, 252301 (2022).
7. Light nuclei collectivity from $\sqrt{s_{NN}} = 3$ GeV Au+Au collisions at RHIC,
M. S. Abdallah et al. (STAR Collaboration), Phys. Lett. B 827, 136941 (2022).
8. Disappearance of partonic collectivity in $\sqrt{s_{NN}} = 3$ GeV Au+Au collisions at RHIC,
M. S. Abdallah et al. (STAR Collaboration), Phys. Lett. B 827, 137003 (2022).
9. Azimuthal anisotropy measurements of strange and multi-strange hadrons in U+U collisions at $\sqrt{s_{NN}} = 193$ GeV at the BNL Relativistic Heavy Ion Collider,

M. Abdallah et al. (STAR Collaboration), Phys. Rev. C 103, 064907 (2021).

10. Beam-energy dependence of the directed flow of deuterons in Au+Au collisions,
J. Adam et al. (STAR Collaboration), Phys. Rev. C 102, 044906 (2020).

11. Bulk Properties of the System Formed in Au+Au Collisions at $\sqrt{s_{NN}} = 14.5$ GeV
at STAR,
J. Adam et al. (STAR Collaboration), Phys. Rev. C 101, 024905 (2020).

12. Strange hadron production in Au+Au collisions at $\sqrt{s_{NN}} = 7.7, 11.5, 19.6, 27,$ and
39 GeV,
J. Adam et al. (STAR Collaboration), Phys. Rev. C 102, 034909 (2020).

(*) indicates papers on which this thesis is based.

Chapter 1

Introduction

The study of the fundamental constituents of matter and their interactions has always been a significant and fascinating topic. In the beginning, the atom was widely recognized as the fundamental unit of all matter. Yet, the search for fundamental particles began with the discovery of the electron by J.J. Thomson in 1897 [1]. The discovery of the proton by Ernest Rutherford in 1917 [2], followed by the discovery of the neutron by James Chadwick in 1932 [3], profoundly changed our understanding of matter. These findings have led to the understanding that atoms consist of protons, neutrons, and electrons. However, the pursuit of greater understanding continued.

In the 1960s, theoretical physicists Murray Gell-Mann and George Zweig independently introduced the concept of quarks. According to their proposal, neutrons and protons, previously thought of as indivisible, were revealed to be bound states of quarks and gluons. These quarks and gluons are collectively referred to as partons. Experimental evidence has substantiated the idea that neutrons and protons are not the ultimate, indivisible particles we once thought them to be [4]. This ongoing journey of discovery underscores the dynamic nature of our understanding of the fundamental constituents of matter. This chapter sets up the basic understanding of heavy-ion collisions. Starting with a look at the essential components according to the Standard Model, the discussion moves on to explore the creation and characteristics of Quark-Gluon Plasma—a unique state of matter resulting from these collisions.

1.1 The Standard Model of Particle Physics

In the domain of particle physics, the Standard Model provides a unified framework for the study of the properties of elementary particles as well as the dynamics of their interactions. The groundbreaking theory, developed by Glashow, Salam, and Weinberg, effectively combines and defines the three basic forces of nature—weak, electromagnetic, and strong—while excluding gravity. Consequently, it provides a deep understanding of

these fundamental interactions [5–7].

The Standard Model of particle physics proposes that there are three generations of quarks and three generations of leptons. Each of the three quark generations includes two quarks: up (u) and down (d) in the first generation, charm (c) and strange (s) in the second, and top (t) and bottom (b) in the third, following that sequence. The three lepton generations, consisting of the electron (e), muon (μ), and tau (τ), are each accompanied by their respective neutrino counterparts (ν_e, ν_μ, ν_τ). For every elementary particle, there exists a corresponding antiparticle that possesses an identical mass but exhibits quantum numbers with opposite values.

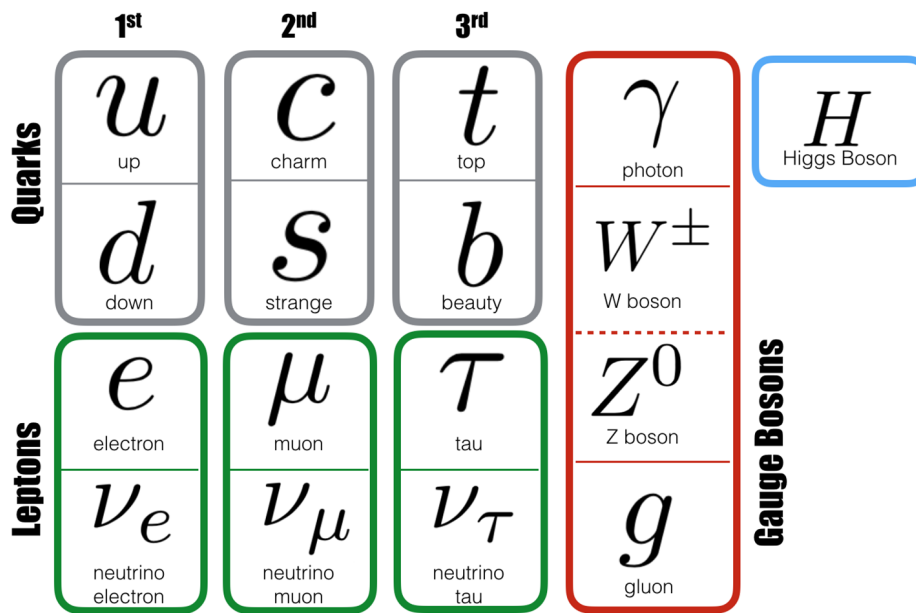


Figure 1.1: The elementary particles of the Standard Model [8].

For each of the three fundamental forces of nature—strong, electromagnetic, and weak—there exists a distinct set of force carriers. Gluons act as carriers for the strong force, photons for the electromagnetic force, and W^\pm and Z bosons for the weak force. Additionally, the graviton has been proposed as the mediator of the gravitational force based on a similar reasoning, though it is not incorporated into the Standard Model. Quarks are fundamental particles classified as fermions, participating in strong, weak, and electromagnetic interactions. Quarks interact with each other through the exchange of bosons, which are particles that mediate the fundamental forces of nature. Within the Standard Model, the incorporation of the Higgs boson [9–11], initially proposed by P. W. Higgs, F. Englert, and R. Brout in 1964, has advanced the field of physics. The experimental confirmation of this particle on July 4, 2012, by the ATLAS [12] and CMS [13] experiments, has contributed to a more thorough understanding of elementary particles. The Higgs boson plays a crucial role in the generation of mass for elementary

particles. Figure 1.1 provides an illustrative representation of the complete set of fundamental building blocks of matter. Quarks are intrinsically confined and are never observed in free states. Rather, they are always found in bound states within composite particles known as hadrons. Hadrons, in turn, can be categorized into two primary classes based on their quark content: mesons, which consist of a quark and an anti-quark pair, and baryons, which are formed from three quarks.

1.2 Quantum Chromodynamics

The theory that describes the interactions between quarks and gluons is known as quantum chromodynamics (QCD). QCD governs the strong interaction, which is the fundamental force that binds quarks together to form hadrons. QCD possesses three distinct color charges that are analogous to the electric charges of QED (Quantum Electrodynamics). Unlike QED, which has two charges, QCD has three types of charges, which are referred to as red, green, and blue, and are carried by quarks and gluons. QCD exhibits two key properties, namely confinement and asymptotic freedom [14, 15]. The understanding of these properties can be gained by analyzing the expression of the strong interaction coupling constant, α_s :

$$\alpha_s(Q^2) \approx \frac{12\pi}{(33 - 2N_f) \ln(Q^2/\Lambda_{\text{QCD}}^2)}, \quad (1.1)$$

where Q^2 is the momentum transfer, N_f is the number of quark flavors, and Λ_{QCD} is the QCD scale parameter. Experimental scattering studies provide a typical value of Λ , which is around 200 MeV. The values of α_s have been derived from various experimental observations and compared with the predictions of perturbative QCD (pQCD). The success of pQCD in predicting and explaining diverse phenomena observed in experiments is evident from the results shown in Figure 1.2.

Quark confinement, also known as “Confinement” can be explained as a phenomenon in QCD that refers to the inability of quarks to exist as isolated particles. Instead, quarks are always bound together within hadrons, which are composite particles made up of quarks and gluons. This means that any isolated quark will experience an infinite force of attraction that prevents it from moving away from other quarks. We can understand from the Eq. 1.1 that at low momentum transfer scales, α_s becomes large, indicating that the strong force becomes stronger at small distance scales. Whereas at high momentum transfer scales ($Q \gg 1$ GeV), α_s becomes smaller, indicating that the strong force becomes weaker at larger distance scales. This phenomenon is known as “Asymptotic Freedom”. It refers to the transition from a confined state to a deconfined state, in which quarks are free to move and interact with one another. David J. Gross, H. David Politzer, and

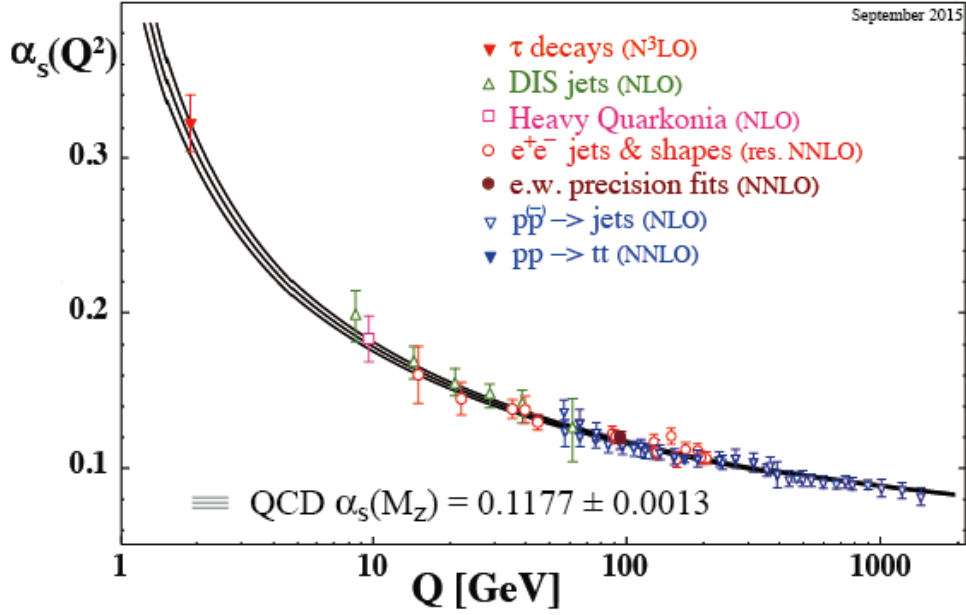


Figure 1.2: Individual measurements for the strong coupling constant $\alpha_s(Q^2)$ as a function of energy scale Q . The Figure is taken from Ref. [16].

Frank Wilczek were awarded the Nobel Prize in 2004 [†] for their discovery of asymptotic freedom, which they made in 1973 and 1974.

1.3 Quark-Gluon Plasma (QGP)

The concept of asymptotic freedom in QCD, which describes how the strength of the strong interaction decreases at high energies, led to the development of the idea of a new phase of matter known as the Quark-Gluon Plasma (QGP). In 1974, T.D. Lee proposed that at very high energies and temperatures, quarks and gluons could exist in a deconfined state, forming a plasma-like state of matter where quarks and gluons are no longer confined within hadrons. This transition is believed to occur at high temperatures (~ 156 MeV) or densities ($1 \text{ GeV}/fm^3$), such as those present in the early universe or in the cores of neutron stars [17, 18].

The QGP can also be created in heavy-ion collisions at ultra-relativistic energies. Experimental studies of the QGP have revealed its unique properties, such as extremely low viscosity, similar to that of an ideal fluid [19], and its strong interactions with other particles. The study of the QGP has thus become an important area of research in nuclear and particle physics, and it has led to a deeper understanding of the properties of quarks and the strong interaction.

[†]<https://www.aps.org/publications/apsnews/200412/nobel.cfm>

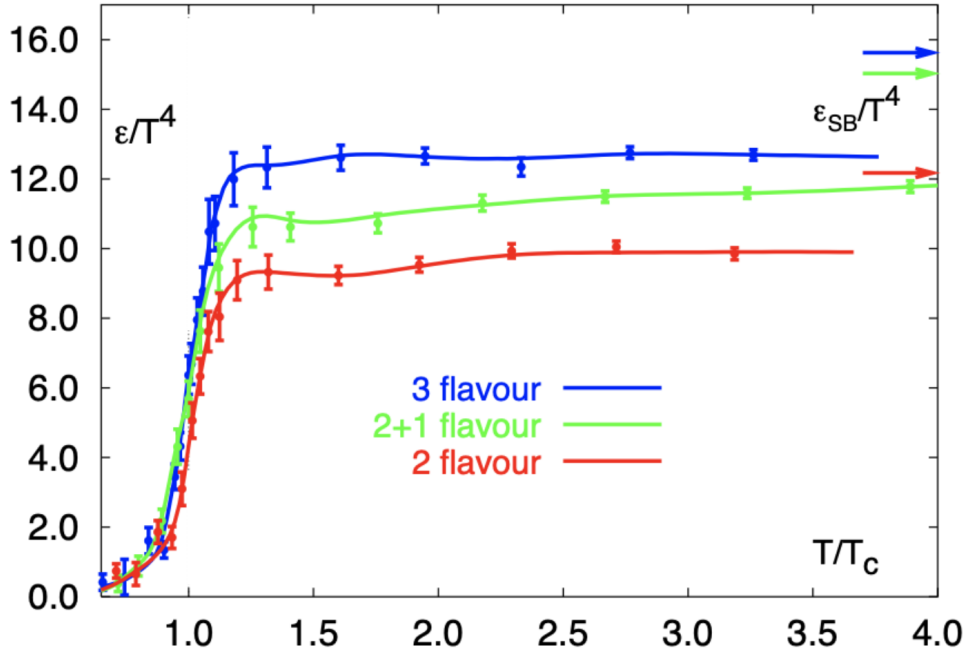


Figure 1.3: The energy density ε/T^4 as a function of temperature scaled by the critical temperature (T_c) is calculated using lattice QCD. The arrows indicating the Stefan-Boltzmann limits [20].

1.4 QCD Phase Diagram

Lattice QCD calculations provide numerical simulations of QCD at finite temperatures and densities, allowing the study of the properties of matter at extreme conditions. These simulations have shown that at temperatures above a certain critical temperature, known as the QCD phase transition temperature (T_c), there is a transition from a confined phase to a deconfined phase, in which quarks and gluons are no longer confined within hadrons and can move freely.

In Figure 1.3, the vertical axis represents the ratio of the energy density (ε) to the fourth power of the temperature (ε/T^4), while the horizontal axis represents the ratio of the temperature to the critical temperature (T/T_c) [20]. The right-hand side arrows in the plot indicate the Stefan-Boltzmann limit, which represents the energy density of a gas of massless particles in the high-temperature limit.

The mathematical expression for the energy density of a gas of massless hadrons from thermodynamic calculations is given by:

$$\varepsilon_{HG} = g \frac{\pi^2}{30} T^4, \quad (1.2)$$

where ε_{HG} is the energy density, T is the temperature, and g is the effective number of massless degrees of freedom of the hadron gas. At temperatures below the critical temperature T_c , the energy density of the system is dominated by hadrons and their

interactions, resulting in a low energy density. As the temperature is increased above T_c , the energy density of the system begins to rise rapidly, indicating the formation of the QGP. The transition is characterized by a rapid increase in the energy density, followed by a plateau at a high energy density, indicating the formation of the QGP. This behavior is consistent with the lattice QCD calculations and provides strong evidence for the existence of the QGP.

For a system consisting of only massless pions, which are found in 3 states, the expression for the energy density of the Hadron Gas (HG) consisting of only massless pions can be written as:

$$\varepsilon_{HG} = 3 \frac{\pi^2}{30} T^4 \quad (1.3)$$

This expression tells us that the energy density of the HG is proportional to the T^4 , with a constant of proportionality of $3\pi^2/30$. For the QGP medium of quarks and gluons, the number of degrees of freedom is considerably higher than for the HG. In the QGP, there are two types of degrees of freedom: quarks and gluons. Quarks come in three “colors” (red, green, and blue) and two “spins” (up and down). Gluons come in eight “colors” and two “spins”. In addition to these degrees of freedom, there are also “flavors” of quarks, which contribute an additional factor of n_f to the energy density.

The expression for the energy density of the QGP can be written as:

$$\begin{aligned} \varepsilon_{QGP} &= 2_{\text{spin}} \times 8_{\text{colors}} \times \frac{\pi^2}{30} T^4 + 2_{q\bar{q}} \times 2_{\text{spin}} \times 3_{\text{colors}} \times n_f \times \frac{7}{8} \frac{\pi^2}{30} T^4 \\ &= \left(16 + \frac{21}{2} n_f \right) \frac{\pi^2}{30} T^4 \end{aligned} \quad (1.4)$$

This expression shows that the energy density of the QGP is also proportional to the T^4 , with a constant of proportionality that is much larger than the HG. The first term in the equation corresponds to the energy density of gluons, while the second term corresponds to the energy density of quarks and antiquarks.

The ratio of energy density to the fourth power of temperature is a measure of the number of degrees of freedom in the thermodynamic system. As the temperature of the system increases, the energy density increases and the value of ε/T^4 increases as well. At the critical temperature, there is a sharp increase in ε/T^4 , which indicates a transition to a new phase of matter called the Quark-Gluon-Plasma (QGP). In the QGP phase, quarks and gluons become the relevant degrees of freedom instead of the hadrons that were present in the initial state. During this phase transition, the pressure in the system changes more slowly than the energy density, meaning that the pressure gradient in the system is reduced. This behavior is due to the fact that the pressure of the system is

related to the momentum distribution of the particles, which changes less rapidly than the energy density during the QGP phase transition. In summary, the number of degrees of freedom is considerably higher for the QGP medium than for the HG. This is reflected in the much higher energy density of the QGP, which is proportional to the T^4 and is dominated by the contributions from quarks and gluons.

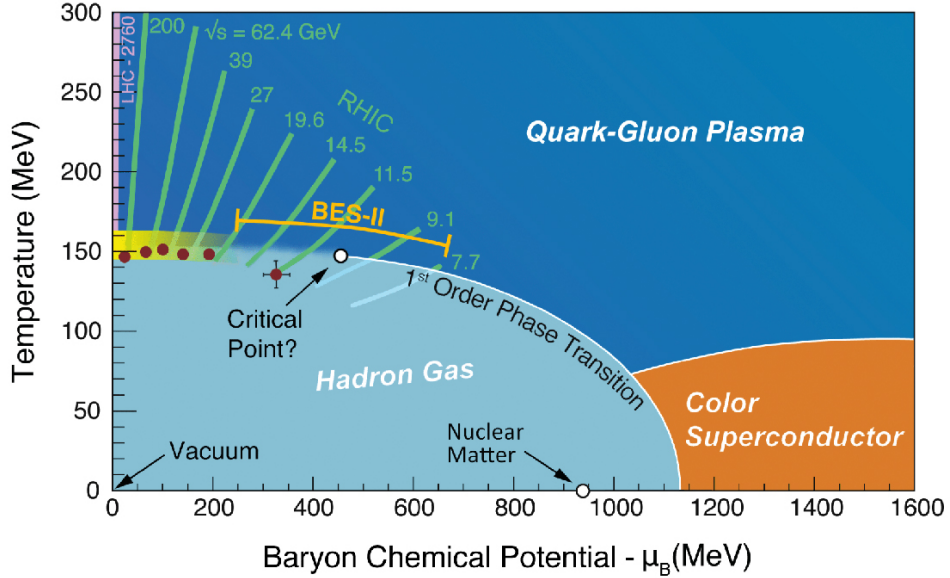


Figure 1.4: The phase diagram schematically illustrating the transition between the confined hadron state and the deconfined quark-gluon plasma state [21].

A theoretical phase diagram, known as the QCD phase diagram, was proposed to understand the behavior of nuclear matter at relativistic speeds. This phase diagram is used to describe the various phases of nuclear matter based on its temperature and density. Lattice QCD calculations and experiments conducted at the Large Hadron Collider (LHC) and the Relativistic Heavy Ion Collider (RHIC) have been used to map this phase diagram.

The QCD phase diagram illustrates the various phases of nuclear matter at different temperatures and baryon chemical potentials (μ_B). At low temperatures and densities, nuclear matter exists in the hadronic phase, where quarks are confined within hadrons. At high temperatures and/or densities, the QCD phase transition leads to QGP, where quarks and gluons are deconfined.

Figure 1.4 presents the QCD phase diagram, showing the different phases of nuclear matter and their respective regions. The diagram is divided into several regions. The low-temperature, low-baryon chemical potential region corresponds to the hadronic phase. As the temperature rises, the system enters the crossover region, where the transition from hadronic matter to QGP is smooth. At high temperatures and low baryon chemical potentials, the system fully transitions into the QGP phase. As the baryon chemical potential increases, the transition becomes a first-order phase transition with a coexistence

region between the hadronic and QGP phases. The endpoint of this first-order line is believed to indicate a second-order phase transition, marking the critical point (T_c). At very high baryon chemical potentials, the system transitions to a color superconducting phase (CSC), where quarks pair up to form a condensate that breaks color symmetry.

The QCD phase diagram has been extensively studied using lattice QCD simulations, as well as experiments at heavy-ion colliders such as RHIC and LHC. These studies have provided insights into the properties of nuclear matter at extreme temperatures and densities, as well as the nature of the QCD phase transition. Also, the search for the QCD critical point is a key focus in investigating the QCD phase diagram.

1.5 Kinematic Variables

To make data analysis easier for experiments at STAR and other relativistic heavy-ion collisions, it is helpful to use kinematic observables that either remain unchanged (Lorentz invariant) or transform in a simple way when moving from one reference frame to another. This section introduces some commonly used kinematic observables that are defined based on the conventions used in the experiments. In the STAR experiment, the collision axis is along the z-direction, which is the same as the beam direction. Therefore, before the collisions, there is no momentum in the x-y plane. The interaction point (IP) is typically at (0,0,0), the center of the STAR detector. However, not all collisions happen exactly at this point. Instead, they are distributed around this central location. The collision point for each event, known as the primary vertex, needs to be reconstructed during the experiment.

1.5.1 Center-of-mass Energy (\sqrt{s})

Center-of-mass energy is defined as the square root of Mandelstam's variable s . This variable, s , is the square of the sum of the four-momenta of two colliding particles, and it remains invariant under Lorentz transformations.

Consider two particles, A and B. The variable s is given by the equation:

$$s = (p_A + p_B)^2 = (E_A + E_B)^2 - (\vec{p}_A + \vec{p}_B)^2. \quad (1.5)$$

Here, p_A and p_B are the four-momenta, E_A and E_B are the energies, and \vec{p}_A and \vec{p}_B are the momentum vectors of particles A and B, respectively.

In the center-of-mass frame, the momentum vectors satisfy:

$$\vec{p}_A + \vec{p}_B = 0.$$

If the two particles have the same mass, then $E_A = E_B = E$. Substituting these values into the equation simplifies the calculation of s .

In Eq. 1.5, the center-of-mass energy in this case is $\sqrt{s} = 2E$. In heavy-ion collisions, the center-of-mass energy is often expressed per nucleon, $\sqrt{s_{NN}}$. For example, in Au+Au collisions at RHIC, the highest $\sqrt{s_{NN}}$ is 200 GeV, meaning each of the 197 nucleons in gold is accelerated to 100 GeV from opposite directions to collide.

At ultra-relativistic energies, heavy-ion collisions produce several new particles. Charged particles move in helical paths, called tracks, under the detector's magnetic field before being detected. Some key kinematic variables related to these tracks are as follows.

1.5.2 Transverse Momentum (p_T)

The momentum of a charged particle can be split into two components: one along the beam axis (p_z) and one in the transverse x-y plane (p_T). The transverse momentum, p_T , is Lorentz invariant and is defined as:

$$p_T = \sqrt{p_x^2 + p_y^2},$$

where p_x and p_y are the momenta along the x and y axis, respectively.

1.5.3 Azimuthal Angle (ϕ)

The azimuthal angle, denoted as ϕ , is the angle between the projection of a charged particle's momentum vector onto the x-y plane and the x-axis. It represents the direction of the particle's momentum in the transverse plane. The azimuthal angle can be expressed in terms of the momentum components p_x and p_y as:

$$\phi = \tan^{-1} \left(\frac{p_y}{p_x} \right).$$

This angle is important for analyzing the spatial distribution of particles in the transverse plane.

1.5.4 Rapidity (y)

In relativistic conditions, momentum and velocity are not additive. Therefore, in heavy-ion collisions, rapidity (y) is a more useful and additive quantity. It is also Lorentz invariant and is defined as:

$$y = \frac{1}{2} \ln \left(\frac{E + p_z}{E - p_z} \right),$$

where E is the energy of the charged particle, and p_z is the momentum along the z-axis.

1.5.5 Pseudorapidity (η)

Calculating rapidity requires both energy and momentum, which can be difficult since measuring energy involves knowing the particle's mass. In some cases, the mass isn't crucial, so experimentalists use pseudo-rapidity (η) instead. It is defined as:

$$\eta = \frac{1}{2} \ln \left(\frac{|\mathbf{p}| + p_z}{|\mathbf{p}| - p_z} \right) = -\ln(\tan(\theta/2)),$$

where \mathbf{p} is the momentum of the charged particle, p_z is the momentum along the z-axis, and θ is the polar angle of the particle relative to the beam axis. Pseudo-rapidity is Lorentz invariant and can be calculated using just the polar angle θ .

1.5.6 Natural unit

In heavy-ion physics, it is easier to use a system where the speed of light c and Planck's constant \hbar are set to 1. This system, called natural units, is common in particle physics. With c and \hbar fixed, only energy is used as the main unit, so all physical quantities are expressed in terms of energy. Table 1.1 shows the natural units for mass, length, and time, along with their conversion factors from SI units.

Physical Quantity	Natural unit	Conversion from SI unit
Time	GeV ⁻¹	1 s = 1.52 × 10 ²⁴ GeV ⁻¹
Length	GeV ⁻¹	1 m = 5.07 × 10 ¹⁵ GeV ⁻¹
Mass	GeV	1 kg = 5.61 × 10 ²⁶ GeV

Table 1.1: Time, length, and mass in natural units.

1.6 Heavy-Ion Collisions at Relativistic Energies

Heavy-ion collision experiments are designed to recreate conditions similar to those in the early universe, moments after the Big Bang. By colliding heavy-ions at extremely high energies, at velocities approaching the speed of light, these experiments create the quark-gluon plasma phase of the matter. The investigation into heavy-ion collisions at relativistic speeds began in the 1970s with experiments conducted at the Bevalac accelerator, located at the Lawrence Berkeley National Laboratory. Over the years, various experimental facilities have been developed to study heavy-ion collisions, including the Super Proton Synchrotron (SPS) at CERN, the Relativistic Heavy Ion Collider (RHIC) at Brookhaven National Laboratory, and the Large Hadron Collider (LHC) at CERN. The LHC is the largest and most powerful accelerator in the world and has been used to study heavy-ion collisions at even higher energies than previous experiments. These experiments have

provided valuable insights into the behavior of matter under extreme conditions and helped to advance our understanding of the fundamental nature of the universe.

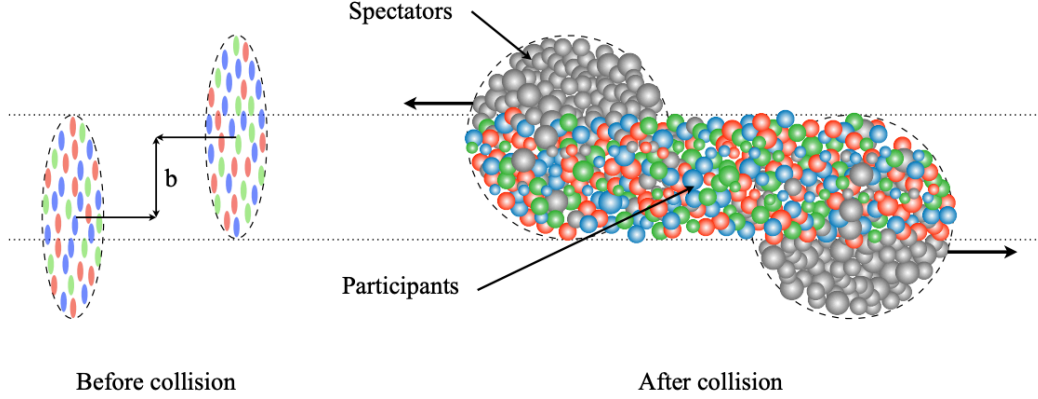


Figure 1.5: A schematic of a heavy-ion collision displays the impact parameter (b) and the spectator and participant nucleons [22].

In relativistic heavy-ion collisions, two nuclei are accelerated to near light-speed and collide head-on (Figure 1.5). Due to special relativity, the nuclei contract along their direction of motion. The overlap region depends on the impact parameter (b), which is the distance between the centers of the nuclei. Central collisions (small b) involve the most overlap, whereas peripheral collisions (large b) have less. In between are semi-central collisions. Nucleons (particles within the nuclei) interacting in the overlap region are called “participants”, while those that do not interact are “spectators”. The number of participants and spectators directly depends on the impact parameter.

The evolution of heavy-ion collisions can be described as a series of stages that occur in space and time. The process starts with the collision of two spherical nuclei traveling at relativistic speeds in the center of mass (CM) frame. Due to their high velocity, the nuclei are Lorentz contracted along their direction of motion. When the nuclei collide at time $t=0$ and location $z=0$, a large amount of energy is deposited in the interaction region, creating a “fireball” in the mid-rapidity region, $y = 0$ as shown in Fig 1.6.

The Bjorken energy density [24], denoted as (ε), plays a crucial role in determining the results of a heavy-ion collision. For a collision that occurs at the origin $(z, t) = (0, 0)$, the energy density in the central region can be determined using the proper time, $\tau = \sqrt{t^2 - z^2}$. The formula for calculating the energy density is:

$$\varepsilon(\tau) = \frac{1}{\tau A} \frac{dE_T}{dy} \quad (1.6)$$

In this expression, A stands for the transverse area of the colliding nuclei, and $\frac{dE_T}{dy}$ is the transverse energy of the collision products, excluding the kinetic energy due to motion along the z -axis, per unit rapidity y . This quantity can be measured experimentally.

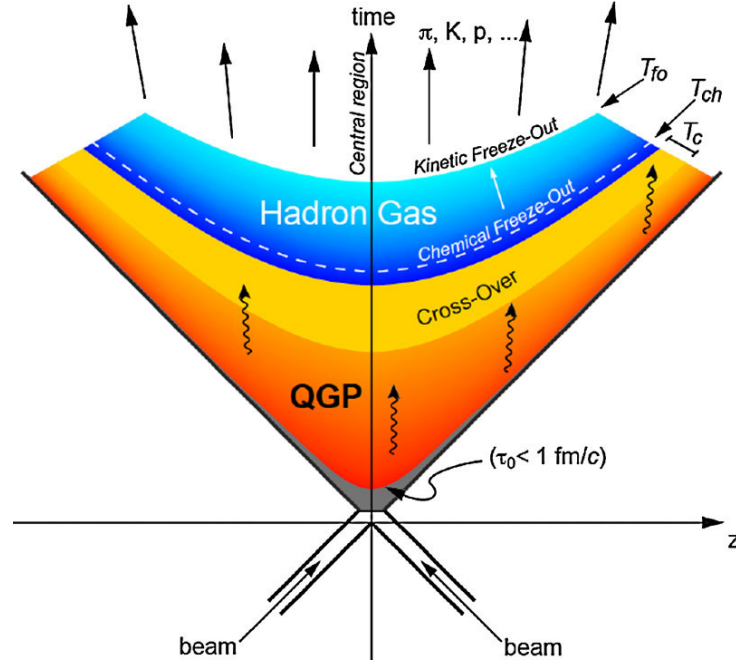


Figure 1.6: A schematic diagram showing the space-time evolution of the system created in high-energy heavy-ion collision experiments. [23]

If the energy density produced does not attain the essential threshold required for the formation of QGP, the system will manifest as a hadron gas. If QGP is formed, the system quickly expands and cools due to its excess pressure with respect to the vacuum. The evolution can be described by relativistic hydrodynamics. At some point, temperature of the created system falls below critical temperature (T_c), and hadrons are reformed, and the quarks and gluons become confined. If there is a first-order phase transition, the system goes through a mixed phase, where quarks and gluons coexist with hadrons. The expansion is likely to be isothermal in this phase, and latent heat is used to convert the quarks and gluons to hadrons. As the system of hadrons continues to expand, “Chemical Freeze-Out” occurs at a temperature T_{ch} , where the inelastic interactions between the hadrons cease, and the composition of different hadron species does not change anymore. The resulting hadronic gas continues to cool until interaction rates become insufficient to maintain thermal equilibrium in the expanding medium, reaching a temperature T_{fo} , when the distance between the hadrons is larger than the mean free path, and the elastic interactions between the hadrons cease. This is known as “Thermal” or “Kinetic Freeze-Out”, from this point, the hadrons are free to stream away to be detected by the detectors. In conclusion, the evolution of heavy-ion collisions is a complex process that involves several stages, including the initial stages, thermalization, expansion, and freeze-out.

1.7 Signatures of Quark-Gluon Plasma

The QGP formation is possible under high temperature and energy density conditions. However, the quark-gluon plasma produced in heavy-ion collisions cannot be directly observed in experiments. The only way to study the properties of this medium is through the analysis of final state particles as proxies. In this section, we will examine experimental observables to gain a deeper understanding of the medium formed during heavy-ion collisions.

1.7.1 Particle Yields and Spectra

In the event of a collision between two heavy-ions at relativistic velocities, the immense energy density produced leads to the existence of quarks and gluons in free states. As the medium evolves, it passes through several stages before eventually forming hadrons, as discussed in Section 1.4. Particle ratios stabilize during chemical freeze-out, while particle momentum becomes fixed at kinetic freeze-out. A critical aspect of understanding the chemical and kinetic freeze-out properties of the medium lies in the analysis of the transverse momentum spectra of hadrons. The invariant yield of hadrons can be calculated using the following formula:

$$E \frac{d^3N}{d^3p} = \frac{d^2N}{2\pi p_T dp_T dy} \quad (1.7)$$

In this expression, E represents the particle energy, and $\frac{d^2N}{dp_T dy}$ corresponds to the event-wise yield density. By examining the p_T spectra, it is possible to extract the yield ($\frac{dN}{dy}$), inverse slope parameter (T), and average transverse momentum ($\langle p_T \rangle$).

Particles in the final state, associated with different momentum regimes, can result from separate production mechanisms. Most particles with p_T below 2.0 GeV/c, frequently referred to as the soft part, are primarily produced through thermal processes within the QGP medium. On the other hand, particles with larger transverse momentum ($p_T > 6.0$ GeV/c) mainly originate from perturbative processes, constituting the hard sector. The coalescence mechanism dominates the intermediate transverse momentum regime. Employing thermal models proves to be a reliable and accurate method for interpreting particle production in areas with low p_T region.

Statistical models utilize particle yields or particle ratios to extract the temperature and baryon chemical potential (μ_B) of the system at chemical freeze-out under the assumption of thermal and chemical equilibrium at that stage. Figure 1.7 presents the measurements of p_T -integrated hadron yield ratios for various particle species in central Au+Au collisions at $\sqrt{s_{NN}} = 200$ GeV, as obtained from the STAR experiment [26]. The horizontal lines depict comparisons with results derived from statistical thermal models

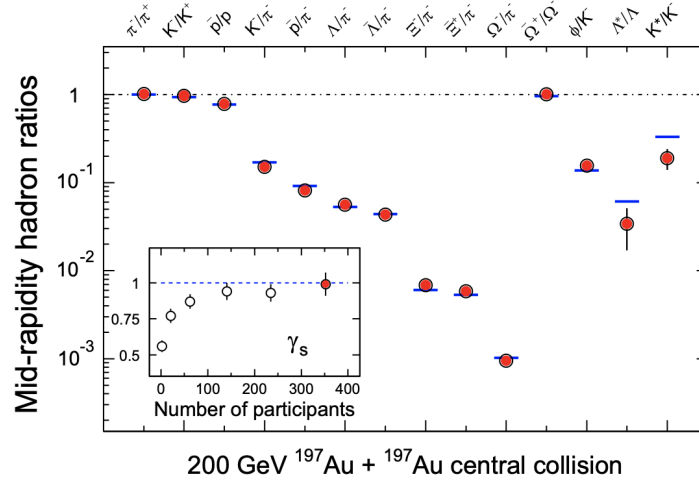


Figure 1.7: The figure displays ratios of mid-rapidity p_T -integrated yields for different hadron species in Au+Au collisions at $\sqrt{s_{NN}} = 200$ GeV [25]. Horizontal lines indicate statistical model fits with parameters $T_{\text{ch}} = 163 \pm 4$ MeV, $\mu_B = 24 \pm 4$ MeV, and $\gamma_s = 0.99 \pm 0.07$. The inset shows the centrality-dependent variation of γ_s .

[27]. These models typically assume thermodynamic equilibrium. The model parameters include the chemical freeze-out temperature (T_{ch}) and the baryon chemical potential (μ_B) and the strangeness suppression factor (γ_s). The values of parameters obtained from the fits are $T_{\text{ch}} = 163 \pm 4$ MeV, $\mu_B = 24 \pm 4$ MeV, and $\gamma_s = 0.99 \pm 0.07$. A remarkable agreement is observed between the data and the model for these ratios, encompassing stable and long-lived hadrons (such as π , K , p) as well as multi-strange baryons (Λ , Ξ , and Ω). However, significant deviations are noted for the short-lived resonance yields, including Λ^* and K^* , which could be attributed to hadronic rescattering after the chemical freeze-out. The strangeness suppression factor (γ_s) as a function of centrality is illustrated in the inset of Fig. 1.7. This factor indicates deviation from chemical equilibrium. For central Au+Au collisions, the value of γ_s is near unity, suggesting that chemical equilibrium has been attained in central Au+Au collisions at $\sqrt{s_{NN}} = 200$ GeV.

The study of transverse momentum distributions for different hadrons can reveal insights into kinetic freeze-out properties. Fits inspired by hydrodynamic models have been applied to the measured spectra, enabling the extraction of model parameters that describe random (typically regarded as the kinetic freeze-out temperature T_{fo}) and collective (radial flow velocity $\langle \beta_T \rangle$) aspects.

Figure 1.8 shows the values of T_{fo} and $\langle \beta_T \rangle$ extracted from thermal and radial flow fits for different centrality bins and hadron species in Au+Au collisions at $\sqrt{s_{NN}} = 200$ GeV. It is observed that the bulk of the system, comprising pions, kaons, and protons, cools down at kinetic freeze-out and exhibits a stronger collective flow. This suggests a rapid expansion following chemical freeze-out, which appears to increase with centrality. The results obtained for ϕ and Ω imply a reduction in hadronic interactions after chemical

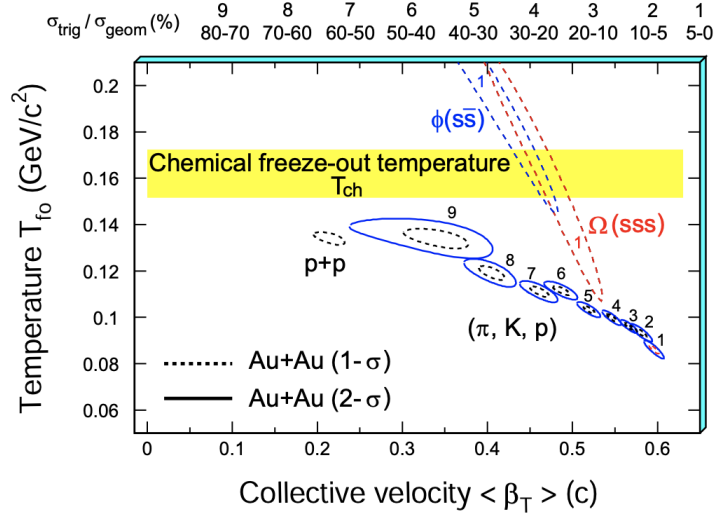


Figure 1.8: χ^2 contours from thermal + radial flow fits for identified (π, K, p) and multi-strange (ϕ, Ω) hadrons in $\sqrt{s_{NN}} = 200$ GeV Au+Au collisions [28]. Centrality labels are provided on the top, and dashed and solid lines represent $1 - \sigma$ and $2 - \sigma$ contours, respectively.

freeze-out.

1.7.2 Anisotropic Flow

Anisotropic flow is a bulk property of the QGP that can provide valuable information about the collective dynamics, degree of freedom, and thermalization at the early stage of a noncentral heavy-ion collisions. During these collisions, the overlapped area has a spatial azimuthal anisotropy, which is converted to momentum-space anisotropy through rescatterings among the constituents of the system. The overlapping region in a non-central heavy-ion collision becomes oval-shaped, as shown in Fig. 1.9. As the system evolves, the spatial anisotropy decreases, making the momentum-space anisotropy sensitive to the early phase of the evolution when the spatial anisotropy is significant.

In experimental studies, anisotropic flow is analyzed through the Fourier expansion of the momentum space azimuthal angle (ϕ) distributions of hadrons concerning the reaction plane. The global picture of anisotropic flow is reflected in the ϕ distribution in momentum space, which can be described by the sum of anisotropic flow for each harmonic through Fourier series. The Fourier coefficients v_n are then used to characterize the n -th harmonic azimuthal anisotropy of hadron production.

$$E \frac{d^3 N}{d^3 p} = \frac{d^2 N}{2\pi p_T dp_T dy} (1 + 2v_n \cos[n(\phi - \Psi_{RP})]),$$

where E represents the energy of the particle, p represents the momentum of the particle, p_T is the transverse momentum of the particle, ϕ represents the azimuthal angle of the

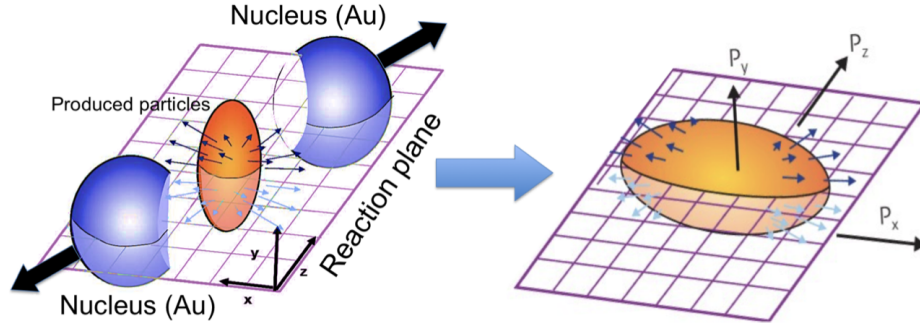


Figure 1.9: A schematic of the almond-shaped impact region evolving into anisotropic expansion in momentum space after a non-central collision [29].

particle, y represents the rapidity of the particle, and Ψ_{RP} is the angle of the reaction plane. The reaction plane is defined as the plane that includes both the beam axis and the direction of the impact parameter. Due to the reflection symmetry with respect to the reaction plane, the sine terms in the Fourier expansion vanish. The Fourier coefficients depend on both p_T and y , and are defined as $v_n(p_T, y) = \langle \cos[n(\phi - \Psi_{RP})] \rangle$. Here, the angular brackets represent an average over all particles, summed over all events, in the (p_T, y) bin under investigation. The directed and elliptic flow coefficients in the Fourier decomposition are represented by v_1 and v_2 , respectively.

1.7.2.1 Directed flow (v_1)

Directed flow, v_1 , reflects the collective sideward motion of produced particles and nuclear fragments, providing insights into the early stages of collisions. A first-order phase transition may result in a “softest point” in the equation of state (EOS), where the expansion of matter slows down. This softening can be detected experimentally by a minimum in v_1 as a function of beam energy [31, 32]. The softening, potentially signaling the formation of the QGP, leads to a distinct flow pattern [33]. Hydrodynamic calculations assuming QGP, predict that $v_1(y)$ crosses zero three times around midrapidity, forming a “wobble point” structure in near-central collisions, which may arise from a tilted, expanding fluid source. However, RQMD model calculations, which do not assume QGP formation, also predict the wobble but in peripheral and mid-central events. Figure 1.10 shows the charged particle v_1 versus η for 10–70% Au+Au collisions at $\sqrt{s_{NN}} = 62.4$ GeV, with results from three methods and various models (AMPT [34–36], RQMD [37], UrQMD [38–40]) for same system and centrality and collision energy. The arrows in the upper panel show the flow direction of spectator neutrons. The models are observed to under-predict the charged particle v_1 near mid-pseudorapidity (see lower panel), while they show good agreement at larger $|\eta|$. Additionally, no significant wobble structure, as previously discussed, is seen within the measured pseudorapidity range for this data set.

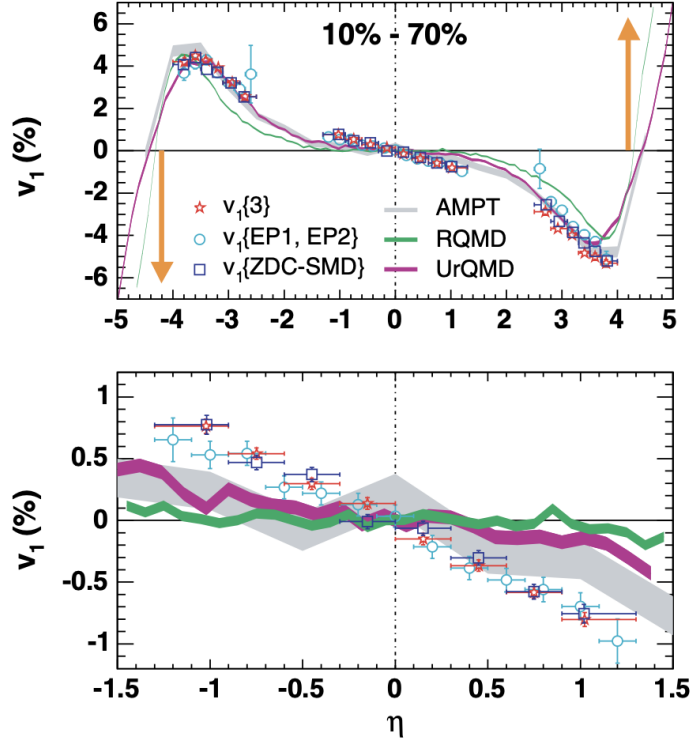


Figure 1.10: The upper panel shows the charged particle directed flow as a function of pseudorapidity from the STAR experiment [30], while the lower panel provides a detailed view of the mid-pseudorapidity region.

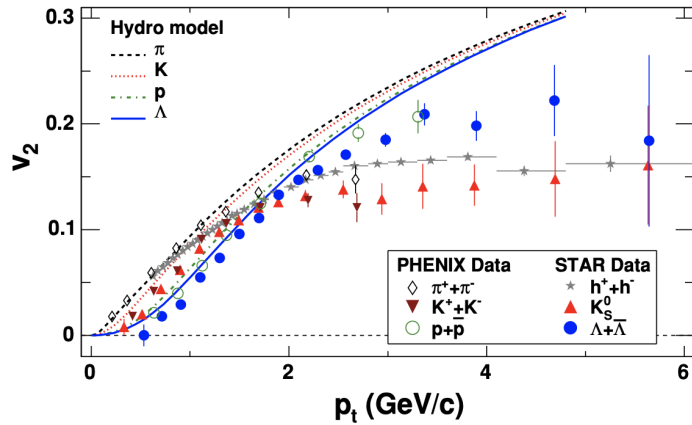


Figure 1.11: v_2 vs p_T for different hadrons from minimum bias collisions in Au+Au at $\sqrt{s_{NN}} = 200$ GeV. The STAR K_S^0 and $\Lambda + \bar{\Lambda}$ data, along with the PHENIX data and hydrodynamic calculations [41].

1.7.2.2 Elliptic flow (v_2)

Figure 1.11 shows elliptic flow (v_2) as a function of p_T for light quark-carrying hadrons ($\pi^+ + \pi^-$, $K^+ + K^-$, $p + \bar{p}$) and strange hadrons (K_S^0 , $\Lambda + \bar{\Lambda}$) at mid-rapidity in minimum bias Au+Au collisions at $\sqrt{s_{NN}} = 200$ GeV from the STAR experiment at RHIC [41]. The lines represent results from ideal hydrodynamic model calculations. In the low p_T region (< 2 GeV/c), lighter hadrons exhibit larger v_2 than heavier hadrons, a phenomenon known as mass-ordering of v_2 . This mass-ordering is expected from ideal hydrodynamic calculations [42]. In the intermediate p_T region ($2 < p_T < 5$ GeV/c), v_2 of identified hadrons is separated into two groups, baryons and mesons. This baryon-meson difference in v_2 is consistent with quark coalescence models, which suggest the existence of a deconfined state of quarks and gluons.

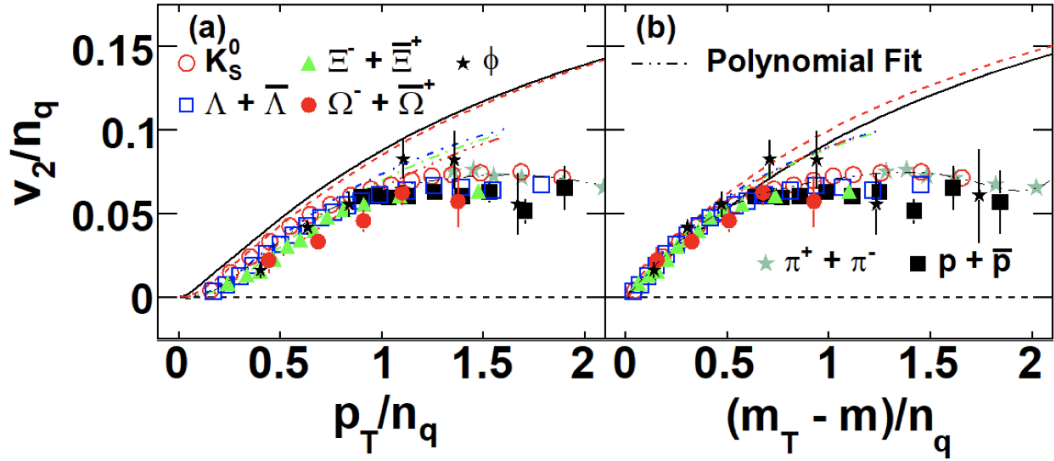


Figure 1.12: The left panel presents v_2/n_q versus $(p_T)/n_q$, while the right panel depicts v_2/n_q against $(m_T - m)/n_q$ in minimum bias Au+Au collisions at $\sqrt{s_{NN}} = 200$ GeV [43].

Figure 1.12 shows $v_{2,\text{scaled}}$ as a function of p_T/n_q (left panel) and $(m_T - m)/n_q$ (right panel) for identified hadrons at mid-rapidity in minimum bias Au+Au collisions at $\sqrt{s_{NN}} = 200$ GeV from the STAR experiment. The choice of the variable $(m_T - m)/n_q$, where m is the rest mass of a particle, removes the particle mass dependence from v_2 at low p_T . This scaling behavior, known as number of constituent quark (NCQ) scaling, can be explained by quark recombination or coalescence models, which assume that flow is developed at the quark level before hadronization, and flow of hadrons is a result of the recombination of their constituent quarks [44, 45]. Therefore, this NCQ scaling of elliptic flow suggests the formation of a partonic medium, where quarks and gluons are the effective degrees of freedom in Au+Au collisions at 200 GeV.

1.7.3 Direct Photons

In a heavy-ion collision, the direct photons, i.e. those not produced via hadronic decays in the final stage of the reaction, encode information about the environment in which they were created. In a thermally balanced quark-gluon plasma, direct photons emerge from gluonic processes involving the following reactions: $q\bar{q} \rightarrow \gamma g$, $gq \rightarrow \gamma q$, $g\bar{q} \rightarrow \gamma\bar{q}$. Photons are known to interact with particles via electromagnetic interactions. When produced within the quark-gluon plasma region, they exhibit minimal participation in strong interactions with quarks and gluons. As a result, their mean-free path is considerably extensive, and they may not experience a collision after their creation. This property enables them to retain information about the temperature at their production point. Thus, they can offer insights into the quark-gluon plasma formed during the initial stages of collisions, serving as a reliable indicator of the QGP.

Direct photons have smaller yields compared to the substantial background from electromagnetic decays. By isolating direct photon yields from background contributions, it is possible to gain insights into the behavior of quarks and gluons within the system prior to hadronization. Direct photon yields have been successfully obtained in experiments such as the RHIC during Au+Au collisions at $\sqrt{s_{NN}} = 200$ GeV.

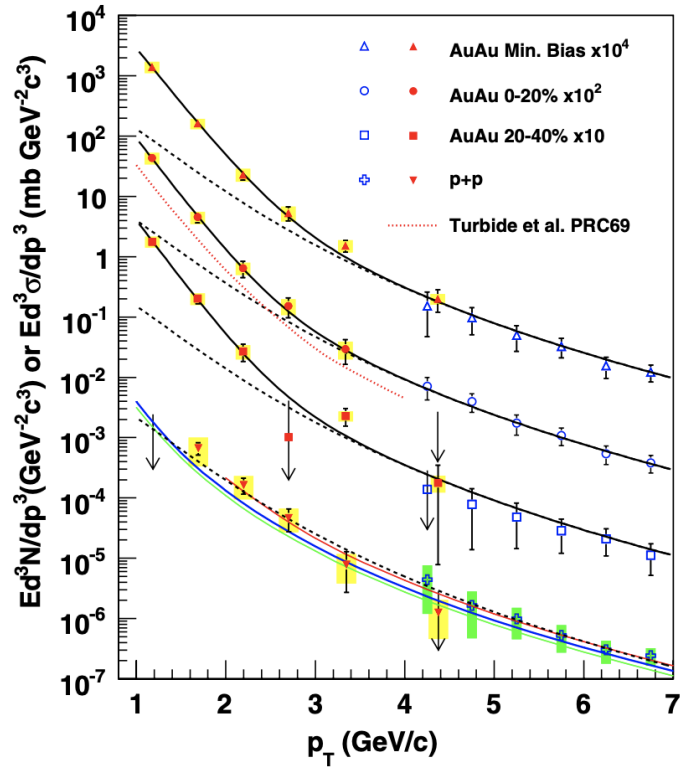


Figure 1.13: The invariant cross-section and yield of direct photons in $p + p$ and Au + Au collisions at $\sqrt{s_{NN}} = 200$ GeV as a function of p_T , measured by the PHENIX experiment [46].

Figure 1.13 shows the direct photon spectra from the PHENIX experiment with Next-

to-Leading Order pQCD (NLO pQCD) calculations. Similar results have been measured in d+Au, p+p, and Au+Au collisions at 200 GeV in the STAR experiment [47, 48]. The NLO pQCD calculations align well with the p+p data for $p_T > 2$ GeV/c, showing consistency within theoretical uncertainties. However, for central Au+Au collisions with $p_T < 2.5$ GeV/c, the Au+Au data surpass the scaled p+p fit curve (dashed curves) by T_{AA} . Where $T_{AA} = \langle N_{\text{bin}} \rangle / \sigma_{\text{inel}}^{\text{NN}}$ represents the nuclear thickness function, where $\langle N_{\text{bin}} \rangle$ denotes the average number of binary nucleon-nucleon inelastic collisions as calculated using the Glauber model, and $\sigma_{\text{inel}}^{\text{NN}}$ is the inelastic cross-section for a nucleon-nucleon collision. This suggests a more rapid increase in the direct photon yield compared to the binary nucleon-nucleon collision-scaled p+p cross section at low p_T .

The thermal photon spectrum, computed with an initial temperature $T_{\text{init}} = 370$ MeV in Au+Au collisions, is represented by the red dotted curve in [49]. Figure 1.14 illustrates a comparison between direct photon data from Au+Au collisions at $\sqrt{s_{NN}} = 200$ GeV within 0–20% centrality and theoretical models predicting thermal photon emission [50]. These theoretical models are based on the assumption that a chemically thermalized QGP medium is formed, characterized by a hot and dense state. The thermalization time, τ_0 , is taken to range between 0.6 fm/c and 0.15 fm/c, which corresponds to an initial temperature range of $T_{\text{init}} = 300$ MeV to 600 MeV. Therefore, the experimentally observed direct photon spectra qualitatively support the existence of a deconfined quark-gluon plasma phase during these high-energy collisions.

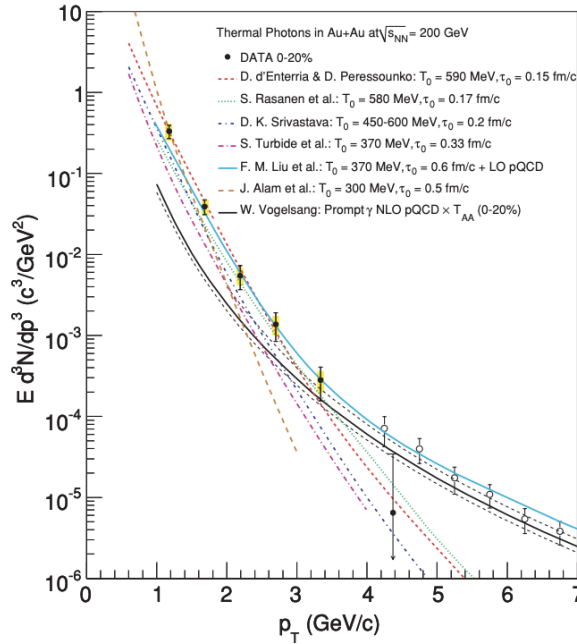


Figure 1.14: Direct photon spectra measured by PHENIX at RHIC energies [50].

1.7.4 Strangeness Enhancement

Strangeness enhancement, as a signature of QGP, can be observed through the production of strange hadrons in high-energy hadronic interactions. While ordinary matter is formed by up (u) and down (d) quarks, strange (s) quarks are unique, as they are not present as valence quarks in the initial state. The presence of strange quarks in the final state hadrons can only occur if these quarks originate from the medium itself. The enhancement of strange particle production has been one of the earliest proposed indicators of the deconfined QGP phase [51]. Notably, the mass of strange quarks and anti-quarks is comparable to the energy scale at which nucleons break down into their constituent quarks and gluons. This similarity suggests that the production and abundance of strange quarks are highly sensitive to the conditions, structure, and dynamics of the deconfined QGP phase. Consequently, studying strange quark production provides crucial insights into the properties and behavior of the quark-gluon plasma during heavy-ion collisions.

In the early stages of high-energy collisions, strangeness is generated through a combination of partonic scattering processes, including flavor creation and flavor excitation. Gluon splittings also contribute to strangeness creation during the partonic evolution. These processes primarily dominate the production of high transverse momentum strange hadrons, while non-perturbative processes govern the production of low transverse momentum strange hadrons. The two primary production channels for s and \bar{s} pairs are $q\bar{q} \rightarrow s\bar{s}$ and $gg \rightarrow s\bar{s}$. When considering the s and \bar{s} production from the $q\bar{q}$ interaction, it takes approximately eight times the natural lifespan of a QGP fireball to reach chemical equilibrium in strangeness. Consequently, Rafelski and others proposed that the majority of quark-antiquark pairs are predominantly created through gluon-gluon fusion [51]. Strange quark production is generally suppressed in comparison to hadrons containing only light quarks due to the heavier nature of strange quarks.

The excitation function of strangeness is qualitatively examined by calculating the ratio of kaon (K^+) yield to that of pion (π^+) yield. This ratio characterizes the relative abundance of strangeness over hadron multiplicity. The SPS experiment at CERN and STAR experiment at RHIC have observed the excessive production of kaons relative to pions, up to three times the value in $p + p$ collisions at the same energy [53–59].

The strangeness enhancement of a specific particle species is experimentally determined as the ratio of the strange hadron yield per participant nucleon in nucleus-nucleus collisions to that in a smaller reference system, such as $p + p$ collisions. Figure 1.15 presents the STAR experiment's measurements of strangeness enhancement for K^- , ϕ , $\bar{\Lambda}$, and $\Xi + \bar{\Xi}$ in Au+Au and Cu+Cu collisions relative to $p + p$ collisions, plotted as a function of the average number of participant nucleons. The results indicate that this ratio exceeds one and increases with both centrality and energy. These findings provide experimental evidence for the formation of a deconfined phase characterized by enhanced

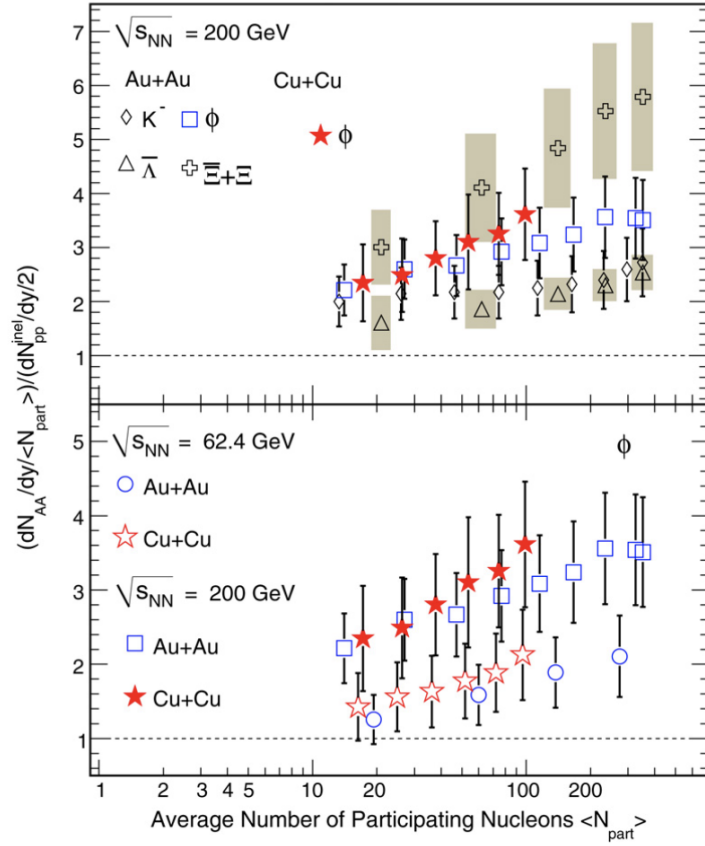


Figure 1.15: The upper panel displays the ratio of yields for K^- , ϕ , $\bar{\Lambda}$, $\Xi + \bar{\Xi}$ in Au+Au and Cu+Cu collisions at $\sqrt{s_{NN}} = 200$ GeV, normalized by the average number of participant nucleons $\langle N_{part} \rangle$, relative to the corresponding yields in $p + p$ collisions. The lower panel illustrates the same ratio but for a collision energy of $\sqrt{s_{NN}} = 62.4$ GeV [52].

production of strange quarks.

1.7.5 Quarkonia Suppression

The charm quark (c) is approximately ten times heavier than the strange quark, and the bottom quark (b) is roughly forty times heavier. Consequently, the energy threshold required for charm quark production is only achievable during the very early stages of the collision. A suggested signature of the QCD phase transition is the suppression of quarkonium production, particularly J/ψ (the ground state of charmonium, $c\bar{c}$). Initially, predictions were made for the J/ψ meson, but these predictions were later extended to the Υ meson (bottomonium, $b\bar{b}$) as well, thereby allowing for the sequential melting of quarkonia. Quarkonia suppression analysis represents another type of nuclear-modification analysis, aiming to measure the difference between the yield of quarkonia states in heavy-ion collisions and an equal number of nucleon-nucleon collisions. In doing so, the quantity R_{AA} is computed.

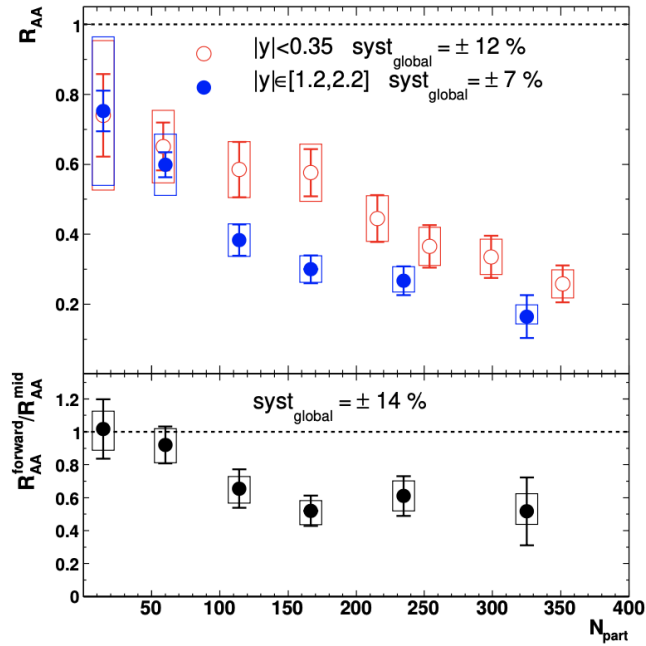


Figure 1.16: R_{AA} of J/Ψ in Au+Au collisions at $\sqrt{s_{NN}} = 200$ GeV as a function of N_{part} . The mid-rapidity and forward rapidity data are respectively shown in open and solid symbols. The ratio of J/Ψ R_{AA} in forward rapidity to mid-rapidity is also presented as a function of N_{part} [60].

If R_{AA} is equal to unity, the number of quarkonia mesons measured in the heavy-ion reaction is the same as what would be expected for a superposition of N_{bin} nucleon-nucleon interactions, where N_{bin} is the number of binary nucleon-nucleon interactions for the centrality class of interest in heavy-ion collisions.

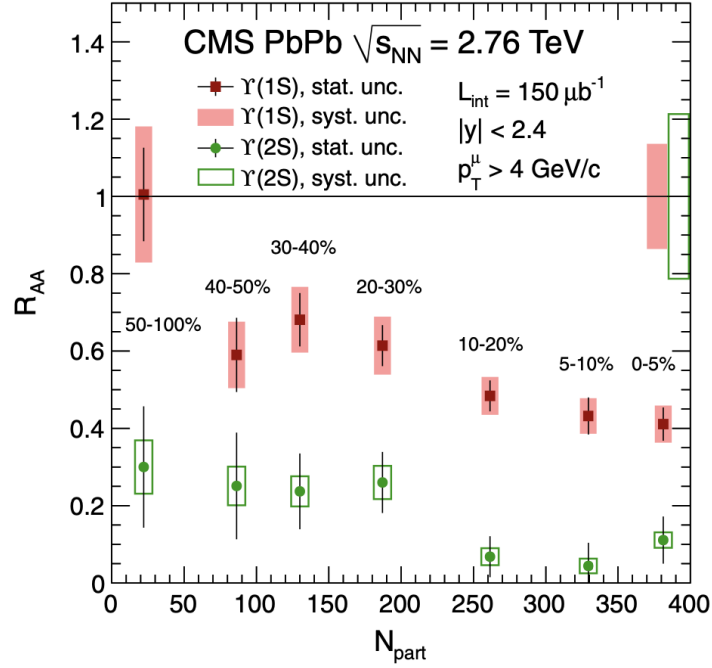


Figure 1.17: The nuclear modification factor R_{AA} of the individual $\Upsilon(1S)$ and $\Upsilon(2S)$ state production as a function of event centrality measured by CMS in Pb+Pb collisions [61].

Both STAR [60] and CMS [61] have conducted measurements of quarkonium (J/Ψ and Υ) suppression, as depicted in Fig. 1.16 and 1.17, respectively. The STAR results also reveal that J/Ψ production is suppressed in Au+Au collisions compared to p+p collisions shown in Fig. 1.16. The CMS results exhibit clear suppression for both the $\Upsilon(1S)$ and $\Upsilon(2S)$ states in all but the most peripheral collisions, where suppression is not observed for the ground state. Furthermore, the CMS results demonstrate sequential melting, as the more tightly bound ground state is less suppressed across all centralities compared to the excited 2S state. In both cases, the measured suppression aligns with the expectations if the medium produced in heavy-ion collisions provides the color screening mechanism of the QGP, as proposed by Matsui and Satz [62, 63].

1.7.6 High p_T Probes

Jet quenching refers to the suppression of hadron jets that are produced from high-energy quark and gluon interactions in the early stages of heavy-ion collisions. This phenomenon occurs as the jets lose energy while traversing the hot and dense medium created in the collision. These jets are comprised of highly energetic particles confined within a narrow cone due to hard scattering. As illustrated in Fig. 1.18, hadron jets are generated back-to-back in A+A collision, known as dijets, in accordance with momentum conservation. The effects of the hot, dense QGP on these jets arise from both elastic [64] and inelastic processes, including gluon radiation [65]. High-momentum partons are more susceptible

to the high gluon density within the QGP [66]. Consequently, the sub-leading jets in A+A collision are absorbed by the QGP medium, resulting in the “quenched jet”. However, in small systems like p+p or d+Au where no QGP exists, there is no in-medium disruption, and therefore no jet quenching is anticipated.

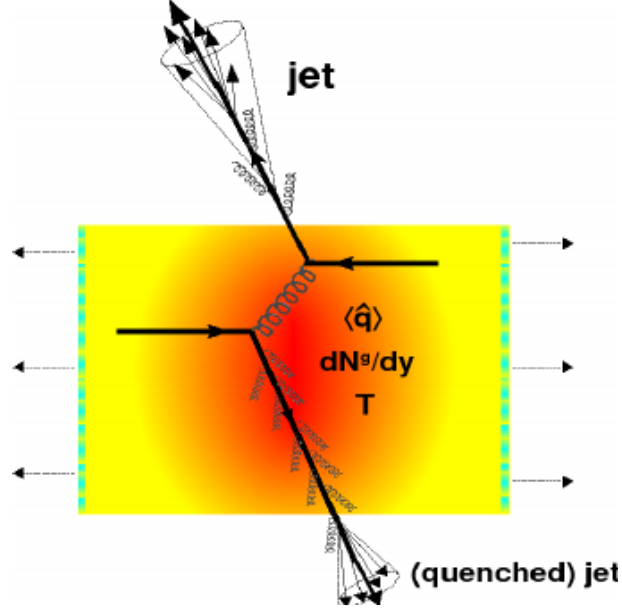


Figure 1.18: Back-to-back jets consist of one near-side jet produced near the surface of the hot and dense medium and another away-side jet deep inside, with the latter experiencing quenching. The medium’s properties include temperature (T), gluon number density in rapidity space (dN_g/dy), and the jet-quenching parameter (\hat{q}) [67].

Experimentally, the intriguing disappearance of jets in heavy-ion collisions can be observed by measuring dihadron azimuthal correlations for high p_T particles. This quantity is determined for hadrons with $p_T > 2$ GeV/c in relation to a triggered hadron with $p_{\text{trig}} > 4$ GeV/c by the STAR collaboration in p+p, d+Au, and Au+Au collisions, as shown in Fig. 1.19 [68]. As depicted in Fig. 1.19, the down-side jet in Au+Au collisions is absent, signifying the jet quenching effect in heavy-ion collisions. In contrast, the down-side jet is present in p+p and d+Au collisions, where no QGP is formed.

An alternative method for quantifying the jet quenching effect is through the nuclear modification factor (R_{AA}), defined as the ratio of a specific hadron yield in nucleus-nucleus collisions to the corresponding p+p collision:

$$R_{AA} = \frac{d^2 N^{AA}/dp_T d\eta}{T_{AA} d^2 \sigma^{NN}/dp_T d\eta}, \quad (1.8)$$

where AA and NN in case of RHIC, are the Au+Au and p+p collision, respectively. T_{AA} is the nuclear thickness function, and $\sigma_{\text{inel}}^{\text{NN}}$ is the inelastic cross-section of a nucleon-nucleon collision. In the absence of in-medium effects, R_{AA} in AA collisions would be expected to be a multiplicative of pp collisions with a value close to unity at high p_T , where hard

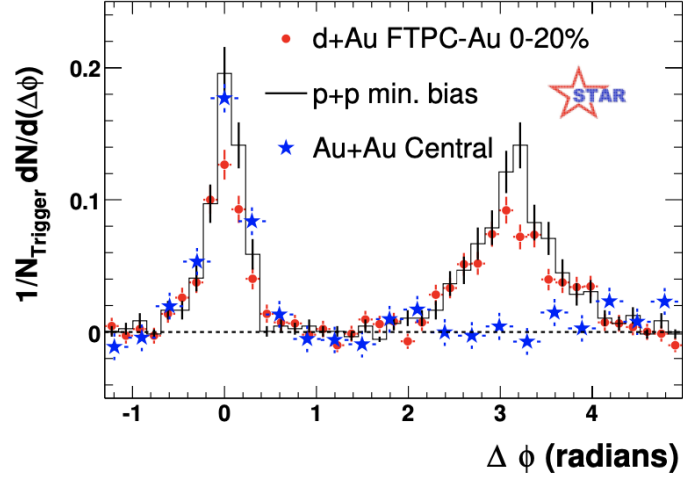


Figure 1.19: Dihadron azimuthal correlations in $p + p$, central $d + \text{Au}$, and central $\text{Au} + \text{Au}$ at $\sqrt{s_{NN}} = 200 \text{ GeV}$ measured by STAR at RHIC [68].

scattering predominantly takes place.

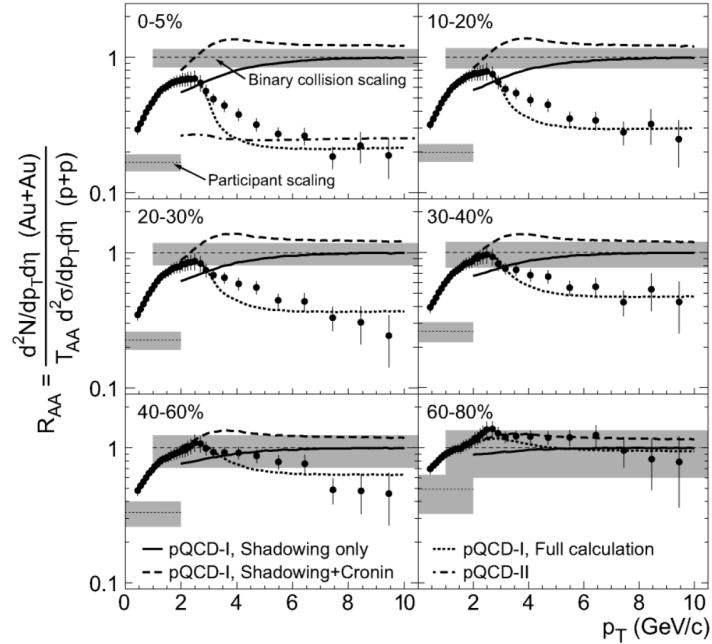


Figure 1.20: Investigating R_{AA} for pairs of charged hadrons at mid-rapidity ($|y| < 0.5$) across various centrality classes in $\text{Au} + \text{Au}$ collisions, relative to $p + p$ collisions [57].

As shown in Fig. 1.20 [57], the STAR experiment observed R_{AA} with respect to p_T in $\text{Au} + \text{Au}$ collisions relative to $p + p$ collisions at $\sqrt{s_{NN}} = 200 \text{ GeV}$. It is evident that the value of R_{AA} is significantly lower than unity for most central and mid-central collisions. This suppression is more prominent for central collisions, where in-medium effects are assumed to be most significant. Neither the Cronin enhancement nor shadowing can solely explain this suppression, as they illustrate parton energy loss in the dense plasma

medium. Furthermore, LHC observations [69] have reported even greater suppression than that found at RHIC. The suppression of high p_T particle R_{AA} in central collisions is considered a hallmark of the deconfined phase.

1.8 Outline of the Thesis

The work presented in this thesis involves the study of various observables to comprehend particle production mechanisms in high-energy heavy-ion collisions and investigate the properties of the QGP. The data reported here were collected by the STAR experiment at RHIC. In Chapter 2, a detailed description of the RHIC facility, the STAR detector, and the specific subsystems utilized for the analysis is presented. Chapter 3 discusses the production of identified particles (π^\pm , K^\pm , p , \bar{p}) in Au+Au collisions at $\sqrt{s_{NN}} = 54.4$ GeV and their bulk properties. The discussion includes results on p_T spectra, centrality, and the energy dependence of particle yields, ratios, $\langle p_T \rangle$, and $\langle m_T \rangle$. Chapter 4 focuses on the multiphase transport (AMPT) model and its role in understanding particle production at different center of mass BES-I energies (7.7-200 GeV). In this chapter, we compare data and model outputs to better understand the particle production mechanism. Chapter 5 looks at the forward upgrade within the STAR experiment, mainly discussing the tracking efficiency and momentum resolution of forward upgrade in STAR. This discussion is centered on the dependence of tracking efficiency and momentum resolution on the pixel width of silicon discs, along with considerations related to the primary vertex. Finally, in Chapter 6, we conclude our study with a summary of the results presented in these chapters, highlighting the importance of further expanding the scope of research on these topics.

Chapter 2

STAR Experiment

The data analyzed in this thesis is obtained from the Solenoidal Tracker At RHIC (STAR), which is located at the Brookhaven National Laboratory (BNL) as a part of the Relativistic Heavy-Ion Collider (RHIC) facility. The RHIC project was initiated in the early 90s to study the interactions of quarks and gluons at high energies. The first head-on collisions between Au+Au nuclei inside the RHIC were recorded on June 12, 2000 at 21:00 EDT at the BNL [†]. This incident marked RHIC as the first global facility to collide heavy-ions at relativistic energies. Additionally, it became the first machine potentially forming QGP and making it possible to study its distinctive characteristics.

At the RHIC facility, STAR is one of four experiments, alongside the Pioneering High Energy Nuclear Interaction eXperiment (PHENIX), PHOBOS (named after the Martian moon Phobos), and the Broad RAnge Hadron Magnetic Spectrometers (BRAHMS). The PHENIX experiment underwent a significant upgrade, evolving into the new sPHENIX experiment, which is now operational alongside STAR at BNL. Currently, both STAR and sPHENIX are active experiments at the RHIC facility. This chapter provides a thorough overview of the RHIC facility, covering its various features and details.

2.1 The Relativistic Heavy Ion Collider

RHIC, located at BNL, is an advanced particle accelerator used by physicists to study the fundamental forces and characteristics of matter. Currently, RHIC is the only operational polarized proton collider. RHIC is capable of colliding different ion beam species, ranging from protons to Uranium: Proton (p), Deuteron (d), Helium (He), Copper(Cu), Ruthenium (Ru), Zirconium (Zr), Gold (Au), and Uranium (U), at energies that can reach up to 100 GeV per nucleon (250 GeV for protons). Table 2.1 presents a summary of the various types of particle collisions conducted at the RHIC.

RHIC comprises two accelerator rings, both of which are 3.8 Km in circumference

[†]<https://www2.lbl.gov/Science-Articles/Archive/RHIC-first.html>

Particle species	$\sqrt{s_{NN}}$ (GeV)
Polarized $p + p$	200, 500
Polarized $p + {}^{27}\text{Al}^{13+}$	200
Polarized $p + {}^{197}\text{Au}^{79+}$	200
$d + {}^{197}\text{Au}^{79+}$	200
${}^3\text{He}^{2+} + {}^{197}\text{Au}^{79+}$	200
${}^{63}\text{Cu}^{29+} + {}^{63}\text{Cu}^{29+}$	22.4, 62.4, and 200
${}^{63}\text{Cu}^{29+} + {}^{197}\text{Au}^{79+}$	200
${}^{96}\text{Zr}^{40+} + {}^{96}\text{Zr}^{40+}$	200
${}^{96}\text{Ru}^{44+} + {}^{96}\text{Ru}^{44+}$	200
${}^{197}\text{Au}^{79+} + {}^{197}\text{Au}^{79+}$	7.7 – 200.0
${}^{197}\text{Au}^{79+} + {}^{197}\text{Au}^{79+}$ (fixed target)	3.0 – 7.7
${}^{238}\text{U}^{92+} + {}^{238}\text{U}^{92+}$	193

Table 2.1: Overview of RHIC Operations [70].

and contain a total of 1,700 superconducting magnets. These magnets allow RHIC to independently accelerate and collide different beam species and spin polarizations for protons. Figure 2.1 displays an aerial image of RHIC, showing its various components [71].

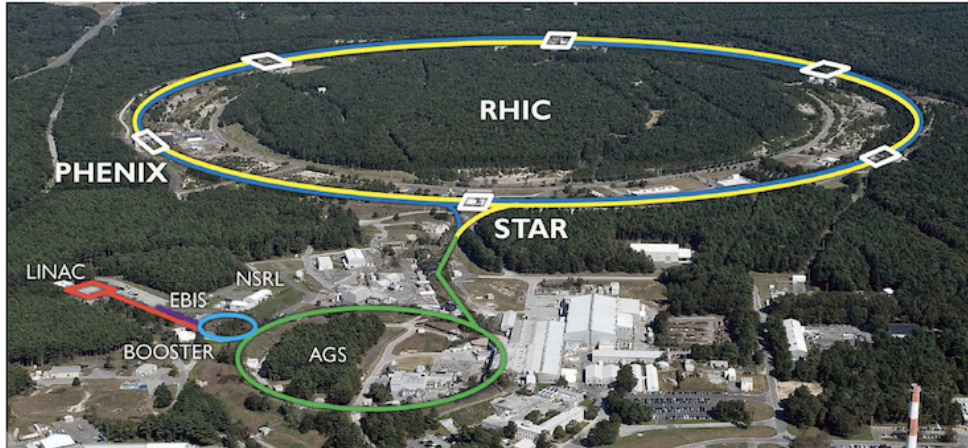


Figure 2.1: The RHIC facility as seen from an elevated viewpoint, showing the two experiments, STAR and PHENIX. Additionally, the injector complex is shown, which comprises LINAC for protons, the Electron Beam Ion Source (EBIS) for heavy ions, the Booster, and the AGS [71].

The flexibility and capabilities of RHIC make it the most advanced and adaptable collider in the world for conducting studies on extreme states of nuclear matter and the origin of the proton spin. The experimental setup of RHIC comprises accelerators, transfer lines, detectors, and computational resources for the purpose of storing and analyzing data. Figure 2.2 provides a schematic overview of the RHIC collider, illustrating the sequential steps of accelerating and colliding heavy ions [72]. The figure also provides a visual representation of the various stages of acceleration for heavy-ions and polarized protons. The sequential advancement of acceleration is detailed as follows. In the beginning, the

negatively charged Au ions are produced by pulse sputter ion source at the Tandem Van de Graaff. These ions undergo electron stripping using a foil at the high voltage terminal of Tandem. Subsequently, they are accelerated to 1 MeV/A in the second stage of the Tandem. Following additional electron stripping at the Tandem exit and a charge selection through bending magnets, beams of gold ions with a charge state of +32 are directed to the Booster Synchrotron.

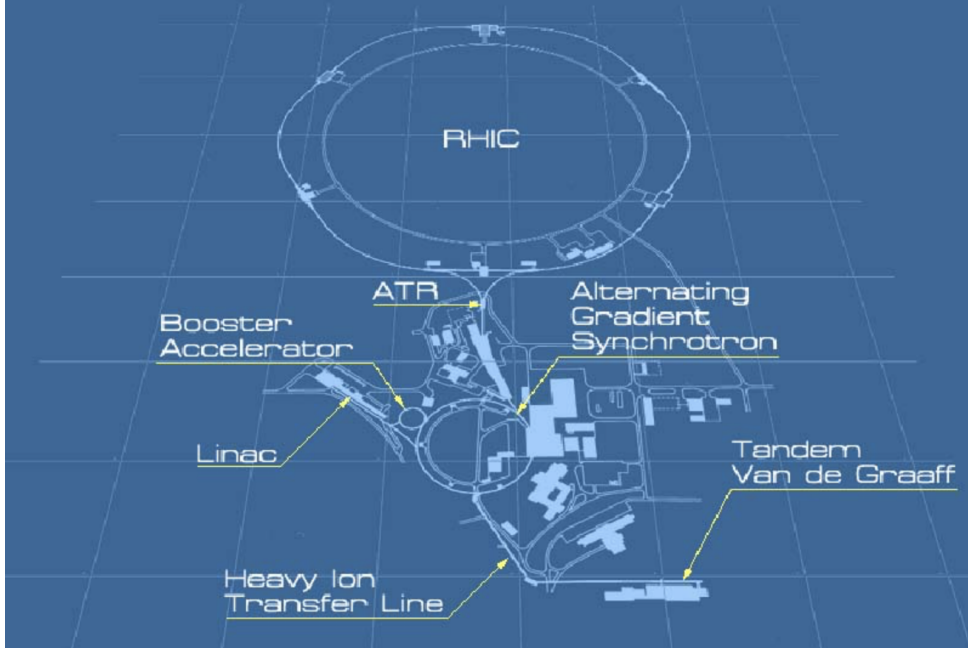


Figure 2.2: The schematic provides a visual representation of the sequence involved in introducing ions to the Relativistic Heavy Ion Collider (RHIC) [72].

The Booster Synchrotron accelerates the ions to 95 MeV per nucleon. Through additional stripping, the ions achieve a charge state of +77. They are sent to the Alternating Gradient Synchrotron (AGS) for acceleration to the injection energy of 10.8 GeV/A for RHIC. The AGS has a total of 24 ion bunches distributed throughout 4 Booster cycles. The bunches are then disassembled and reassembled into four bunches, and then accelerated, so that each bunch has ions equal to one Booster filling. At the AGS exit, Au ions are completely stripped, reaching a charge state of +79. After passing through a different beam line known as the AGS-To-RHIC (ATR) transfer line, the ion bunches reach the end where a switching magnet directs them either left, enabling clockwise travel in the RHIC ring, or right for anticlockwise travel in the second RHIC ring.

Another important aspect of RHIC is to provide beams of very high luminosities (L), which makes it possible to study rare processes with small cross sections. For a process with cross section σ_i , the event rate (R_i) is given by $R_i = \sigma_i \cdot L$. L is calculated as $L = f \cdot n \cdot N_1 \cdot N_2 / A$, where N_1 and N_2 are the number of particles contained in each bunch, A is the cross-sectional area of overlap between the two colliding beams, f is the

frequency of revolution, and n is the number of bunches per beam. High luminosity can be achieved by maximizing f and n .

2.2 STAR Experiment

STAR is an experimental facility that aims to investigate matter under extreme conditions, such as high temperature and energy density. STAR offers extensive coverage in η and full azimuthal coverage, enabling it to conduct research in heavy-ion physics as well as a spin physics program. STAR was mainly made to measure the production of hadrons over 4π -acceptance. It has detection systems for very accurate tracking, measuring particle momentum, and identifying particles at the center of mass rapidity. The 4π acceptance of the STAR detector makes it highly suitable for characterizing heavy-ion collisions on an event-by-event basis and for detecting hadron jets.

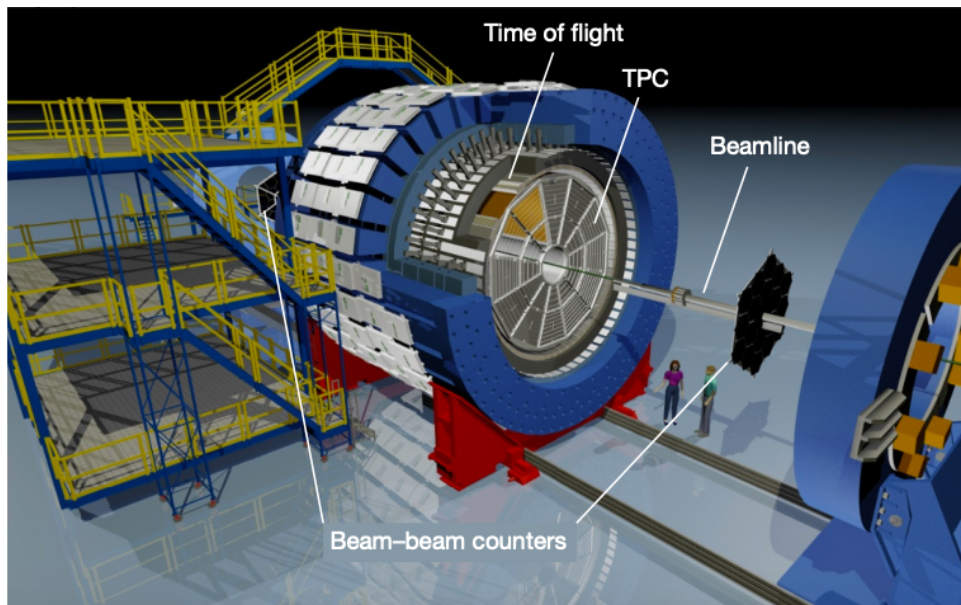


Figure 2.3: A schematic illustration of the STAR detector system [73].

Within the STAR detector, a variety of sub-detector systems play distinct roles in measuring different quantities. Figure 2.3 offers a perspective view of this complex system, ensconced in an expansive solenoidal magnet generating a constant 0.5 T magnetic field along the beam axis. This uniform magnetic field influences charged particle trajectories, enabling precise momentum measurements. Most of the sub-detectors measure full azimuthal coverage. Essential triggering detectors like the Zero Degree Calorimeters (ZDCs), Beam-Beam Counter (BBCs), and Pseudo Vertex-position-detector (VPDs) are strategically positioned on opposite sides from the detector center. These detectors facilitate event triggering, a crucial aspect of the data recording process. Two electromagnetic calorimeters, the Barrel Electromagnetic Calorimeter (BEMC) and the Endcap Electro-

magnetic Calorimeter (EEMC), are used for gauging energy deposition by electrons and photons during their interactions with matter. At the core of the STAR detector lies the Time-Projection-Chamber (TPC), a central component for tracking and particle identification. Another important detector, the Time-Of-Flight (TOF), supplements particle identification of high momentum particles. In the next section, an in-depth exploration of the TPC and TOF detectors and their specific roles in particle identification is presented.

2.2.1 Time Projection Chamber (TPC)

In the STAR experiment, TPC serves as the primary tool for tracking charged particles. It records their paths, measures their momenta, and identifies them by assessing the ionization energy loss per unit length (dE/dx) [74–76]. Covering a specific pseudorapidity region ($|\eta| < 1.8$) with complete azimuthal angle coverage, the TPC is proficient in measuring charged particle momenta within the range of 100 MeV/c to 30 GeV/c and effectively identifying particles over a momentum range of 100 MeV/c to 1 GeV/c. Figure 2.4 shows a visual representation of the STAR TPC. It has a tracking volume with a diameter of 4 m and a length of 4.2 m. The inner radius of the tracking volume starts at 50 cm, and the outer radius, 200 cm, covers an η interval of +1 unit. The TPC operates in a 0.5 T solenoidal magnetic field, which has been mapped with a precision of 1 to 2 G.

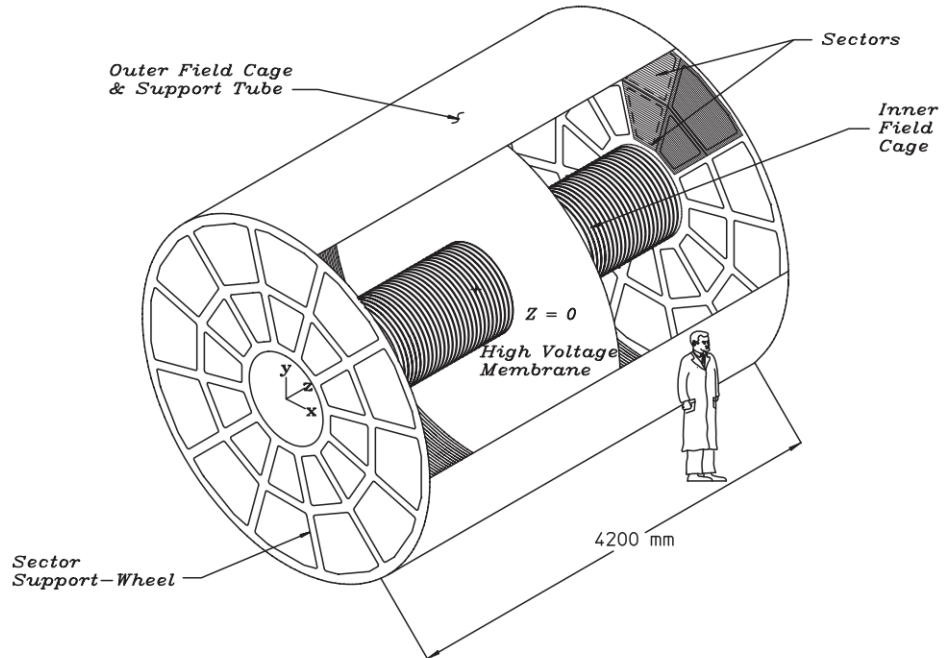


Figure 2.4: The STAR TPC encases the beam-beam interaction region at RHIC, with collisions occurring in close proximity to the central region of TPC [73].

TPC tracking volume is split into two halves along the beam direction, with a high voltage cathode located at the center. The central membrane operates at 28 kV, while

the end caps are grounded. Secondary electrons from tracks drift towards either end of the TPC depending on their point of origin. The drifting electrons are amplified by a grid of wires on each end, and the pulses are read out on small pads placed behind the anode wires. Each sector of the TPC readout planes is composed of an inner and an outer sub-sector. The inner sub-sector has smaller pad sizes and a wire plane separation of 2 mm, while the outer sub-sector has larger pads and a wire plane separation of 4 mm. The goal is to achieve a signal-to-noise ratio of 20:1 in both sectors, with a net gain of about 1100 on the outer sector and 3000 on the inner sector. The TPC is operated with P10 gas (90% Argon, 10% Methane), and a 150 cm path through the gas is equal to 1.17% of the radiation length. The field cages, which define the electric field inside the TPC, are lightweight cylinders of Nomex honeycomb sandwiched between two layers of Kapton. There are 364 rings in each field cage, with a width of 110 mm and separated by a 1.5 mm gap.

During phase II of the Beam Energy Scan program, the inner sectors of the TPC were upgraded as part of the i-TPC upgrade. The number of pad rows in each inner sector increased from 13 to 40. This upgrade extended the pseudo-rapidity coverage from $|\eta| < 1$ to $|\eta| < 1.6$. With 32 pad rows in the outer sector, a track can now have a maximum of up to 72 hits. This significant increase in the number of hits, particularly from the inner sector, has improved momentum resolution and lowered the minimum momentum threshold from $p_T = 0.15 \text{ GeV}/c$ to $p_T = 0.06 \text{ GeV}/c$.

2.2.1.1 Track Reconstruction in TPC

The TPC readout system, utilizing Multi-Wire Proportional Chambers (MWPC) with readout pads, is structured with a pad plane and three wire planes. Organized into 24 sectors, each containing 12 readout sectors per end cap, these sectors are further divided into inner and outer sectors. Figure 2.5 shows the pad plane of a TPC sector, which is divided into inner and outer sections. The inner sector, featuring 13 small, widely spaced pad rows, maximizes two-track resolution in high particle density areas. Conversely, the outer sector comprises 32 large, densely packed pad rows, optimizing ionization energy loss in regions with smaller particle populations. This configuration allows for a maximum of 45 hits on a track that traverses all pad rows.

The STAR TPC is capable of track reconstruction, presenting a track as a 3D image with x, y, and z-coordinates at each point. Within the TPC volume, charged particles ionize gas atoms, creating electron arrays. The x and y-positions are derived from adjacent pads along a single pad row, while the z-position involves drift time measurement. A helical fit uses x, y, and z-coordinates to determine a particle trajectory. Deviations from the helical shape, induced by energy loss and scattering, are rectified in a global track using information from inner detectors with the Kalman fit method. Back extrap-

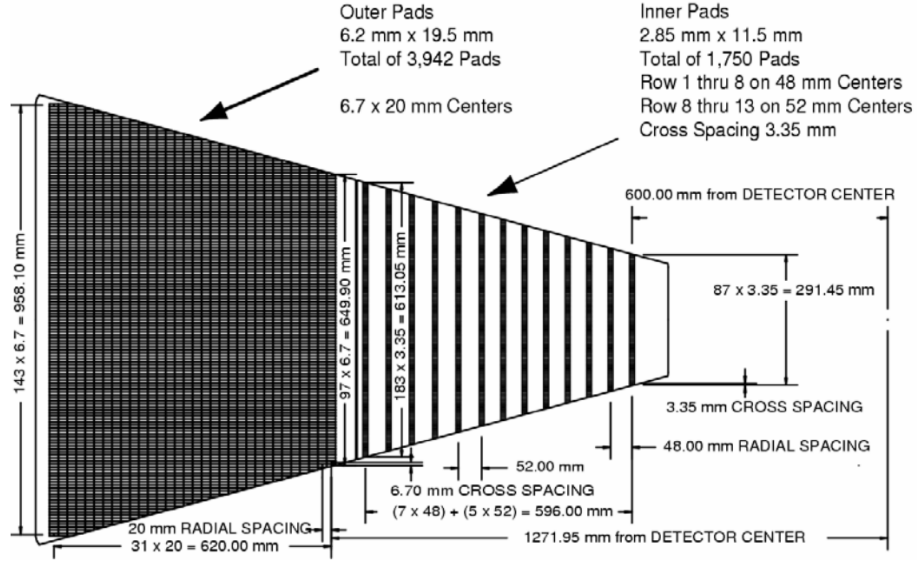


Figure 2.5: The arrangement of a TPC anode sector is depicted in the figure sourced from Ref [77]. The diagram illustrates a sector of the TPC anode plane, showcasing both inner and outer subsectors, along with their corresponding padrows.

olation determines the z-position of the primary collision vertex. Tracks with a Distance of Closest Approach (DCA) less than 3 cm undergo refitting, becoming primary tracks. Reconstruction efficiency varies based on particle type, track quality cuts, and track density.

2.2.1.2 Particle Identification in TPC

TPC effectively shows its ability to identify charged particles by precisely measuring ionization energy loss inside. Despite the potential for a particle track to yield 45 dE/dx points across 45 pad rows, challenges arise due to notable ionization fluctuations and the shorter trajectory for dE/dx measurement. Consequently, it is preferable to use the most probable dE/dx instead of the average, achieved by determining the truncated mean of the 70% electron cluster and excluding 30% of larger ionization clusters. The mathematical expression for ionization energy loss uses the Bichsel function [78], an extension of the Bethe-Bloch formula given in Eq. 2.1 [79], which shows the mass dependence crucial for particle identification:

$$-\frac{dE}{dx} = Kz^2 \frac{Z}{A} \frac{1}{\beta^2} \left[\frac{1}{2} \ln \left(\frac{2m_e c^2 \beta^2 \gamma^2 T_{max}}{I^2} \right) - \beta^2 - \frac{\delta^2}{2} \right], \quad (2.1)$$

In the given formula, several symbols play essential roles in characterizing the absorption of radiation in a material. The atomic mass (A) and atomic number (Z) of the absorber define its fundamental properties, reflecting the mass and charge distribution within the material. The track radius of the electron and mass (m_e) contribute to the overall in-

teraction process, representing the spatial extent and mass of the electrons involved in the absorption. The maximum energy transfer (T_{\max}) denotes the maximum amount of energy transferred from the incident particle to the absorber during its absorption. The mean excitation energy (I) provides insight into the average energy required to create an electron-ion pair, offering a measure of the absorber response to ionization. The correction due to the density effect (ρ) accounts for variations in material density, influencing the overall absorption characteristics. Together, these quantities collectively describe the complex interplay of factors influencing the absorption of radiation within a material.

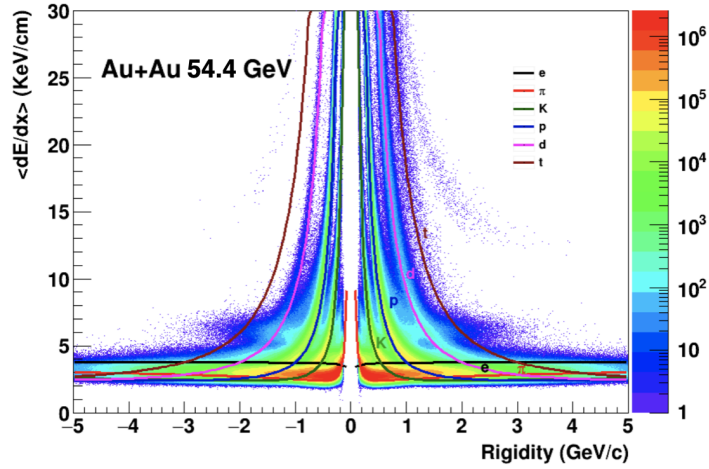


Figure 2.6: Ionization energy loss of primary and secondary particles within the STAR TPC as a function of rigidity in Au+Au collisions at $\sqrt{s_{NN}} = 54.4$ GeV.

Figure 2.6 represents the ionization energy loss of primary and secondary charged particles inside the TPC in STAR, depicting dense bands reflecting the ionization energy loss of the charged particles. The solid lines signify theoretical predictions from the Bichsel function. For qualitative particle identification, the $n\sigma$ variable, measuring the standard deviation, proves reliable. It is defined by comparing the measured and expected values of $\langle dE/dx \rangle$, considering the particle type and dE/dx resolution (R) of the TPC. The $n\sigma$ variable, providing a qualitative assessment. The $n\sigma$ is defined as:

$$n\sigma_i = \frac{1}{R} \log \frac{\langle dE/dx \rangle|_{\text{measured}}}{\langle dE/dx \rangle_i|_{\text{expected}}} \quad (2.2)$$

where i represents the particle type under consideration (e.g., e , π , K , p , etc.), $\langle dE/dx \rangle|_{\text{measured}}$ signifies the observed energy loss of the particle, $\langle dE/dx \rangle_i|_{\text{expected}}$ denotes the mean energy loss derived from the Bichsel function for that specific particle.

In the context of this thesis, the z variable is chosen for particle identification using the TPC. Which is defined as,

$$z_i = \ln \left(\frac{\langle dE/dx \rangle|_{\text{measured}}}{\langle dE/dx \rangle_i|_{\text{expected}}} \right) \quad (2.3)$$

2.2.2 Time-Of-Flight (TOF)

The Time-Of-Flight (TOF) detector in the STAR experiment extends particle identification capabilities beyond the momentum range measured by TPC [80]. It comprises two subsystems: the pseudo Vertex Position Detector or pVPD (start detector) and TOF (stop detector), both using scintillator or phototube technology with custom electronics. The TOF detector, positioned just above the TPC, envelops it with a slightly reduced pseudo-rapidity acceptance of $|\eta| < 0.9$ with full azimuthal coverage. It consists of a total of 120 trays evenly distributed, with 60 on each side. In 2010, STAR underwent an upgrade to a complete barrel TOF detector, incorporating Multigap Resistive Plate Chamber (MRPC) technology [81]. Each TOF tray had 32 MRPC modules covering 6° in the azimuthal direction around the TPC. The MRPC is essentially a stack of resistive plates with gap filled with gas between adjacent plates. High voltage is applied to both sides of the outer plates, creating a strong electric field in the sub-gaps between the plates. As the plates are resistant to signal avalanche, the induced signal on the collecting plate is the sum of signals from all the gaps. Figure 2.7 provides a cross-sectional view of the MRPC module, displaying its long and short sides along with their respective dimensions [82].

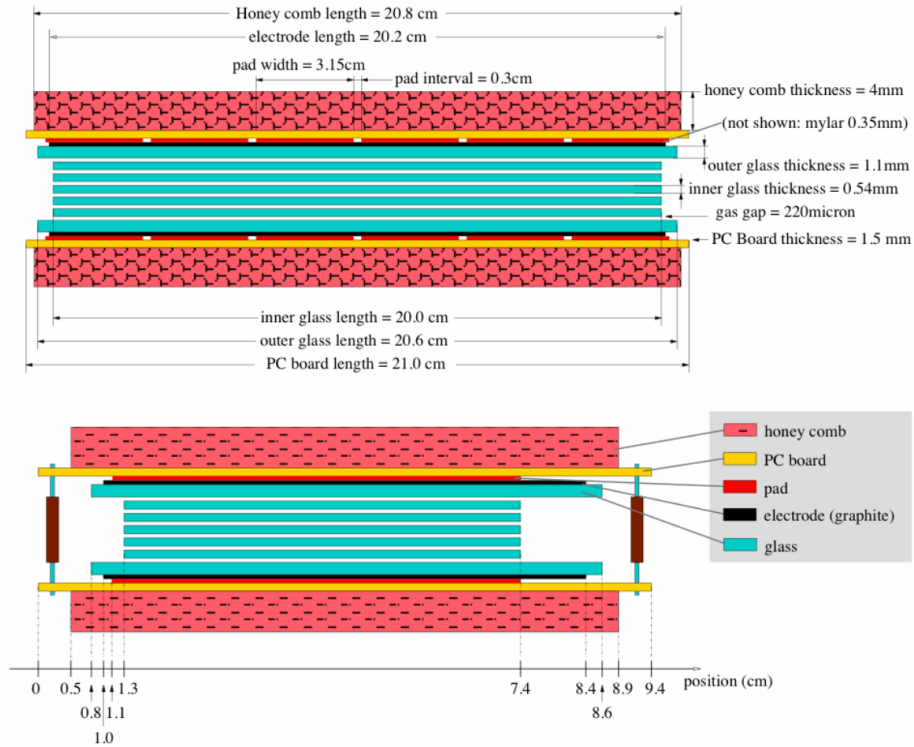


Figure 2.7: Two distinct views shows the structure of an MRPC module, with the upper view emphasizing the long edge and the lower view focusing on the short edge. It is important to note that these two perspectives are not depicted at identical scales [82].

Two identical pVPDs are symmetrically positioned on both sides, equidistant from

the center of the beam pipe at a distance of 5.7 m. Their η coverage is from 4.24 to 5.1, with 19 channels on each side. These detectors play a crucial role in providing the start time information for TOF events and independently determining the z-component of the collision vertex. The combined information from TOF and pVPDs is used to calculate the time interval (Δt). For particle identification, we use the path length (l) and momentum (p) information from TPC. The inverse of velocity is then determined by $1/\beta = c\Delta t/l$, where c is the speed of light. Figure 2.8 illustrates the representative figures showing $1/\beta$ as a function of momentum in $Au + Au$ collisions at $\sqrt{s_{NN}} = 54.4$ GeV in STAR.

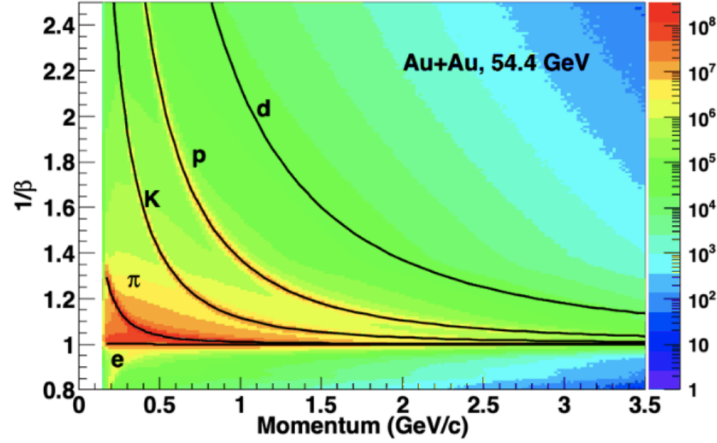


Figure 2.8: The variation of $1/\beta$ with momentum is examined using TOF in $Au + Au$ collisions at $\sqrt{s_{NN}} = 54.4$ GeV at STAR.

Inferred from Figure 2.8, $1/\beta$ bands are distinctly separated up to a momentum of 2 GeV/c for pions, kaons, and protons. This TOF information is effectively utilized for identifying pions, kaons, and protons within a transverse momentum range of 2 GeV/c.

2.2.3 Trigger Detectors

The STAR trigger system [83] monitors each beam crossing in RHIC, applying specific criteria to determine whether to accept a collision event and initiate data recording. RHIC interaction rates can reach approximately 10 MHz at the highest luminosity. However, the majority of STAR data is recorded by slow detectors operating at rates around 100 Hz. Consequently, the trigger system utilizes input from fast detectors to govern event selection for recording by the much slower tracking detectors. Key trigger detectors at STAR include the Zero Degree Calorimeters, the Beam Beam counters, the Vertex Position Detectors, and the ElectroMagnetic Calorimeters.

2.2.3.1 Zero Degree Calorimeters (ZDC)

The Zero Degree Calorimeters (ZDCs) [84], common to all RHIC experiments, consist of pairs on each side near DX dipole magnets. Positioned 18 m from the interaction point

with ± 5 cm horizontal acceptance, ZDCs serve dual roles: counting spectator neutrons and providing a coincident signal for luminosity monitoring [85]. They determine the collision vertex with 100 ps time resolution. Two Shower Maximum Detectors (SMDs) positioned between ZDC modules study the spatial distribution of neutron hits. ZDC-SMD helps to study the anisotropic flow, ultra-peripheral collisions, and spin physics [86].

2.2.3.2 Beam-Beam Counter (BBC)

The ZDCs are designed for triggering high particle multiplicity events in Au+Au collisions. However, for lower multiplicity p+p collisions, the more reliable Beam Beam Counter (BBC) is employed. Positioned 3.75 m away from the nominal interaction point at the east and west pole tips of the STAR magnet, each BBC comprises two rings of hexagonal scintillator tiles. The outer ring consists of large tiles, while the inner ring is made up of smaller tiles as shown in Fig. 2.9. The inner ring, with an inner diameter of 9.6 cm and an outer diameter of 48 cm, features a 2×18 array of small hexagonal tiles, covering a pseudo-rapidity range of $3.4 < \eta < 5.0$. The outer ring contains a 2×18 array of larger tiles, with inner and outer diameters of 38 cm and 193 cm, respectively, corresponding to a pseudo-rapidity range of $2.1 < \eta < 3.6$. When a charged particle passes through the BBCs, it produces light in the scintillator tiles. The coincidence rate of the BBCs provides the minimum bias trigger required for p+p collisions. Additionally, BBC measures the absolute luminosity (L) with 15% precision and relative luminosity (R) for different proton spin orientations. The small tiles are used for reconstructing the first-order event plane in anisotropic flow analysis, and the time difference between the two counters determines the primary vertex position.

2.2.3.3 Vertex Position Detectors (VPD)

Since 2009, the two Vertex Position Detectors (VPDs) [88] have been employed in triggering events during high-energy heavy-ion collisions. Positioned on both sides of the STAR, these VPD pairs are located 5.7 m away from the center of the interaction point, covering a pseudo-rapidity range of $4.24 < |\eta| < 5.1$. Each VPD is composed of 19 lead converters and plastic scintillators equipped with PMT readout.

The coincidence rate between the east and west VPDs serves as a source for minimum biased triggered events. Furthermore, the time difference between coincident events from the east and west VPDs provides precise information regarding the location of the primary vertex position. Notably, VPDs achieve a significantly better timing resolution compared to BBCs.

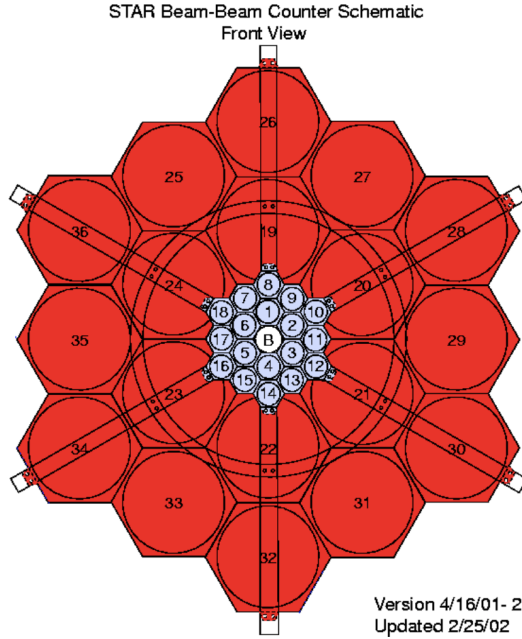


Figure 2.9: The diagram shows the Beam-Beam Counter with small blue and large red tiles, the beam pipe crossing at the center marked by the symbol B [87].

2.2.3.4 ElectroMagnetic Calorimeters (EMCs)

The STAR detector incorporates two electromagnetic calorimeters: the Barrel Electromagnetic Calorimeter and the Endcap Electromagnetic Calorimeter. These calorimeters play an important role in the event-triggering process, particularly for events involving rare probes and high- p_T processes. Such events are often characterized by significant electromagnetic energy deposition in the EMC towers or patches, originating from jets, leading hadrons, direct photons, and heavy quarks. Furthermore, electromagnetic calorimeters contribute significantly to the characterization of ultra-peripheral collision events. These calorimeters serve as valuable tools for understanding the intricacies of such collision events and their associated phenomena. The schematic showing the side view of the BEMC and the end view of the EEMC is presented in Fig. 2.10[†].

Barrel Electromagnetic Calorimeter (BEMC)

The Barrel Electromagnetic Calorimeter [89] is designed to fully cover the STAR TPC with an area of approximately 60 m², providing full azimuthal coverage and pseudo-rapidity acceptance within $|\eta| < 1$. The BEMC is a sampling calorimeter, consisting of alternating layers of lead and scintillator, with 20 layers of each material. It is divided into 120 modules—60 on the east side and 60 on the west side—each covering 6 degrees in $\Delta\phi$ and 1.0 unit in $\Delta\eta$. Each module is further segmented into 40 towers, arranged as

[†]<https://www.star.bnl.gov/public/trg/.introduction/index.html#eemc>

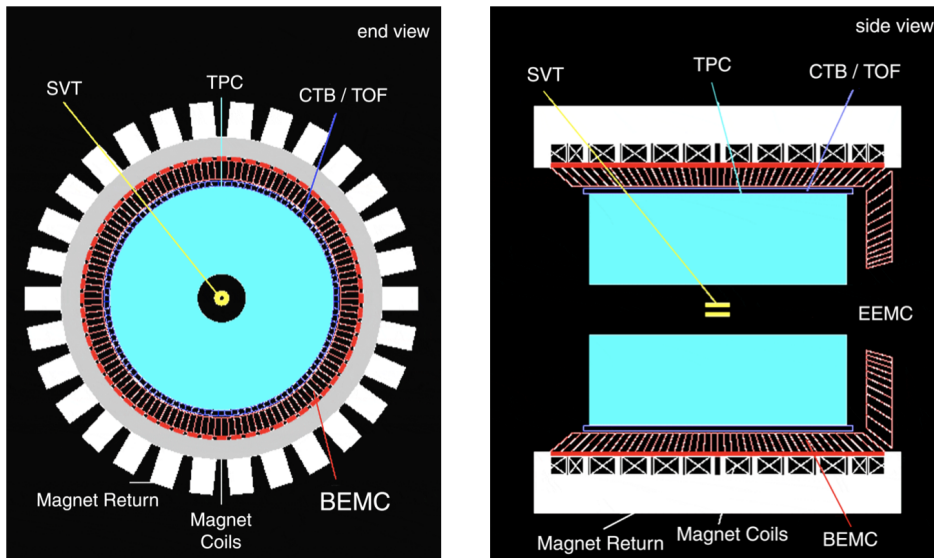


Figure 2.10: End view of Barrel EMC and side view of Endcap EMC.

2 in ϕ and 20 in η , giving each tower a span of 0.05×0.05 in $\eta - \phi$ space. For triggering purposes, the towers are grouped into sets of 16 to form 300 trigger patches, each covering 0.2×0.2 in $\eta - \phi$. In total, the BEMC consists of 4800 towers that project back to the interaction region. Each tower contains lead-scintillator layers, and a Shower Maximum Detector (SMD) is placed at approximately 5 radiation lengths (X_0) from the front of the lead-scintillator bundle to provide fine spatial resolution.

The BEMC measures neutral energy by detecting photons produced in the interaction, which initiate particle cascades upon entering the calorimeter. The energy deposited in individual towers or groups of towers can be used to trigger high- p_T events. This enables the reconstruction of π^0 mesons at relatively high transverse momentum (25-30 GeV/c) and the identification of single electrons and electron pairs amidst dense hadron backgrounds from W and Z boson decays.

Endcap Electromagnetic Calorimeter (EEMC)

The Endcap Electromagnetic Calorimeter is installed within the west STAR magnet pole tip, covering the pseudo-rapidity range of $1 \leq \eta \leq 2$ with full azimuthal coverage [90]. It extends and supplements the rapidity coverage provided by the BEMC. Similar to the BEMC, the EEMC is a lead-scintillator sampling electromagnetic calorimeter, consisting of 720 individual towers, each sized either 0.05×0.1 or 0.1×0.1 in the $\eta - \phi$ plane. These towers are organized into 90 trigger patches, each covering 0.3×0.2 in the $\eta - \phi$ plane. The EEMC also features a Shower Maximum Detector (SMD) to enhance its capacity to distinguish between photons and π^0 or η mesons in the 10-40 GeV energy range. Furthermore, pre-shower and post-shower layers are incorporated to aid in differentiating

electrons from hadrons. The acceptance of EEMC enhances the ability of the STAR detector to detect photons, π^0 , η mesons, and to distinguish electrons, positrons, and high- p_T particles and jets.

Chapter 3

Identified Particle Production in Au+Au Collisions at $\sqrt{s_{\text{NN}}} = 54.4$ GeV in the STAR Experiment

3.1 Introduction

RHIC at BNL aims to probe the properties of QGP medium [28, 91–93]. One of the primary goals of RHIC is to explore the conjectured QCD phase diagram, investigating the relationship between temperature T and baryon chemical potential μ_B . Predictions from Lattice QCD calculations suggest a crossover near zero μ_B and a first-order phase transition line at higher μ_B . The end point of the first-order phase transition line is believed to be a second-order phase transition point, commonly referred to as the QCD critical point. To achieve these scientific goals, RHIC initiated the first phase of the Beam Energy Scan (BES-I) program in 2010 [94–104].

This phase involved Au+Au collisions at center-of-mass energies ranging from 7.7 to 62.4 GeV. The BES-I program was successful, leading to the launch of the second phase, Beam Energy Scan (BES-II), which ran from 2017 to 2021. During BES-II, Au+Au collision data were recorded at center-of-mass energies between 7.7 and 54.4 GeV, allowing the exploration of a large part of the QCD phase diagram. The BES-II covered various T and μ_B by changing the collision energy, centrality, and rapidity. In 2017, the STAR experiment at RHIC collected a high statistics dataset from Au + Au collisions at $\sqrt{s_{\text{NN}}} = 54.4$ GeV. This targeted dataset was designed to bridge a notable energy gap that existed between 39 and 62.4 GeV. The p_T -spectra of identified hadrons are crucial for understanding the bulk properties of the produced medium. These properties include the integrated yield (dN/dy), the average transverse momentum ($\langle p_T \rangle$), particle yield ratios, and the characteristic of the system at kinetic freeze-out. The systematic study of these bulk properties can provide valuable insights into the mechanisms of particle pro-

duction and the evolution of the system resulting from heavy-ion collisions. This thesis chapter focuses on the analysis of data from Au+Au collisions at $\sqrt{s_{NN}} = 54.4$ GeV. The analysis begins with the identification of π^+ , K^+ , p and their anti-particles, followed by the measurement of their p_T -spectra. Essential observables, including $\langle p_T \rangle$, dN/dy , and various particle ratios, are extracted from these spectra. These observables form the basis for probing the freeze-out properties of the medium, examined as functions of collision centrality and energy.

3.1.1 Data Set and Analysis Selection Criteria

The dataset used in the presented analysis is taken from Au+Au collisions at $\sqrt{s_{NN}} = 54.4$ GeV, collected in 2017 using the STAR detector at RHIC. This dataset was collected using a minimum bias trigger, defined by a coincidence of hits in the ZDCs [105], VPDs [106], and/or BBCs. The VPD helps us find the vertex z position by measuring the time difference between signals detected on its east and west sides. This careful process ensures that we choose the right events for our analysis.

3.1.1.1 Event Selection

The primary vertex for each minimum-bias event was determined by identifying the best common origin of tracks measured in the TPC. Given the symmetric nature of the STAR TPC, we prioritized events with primary vertices near the center ($z = 0$). This selection maximizes the distance traveled by particles within the TPC, improving reconstruction accuracy. The x and y coordinates of the event vertex were obtained through track and vertex reconstruction, while the z -coordinate was calculated based on the drift length, determined by multiplying the drift time by the drift velocity. The drift velocity was calibrated using a TPC laser before each run [107].

For this analysis, we focused on events with primary vertex z -positions (V_z) within ± 30 cm of the TPC center along the beamline. To eliminate contributions from beam-gas and beam-material interactions, we also restricted the events to within a 2 cm radius from the origin of the vertex distribution. This circular cut is defined by $V_r = \sqrt{V_x^2 + V_y^2}$, where V_x and V_y represent the vertex positions along the x and y axes. The beam-pipe radius is 3.81 cm. With these criteria and a minimum-bias trigger, we selected ~ 512 million high-quality minimum-bias events. The distributions of V_z and V_y vs V_x for Au+Au collisions at $\sqrt{s_{NN}} = 54.4$ GeV are illustrated in Fig. 3.1. Event cuts that yield a significant number of events after application are listed in Table 3.1.

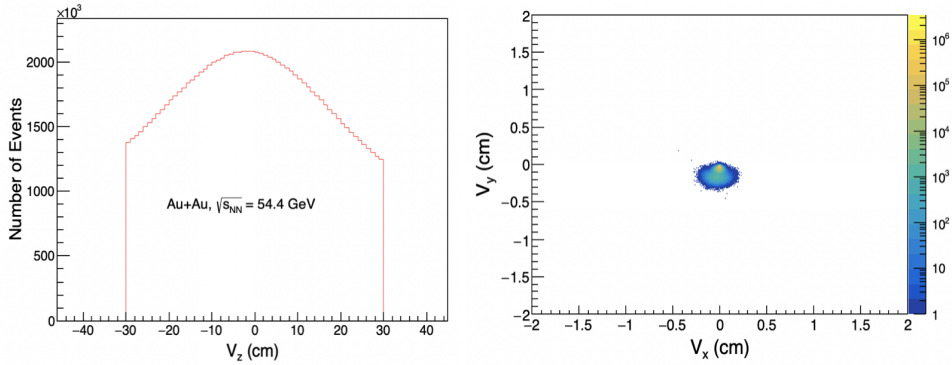


Figure 3.1: Distribution of the z-component of the vertex (V_z) (left panel) and the V_y versus V_x distributions (right panel) after applying all event cuts in Au+Au collisions at $\sqrt{s_{NN}} = 54.4$ GeV in the STAR experiment.

Table 3.1: Trigger Id and Event cuts

Cut	Value	No. of Events after the cut
Trigger Id	580001 580021	
$ V_z $	< 30 cm	~ 512 M (After bad run rejection, V_z and V_r cut)
V_r	< 2 cm	

3.1.1.2 Track Selection

We employed track selection criteria similar to those used in previous STAR analyses [108]. For this analysis, only primary tracks were considered, with optimal cuts applied to minimize contamination from secondary tracks. To reduce contributions from the secondary vertex, the Distance of Closest Approach (DCA) of the track to the collision vertex was limited to 3 cm or less. Additionally, we applied a criterion based on the number of fit points, requiring that each track have more than 25 fit points (nHitsFit) to prevent the inclusion of split tracks. Tracks passing through the TPC can have up to 45 possible hits. The fraction of points used in the fit must be greater than 52% of the total possible fit points (nHitsPoss) to avoid counting split tracks as multiple tracks. To ensure good $\langle dE/dx \rangle$ resolution, the number of hits used to calculate $\langle dE/dx \rangle$ was required to exceed 15. The analysis was performed within a rapidity window of $|y| < 0.1$. The track selection criteria used for Au+Au collisions at $\sqrt{s_{NN}} = 54.4$ GeV are detailed in Table 3.2.

Source	Value
$ y $	< 0.1
DCA (cm)	< 3.0
nHitsFit	> 25
nHitsFit/nHitsPoss	> 0.52
ndEdx	> 15

Table 3.2: Track Selection Criteria for Tracks in Au+Au Collisions at $\sqrt{s_{NN}} = 54.4$ GeV

3.1.1.3 Centrality Selection

The centrality of an event, which reflects the overlap between colliding nuclei, depends on the impact parameter (b). Centrality is determined experimentally using the reference multiplicity (N_{ch}), which is defined as the number of charged tracks in the TPC that meet specific criteria, including having at least 10 fit points, a pseudo-rapidity of $|\eta| < 0.5$, and a DCA of less than 3 cm. The measured N_{ch} is compared with the simulated multiplicity density, calculated using a two-component Monte Carlo (MC) Glauber Model [109, 110], and is defined as follows:

$$\frac{dN_{\text{ch}}}{d\eta} = n_{pp} \times ((1 - x) \times N_{\text{part}} + x \times N_{\text{coll}})$$

Here, n_{pp} represents the average number of charged particles produced in minimum-bias p+p collisions, and x is the fraction of the hard component. N_{part} refers to the total number of nucleons that experience at least one collision, and N_{coll} is the number of binary nucleon-nucleon collisions. The values of N_{part} , N_{coll} , and b can be calculated using the Glauber model [109, 110], which is a geometrical model of nucleus-nucleus collisions.

To account for event-by-event variations in multiplicity, the Negative Binomial Distribution (NBD) is convoluted with N_{part} and N_{coll} . The NBD distribution in multiplicity n is characterized by two parameters, n_{pp} and k , and is defined as:

$$P_{\text{NBD}}(n_{pp}, k; n) = \frac{\Gamma(n + k)}{\Gamma(n + 1)\Gamma(k)} \left(\frac{n_{pp}}{k}\right)^n \left(\frac{n_{pp}}{k} + 1\right)^{-n-k},$$

where Γ is the Gamma function. The parameters n_{pp} and k are obtained by fitting the measured multiplicities to those from the simulations. This fitting process is typically performed for multiplicities greater than a certain threshold to avoid trigger inefficiency in peripheral collisions. Centrality classes are then defined by calculating the fraction of the total cross-section obtained from the simulated multiplicity. The criteria for centrality selection used in this analysis are detailed in Ref. [111].

Figure 3.2 shows the measured uncorrected multiplicity distribution for charged particles from the TPC in Au+Au collisions at $\sqrt{s_{NN}} = 54.4$ GeV. It illustrates the distribution of Reference Multiplicity categorized into nine distinct centrality classes: 0-5%, 5-10%, 10-20%, 20-30%, 30-40%, 40-50%, 50-60%, 60-70%, and 70-80%. These centrality classes were established using the StRefMultCorr class, specifically developed for STAR datasets from the year 2010 onwards.

3.2 Particle Identification

In the STAR experiment, charged particle identification is performed utilizing the TPC [77] and TOF detectors, depending on the momentum of the particle. For low momentum

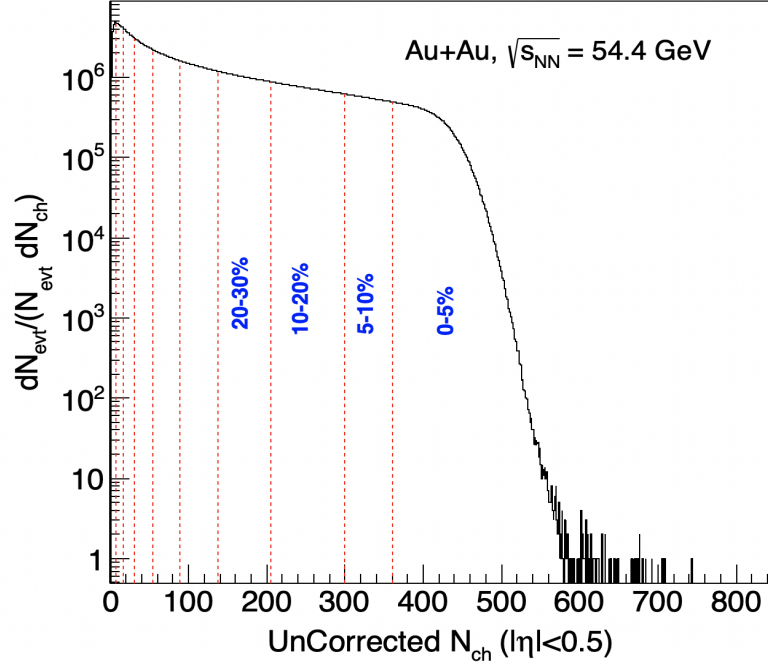


Figure 3.2: The distribution of charged particle multiplicity (not corrected for efficiency and acceptance) measured by the TPC within $|\eta| < 0.5$ in Au+Au collisions at $\sqrt{s_{NN}} = 54.4$ GeV in the STAR experiment. The vertical lines represent the centrality selection criteria employed. Errors are statistical.

particles, the TPC is used, while for particles with intermediate or high momenta ($p_T > 1$ GeV/c), the TOF is used. The TPC exhibits exceptional capabilities in particle tracking and identification, especially within the low-momentum range.

Figure 3.3 illustrates this characteristic plot in Au+Au collisions at $\sqrt{s_{NN}} = 54.4$ GeV, depicting $\langle dE/dx \rangle$ as a function of charge/momentum (p/q) known as rigidity. Various particles fall within a specified band of $\langle dE/dx \rangle$ around their expectation values from the Bichsel function, indicated by solid curves in the figure.

The TPC uses the ionization energy loss (dE/dx) for particle identification, from which the variable z is defined:

$$z_i = \ln\left(\frac{\langle dE/dx \rangle}{\langle dE/dx \rangle_i^B}\right),$$

where $\langle dE/dx \rangle_i^B$ is the expected energy loss based on the Bichsel function and “ i ” is the particle type (e^\pm , π^\pm , K^\pm , p, or \bar{p}).

The most likely value of z_i for particle “ i ” is determined to be 0. The z_i distribution is specifically constructed for a particular particle type within a given p_T bin, where the rapidity ($|y|$) is limited to less than 0.1. Figure 3.4 provides an illustrative representation

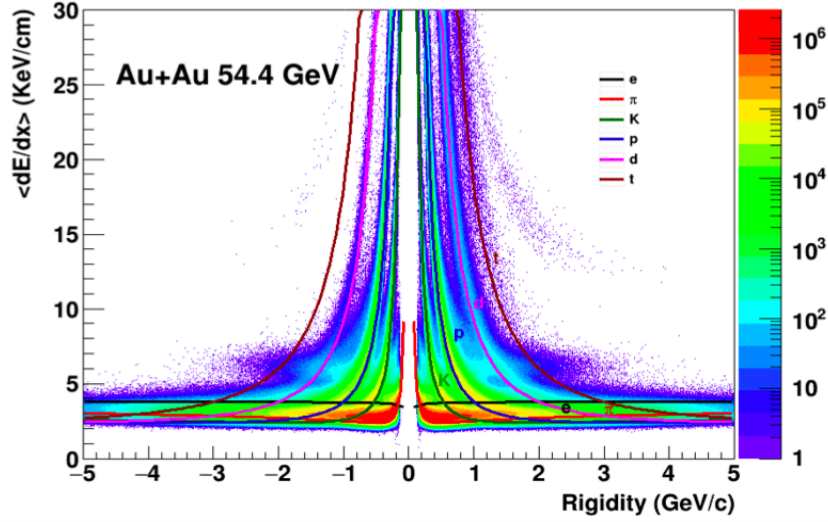


Figure 3.3: The distribution of specific energy loss ($\langle dE/dx \rangle$) of charged particles as a function of momentum-to-charge ratio (p/q) obtained from the TPC in Au+Au collisions at $\sqrt{s_{NN}} = 54.4$ GeV. The curves represent the expected mean value of dE/dx for the corresponding particle.

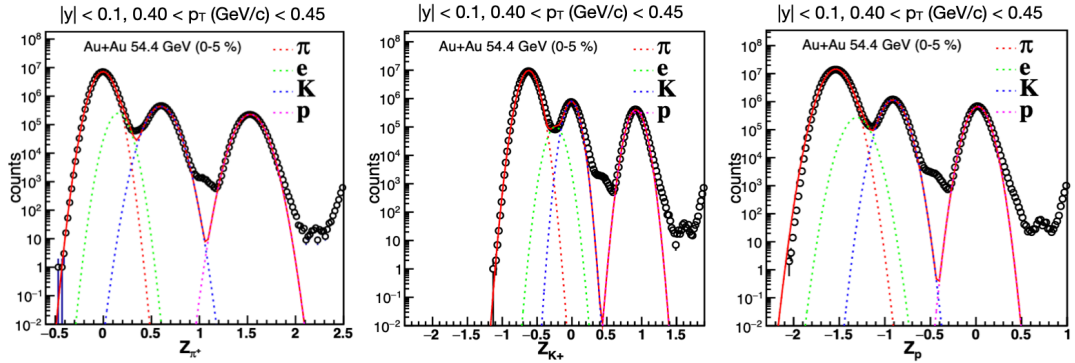


Figure 3.4: The z_{π} , z_K , and z_p distributions of π^+ , K^+ , and p at mid-rapidity ($|y| < 0.1$) for p_T range 0.40-0.45 GeV/c in 0-5% centrality from TPC in Au+Au collisions at $\sqrt{s_{NN}} = 54.4$ GeV. The curves represent Gaussian fits corresponding to contributions from pions, electrons, kaons, and protons. The uncertainties are purely statistical.

of the z_{π} , z_K , and z_p distributions for positively charged particles across various p_T bins in central Au+Au collisions at a center-of-mass energy of $\sqrt{s_{NN}} = 54.4$ GeV.

In order to calculate the raw yields within a given p_T bin, a fitting technique involving a multi-Gaussian function is applied to the z_X distributions, as shown in Fig. 3.4. The area under the Gaussian curve corresponding to the particle of interest, identified by its centroid at zero, provides the yield of that particular particle within the specified p_T bin.

At lower p_T values, the peaks of the pion, kaon, and proton distributions are distinctly separated. However, as the p_T increases, these distributions gradually begin to overlap as shown in Fig. 3.5. In this overlapping p_T region, the sigma values of the Gaussian fits are constrained by the values obtained from the lower p_T bins. This approach is employed to ensure the accurate extraction of particle yields, particularly in situations where the

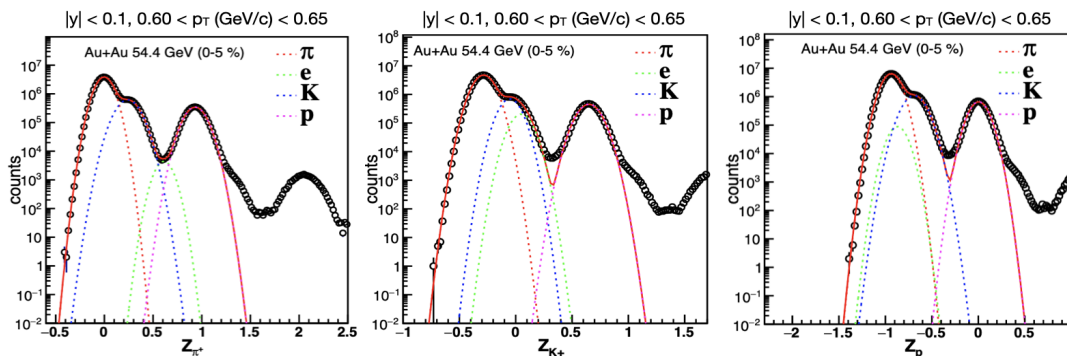


Figure 3.5: The z_π , z_K , and z_p distributions of π^+ , K^+ , and p at mid-rapidity ($|y| < 0.1$) for p_T range 0.60-0.65 GeV/c in 0–5% centrality from TPC in Au+Au collisions at $\sqrt{s_{NN}} = 54.4$ GeV. The curves represent Gaussian fits corresponding to contributions from pions, electrons, kaons, and protons. The uncertainties are purely statistical.

distributions of different particle types coincide, necessitating a careful consideration of the constrained sigma values from lower p_T regions.

It is observed that the dependence of $\langle dE/dx \rangle$ on particle mass weakens with increasing particle momentum. The $\langle dE/dx \rangle$ bands of π^\pm , K^\pm , and $p(\bar{p})$ start merging around 1.0 GeV/c, limiting pion and kaon identification to 0.8 GeV/c and proton identification up to 1.0 GeV/c using this approach. To address this issue, the Time of Flight detector is used for intermediate p_T particles with momentum greater than 1.0 GeV/c.

3.3 Correction Factors

The raw spectra are calculated using $d^2N/(2\pi p_T dp_T dy)$ for each p_T bin. Some particles might not be detected in the STAR TPC due to its geometry. Particles can also hit dead regions of the detector, or tracks might not be accurately reconstructed if some hits are missing. As a result, the raw spectra need to be corrected for detector acceptance, track reconstruction inefficiency, hadronic interactions, and the decay of resonance particles. These corrections are done using a method called the embedding technique.

GEANT is very useful to study the detector effects [112]. GEANT is a software framework designed to realistically simulate the passage of particles through matter. The various components (including structural) of the STAR detector and its subsystems are modeled in GEANT3. Monte Carlo tracks can then be sent through the model to evaluate how the detector responds to the tracks and how tracks respond as they transit the detector. In STAR, this process is known as “embedding” because it involves embedding Monte Carlo generated tracks into real data. These tracks then pass through GEANT simulation. We use the terms embedded track, reconstructed track, and matched track in the following way. An embedded track is a particle of a defined species whose kinematic properties were generated from a Monte Carlo model. Often the embedded tracks are

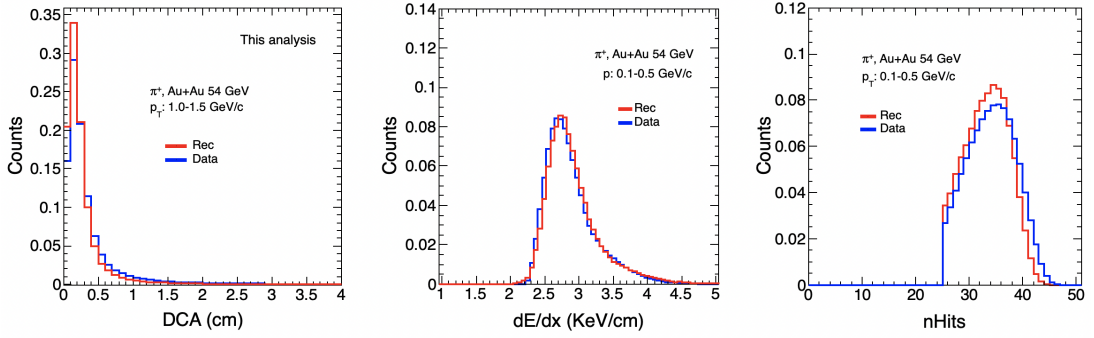


Figure 3.6: We compare the DCA, nHits, and nHitsdEdx distributions between reconstructed embedding tracks and real tracks, focusing on the π^+ embedding sample in Au+Au collisions at $\sqrt{s_{\text{NN}}} = 54.4$ GeV. The errors considered are purely statistical.

given a value of rapidity and p_T by sampling a uniform distribution over some range of interest. A reconstructed track is a track that has been successfully reconstructed by the reconstruction software. A matched track is a reconstructed track that is also matched back to an originally embedded track. This last distinction is necessary since embedded tracks are embedded into events with real tracks. In the following discussions and plots, we only utilize matched tracks which have also passed all of the track quality cuts defined earlier in table 3.2.

We compare DCA, nHits, and dE/dx distributions between real data and embedding for π^+ . These comparisons are shown in Fig. 3.6, referencing the π^+ embedding sample. The plots illustrate a good agreement between the embedding and real data in Au+Au collisions at $\sqrt{s_{\text{NN}}} = 54.4$ GeV.

3.3.1 Track Energy-Loss Correction

As a particle traverses the detector material, it undergoes interactions and experiences multiple Coulomb scatterings along its trajectory. Consequently, the particle undergoes energy loss, leading to changes in its momentum. This energy loss is momentum-dependent, with lower momentum particles losing more energy compared to higher momentum particles [113]. TPC measures a momentum lower than the actual momentum of the particle at freeze-out due to this effect. To correct for Coulomb scattering and energy loss, the track reconstruction algorithm assumes a pion mass for each particle. However, heavier particles such as K^\pm and $p(\bar{p})$ require additional momentum corrections. These corrections are calculated using embedding. The energy loss correction factor is determined by analyzing the momentum difference between reconstructed (p_T^{REC}) and initial (p_T^{MC}) momentum as a function of p_T^{REC} .

The correction factor is determined by fitting the energy loss versus p_T^{REC} distributions

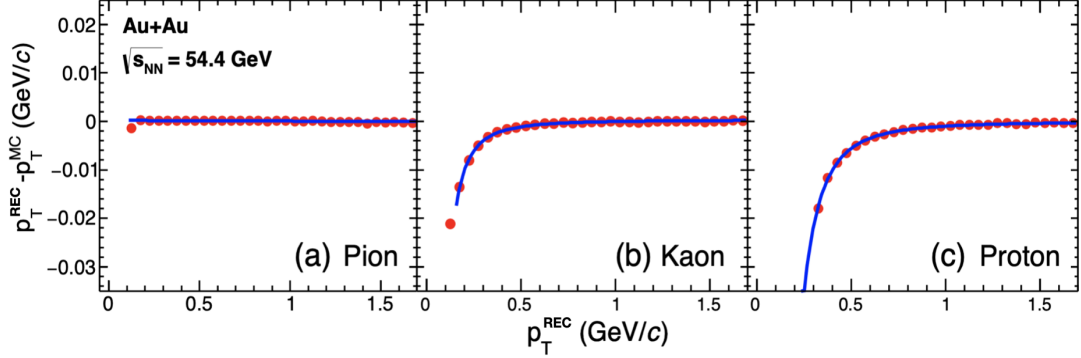


Figure 3.7: The difference between the reconstructed momentum (p_T^{REC}) and the Monte Carlo generated momentum (p_T^{MC}) is plotted as a function of p_T^{REC} for pions (left panel), kaons (middle panel), and protons (right panel) in Au+Au collisions at $\sqrt{s_{\text{NN}}} = 54.4$ GeV. These plots show the statistical errors only.

using the following functional form:

$$p_T^{\text{REC}} - p_T^{\text{MC}} = p_0 + p_1 \left(1 + \frac{p_2}{(p_T)^2} \right)^{p_3}, \quad (3.1)$$

where p_0 , p_1 , p_2 , and p_3 are the fit parameters. Since the energy loss correction depends on the particle type only, a uniform energy loss correction is applied across all centralities. Figure 3.7 illustrates this correction for pions, kaons, and protons in Au+Au collisions at $\sqrt{s_{\text{NN}}} = 54.4$ GeV.

3.3.2 TPC Tracking Efficiency

After applying the energy-loss correction, It is important to correct the raw spectra of these particles for the track reconstruction efficiency ($\varepsilon_{\text{track-eff}}$), which can be obtained from the embedding method discussed previously. Track reconstruction efficiency depends on factors such as the rapidity and p_T of the particle track. Tracks may go unmeasured due to trajectory issues within the TPC or potential detector malfunction or failure of track reconstruction algorithm. The product of efficiency and acceptance, termed tracking efficiency, quantifies the likelihood of a particle being reconstructed as a track. Determining tracking efficiency is crucial for each particle species, centrality class, and rapidity bin, considering p_T .

The tracking efficiency multiplied by acceptance is the ratio of the distribution of reconstructed to original Monte Carlo tracks as a function of p_T within the specified rapidity range. It is defined as:

$$\varepsilon_{\text{track-eff}} = \frac{\text{Number of matched MC tracks}}{\text{Number of input MC tracks}}. \quad (3.2)$$

Figure 3.8 illustrates the tracking efficiency for pions, kaons, and protons at mid-

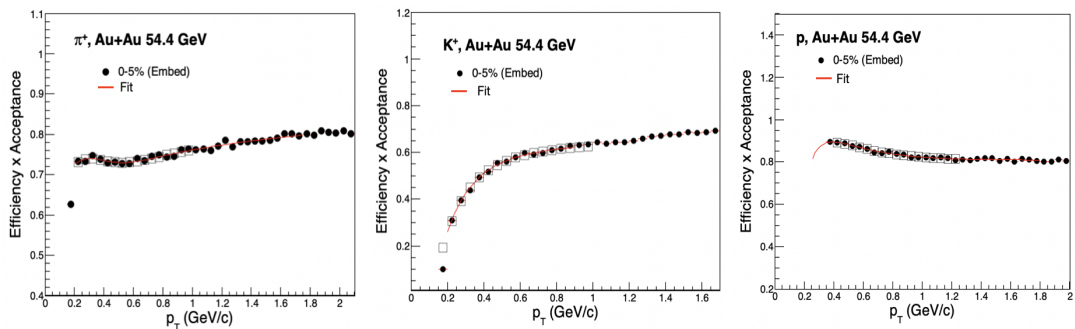


Figure 3.8: Track reconstruction efficiency and acceptance as a function of p_T^{MC} for reconstructed pions (left), kaons (middle), and protons (right) derived from embedding in Au+Au collisions at $\sqrt{s_{\text{NN}}} = 54.4$ GeV. The lines represent the functional fit to the data, with statistical errors being depicted.

rapidity in the most central (0-5%) events at $\sqrt{s_{\text{NN}}} = 54.4$ GeV. The presented TPC tracking efficiency is a fit in the full p_T range, expressed as:

$$f(p_T) = A \exp[-(B/p_T)^C],$$

where $f(p_T)$ is the function to fit tracking efficiency and A , B , and C are fit parameters. It is important to note that TPC tracking efficiency is presented as a function of embedded p_T since the correction is applied after the energy-loss correction. The energy-loss correction precedes the evaluation of the tracking efficiency correction, ensuring accuracy in the correction process.

3.3.3 Pion Feed-down Correction

The charged pions spectra undergo corrections due to contamination sources. As the lightest mesons, pions receive contributions from higher resonance particles such as K_S^0 and Λ , along with potential misidentification with muons. Background pions from the detector material further contribute. Monte Carlo simulations, based on HIJING and GEANT, correct for weak decay and muon contamination. The feed-down contribution, encompassing weak decays and muon contamination, is subtracted from the raw pions yield in each p_T bin. This correction, showing p_T dependence but no centrality dependence, is applied across all nine centrality classes.

Figure 3.9 illustrates the comprehensive contribution to the pions yield arising from feed-down processes, presenting as a function of p_T in Au+Au collisions at $\sqrt{s_{\text{NN}}} = 54.4$ GeV.

3.3.4 Proton Background Correction

When high-energy charged particles pass through the detector, they interact with the detector materials, which can produce secondary particles including protons. The DCA

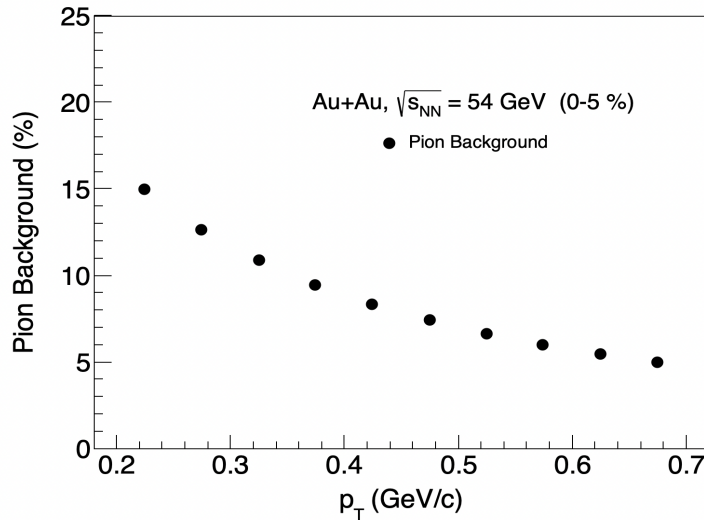


Figure 3.9: The total background fraction to the yield of pions as a function of p_T , illustrating contributions from weak decay and muon contamination in Au+Au collisions at $\sqrt{s_{\text{NN}}} = 54.4$ GeV. The errors are statistical only.

distributions play a crucial role in correcting for proton background. Since these protons originate from the detector material, they are produced at a significant distance from the primary collision vertex. Referred to as knock-out protons, they exhibit a prolonged trail in the DCA distribution for protons. In contrast, anti-protons do not result from such interactions, resulting in the absence of a long tail in the DCA distribution for anti-protons. The effect is dependent on p_T , being most pronounced at low p_T and significantly reduced at high p_T . To correct the proton yield for these background protons, a correlation between the DCA distributions of protons and anti-protons is established in real data, as discussed in the references [100]. Protons and antiprotons are specifically chosen with a dE/dx cut of $|n\sigma_p| < 2$, where σ_p represents the dE/dx resolution of the TPC for protons. In Figures 3.10 and 3.11, the black circles depict the DCA distribution of protons, with the red-solid line representing the fit to this distribution. The blue-dotted line corresponds to the $\bar{p}(DCA)$ distribution, scaled by the \bar{p}/p ratio. It is evident that the DCA distribution of protons primarily arises from knock-out protons originating from the detector material and can be effectively described by the following function:

$$p_{\text{bgd}}(DCA) \propto [1 - \exp(-DCA/DCA_0)]^\alpha$$

Here, DCA_0 and α are fit parameters. Assuming the background-subtracted proton DCA distribution exhibits a similar shape to that of the antiproton distribution, the DCA distribution of protons can be fitted using the following equation:

$$p(DCA) = \frac{\bar{p}(DCA)}{r_{\bar{p}/p}} + A p_{\text{bgd}}(DCA)$$

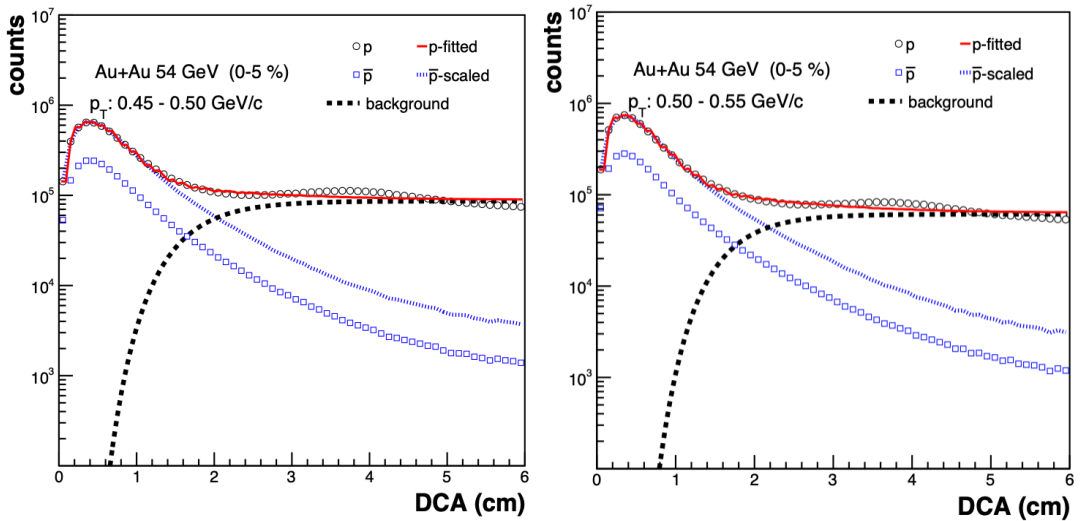


Figure 3.10: The DCA distributions of protons and antiprotons for $0.45 < p_T$ (GeV/c) < 0.50 and $0.50 < p_T$ (GeV/c) < 0.55 in the 0–5% centrality range in Au+Au collisions at $\sqrt{s_{NN}} = 54.4$ GeV. The dashed curve represents the fit to the proton background, the dotted histogram depicts the antiproton DCA distribution scaled by $r_{\bar{p}/p}$, and the solid histogram shows the fit to the proton DCA distribution. The errors are statistical only.

Where $r_{\bar{p}/p}$ and A are fit parameters. Utilizing the functional fit to the proton DCA distribution, we calculate the proton background fraction in different p_T bins across nine distinct centrality classes. The proton background fraction decreases with an increase in p_T and exhibits an increase from central to peripheral collisions, as depicted in Fig. 3.12.

3.4 Systematic Uncertainties

In this section, we discuss the different systematic sources of uncertainty that come up when extracting observables like particle spectra, particle yields, average transverse momentum, and kinetic freeze-out parameters. Systematic uncertainties in the measurements arise from event and track selection cuts, the PID procedure, the methods for estimating correction factors, and errors associated with extrapolation using functional fits. To calculate the impact of systematic uncertainties on particle spectra, the data are analyzed with variations in event and track cuts across different ranges, as detailed in Table 3.3. The errors from these sources are calculated and then added in quadrature.

The determination of integrated particle yields (dN/dy) and $\langle p_T \rangle$ involves using fitting functions to extrapolate the p_T spectra into the unmeasured low- p_T and high- p_T regions. The principal source of systematic uncertainty in dN/dy and $\langle p_T \rangle$ arises from this extrapolation. To assess this systematic error, various fit functions are utilized. For pions, the Levy-Tsallis function is used to calculate dN/dy for the default value, while the p_T -exponential function is used for systematic error estimation. For kaons, the Levy-Tsallis function calculates dN/dy for the default value, with the Boltzmann function used for

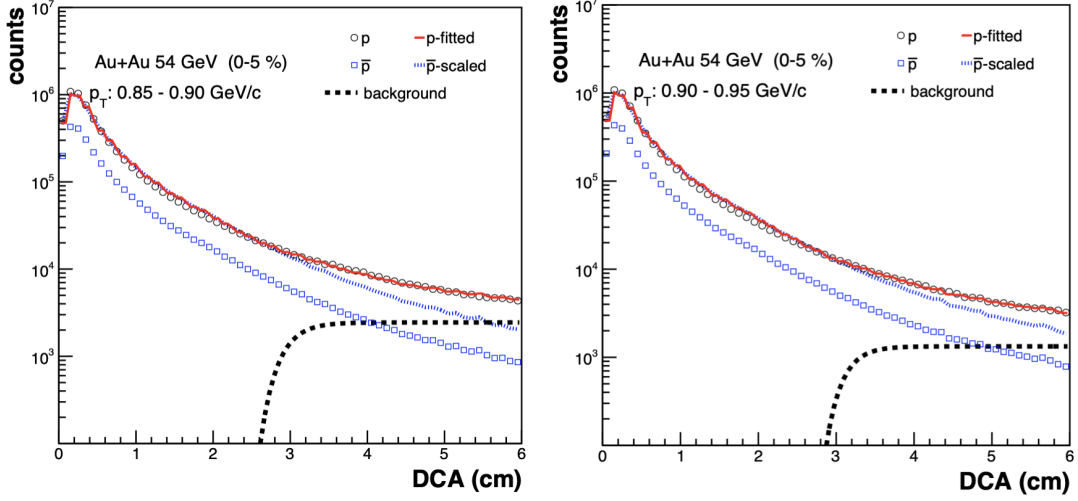


Figure 3.11: The DCA distributions of protons and antiprotons for $0.85 < p_T$ (GeV/c) < 0.90 and $0.90 < p_T$ (GeV/c) < 0.95 in the 0–5% centrality range in Au+Au collisions at $\sqrt{s_{NN}} = 54.4$ GeV. The dashed curve represents the fit to the proton background, the dotted histogram depicts the antiproton DCA distribution scaled by $r_{\bar{p}}/p$, and the solid histogram shows the fit to the proton DCA distribution. The errors are statistical only.

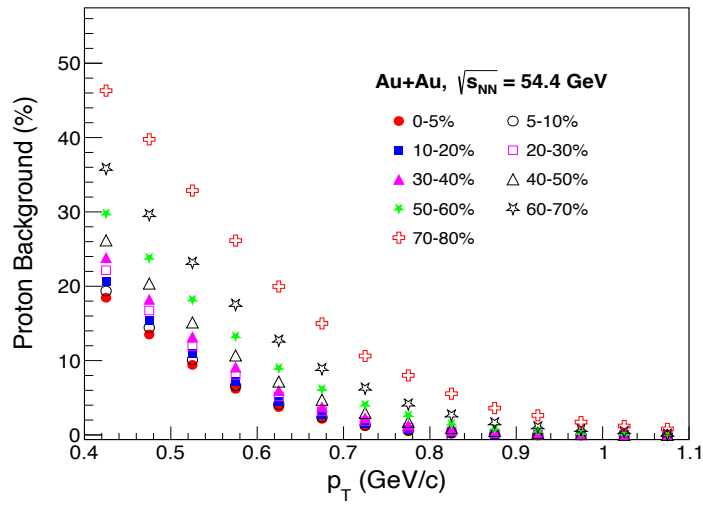


Figure 3.12: The total background fraction to the yield of proton as a function of p_T , for different centralities in Au+Au collisions at $\sqrt{s_{NN}} = 54.4$ GeV. The errors are statistical only.

Cut	Default Value	Modified Value
Vz (cm)	< 30	< 50
y	< 0.1	< 0.5
DCA (cm)	< 3	< 2
nHitsFit	≥ 25	≥ 20
ndEdx	≥ 15	≥ 10
p_T (GeV/c)	> 0.10	> 0.15

Table 3.3: Default and modified values of event and track cuts to measure systematic uncertainties.

systematic error estimation. In the case of protons, the Double exponential function is used for the default value, and the m_T -exponential function is used for systematic error estimation. Here, $m_T = \sqrt{m^2 + p_T^2}$ denotes the transverse mass of the particle. The functional forms of these fit functions are as follows:

- Levy function: $\propto \frac{(n-1)(n-2)}{nT[nT+m(n-2)]} \times \frac{dN}{dy} \times p_T \times \left(1 + \frac{m_T-m}{nT}\right)^{-n}$
- p_T -exponential: $\propto e^{-p_T/T}$
- m_T -exponential: $\propto e^{-(m_T-m)/T}$
- Boltzmann: $\propto m_T e^{-m_T/T}$
- Double-exponential: $\propto A_1 \exp^{-p_T^2/T_1^2} + A_2 \exp^{-p_T^2/T_2^2}$

Where m_T represents the transverse mass of the particle under study, T denotes the temperature obtained from their respective fit functions. Parameters A_1 , A_2 , T_1 , and T_2 , T , and n are free parameters and determined through fitting.

Other sources of systematic uncertainties must also be considered. An uncertainty due to tracking efficiency, around 5%, is added in quadrature. Systematic uncertainties from pion feed-down and proton background corrections are also included. Proton background is significant at low p_T but negligible at higher p_T . The systematic uncertainty from pion feed-down correction is negligible. We combined the systematic and statistical errors in quadrature to obtain the final error in the data.

Systematic errors in particle yields are used to calculate the errors in the particle ratios. However, the correlated error contributions from tracking efficiency tend to cancel out. Additionally, the contributions from extrapolation largely cancel out when calculating particle ratios. The errors in the average momentum ($\langle p_T \rangle$) calculation mostly arise from the extrapolated region. These systematic errors come from changing the range of the fitting and altering the fit functions. The systematic errors are estimated to be around 9-10% for π^\pm , 8-10% for K^\pm , and 9-11% for $p(\bar{p})$.

3.5 Results and Discussions

In this part, we present the p_T -spectra of π^\pm , K^\pm , p , and \bar{p} , in Au+Au collisions at $\sqrt{s_{\text{NN}}} = 54.4$ GeV. We present the bulk properties such as dN/dy , $\langle p_T \rangle$, particle ratios, and freeze-out parameters. The results obtained in Au+Au collisions at $\sqrt{s_{\text{NN}}} = 54.4$ GeV are compared with previously published results from RHIC energies, and their physics implications are also discussed.

3.5.1 Transverse Momentum Spectra

The p_T -spectra of a particle comprise all of the hidden information about its formation and transverse dynamics as it travels from creation in a heavy-ion collision. The shape of the p_T spectra and its dependence on particle type and centrality reflects collision dynamics. In heavy-ion collisions, high particle density leads to frequent collisions, making particles behave like a fluid. Pressure from the collision pushes particles outward, creating an expanding, potentially thermalized source. This expansion, driven by internal pressure gradients, introduces a blast velocity. This blast velocity and the thermal freeze-out temperature shape the p_T spectra and indicate strong radial flow [114].

The p_T spectra of identified particles provide information on the combined effects of kinetic freeze-out temperature (T_{kin}) and the collective expansion of the fireball (radial flow) in the system through a simultaneous fit. The collective flow moves particles to higher p_T regions, while low- p_T spectra reflect late-stage collision dynamics, including soft collective effects and resonances. High p_T spectra are influenced by early-stage parton dynamics. The results presented focus on the low p_T region. After applying the necessary corrections, the invariant yields of π^\pm , K^\pm , and $p(\bar{p})$ are given by the following mathematical expression:

$$\frac{1}{N_{\text{events}}} \frac{d^2N}{2\pi p_T dp_T dy} = \frac{1}{2\pi p_T} \times \frac{1}{N_{\text{events}}} \times \frac{1}{\Delta p_T \Delta y} \times \frac{1}{C(p_T)} \times Y(p_T), \quad (3.3)$$

where $Y(p_T)$ and $C(p_T)$ represent raw yield and corrections to the raw yield, respectively. Finally the p_T spectra for various particles, including π^+ , π^- , K^+ , K^- , p , and \bar{p} in Au+Au collisions at $\sqrt{s_{\text{NN}}} = 54.4$ GeV, are presented in Fig. 3.13 using TPC. These spectra are shown for nine centrality classes: 0-5%, 5-10%, 10-20%, 20-30%, 30-40%, 40-50%, 50-60%, 60-70%, and 70-80%. For clarity, the spectra are scaled with different factors, as shown in the plot. To calculate derived physical quantities, we have combined the TPC data points with TOF data taken from another analysis. The combined spectra are shown in Fig. 3.14. Fits are applied using specific functions (Levy for pions and kaons, and double exponential for (anti)protons) to extract dN/dy and the $\langle p_T \rangle$ in each centrality.

The figure shows a clear p_T and centrality dependence. Pion spectra exhibit similar

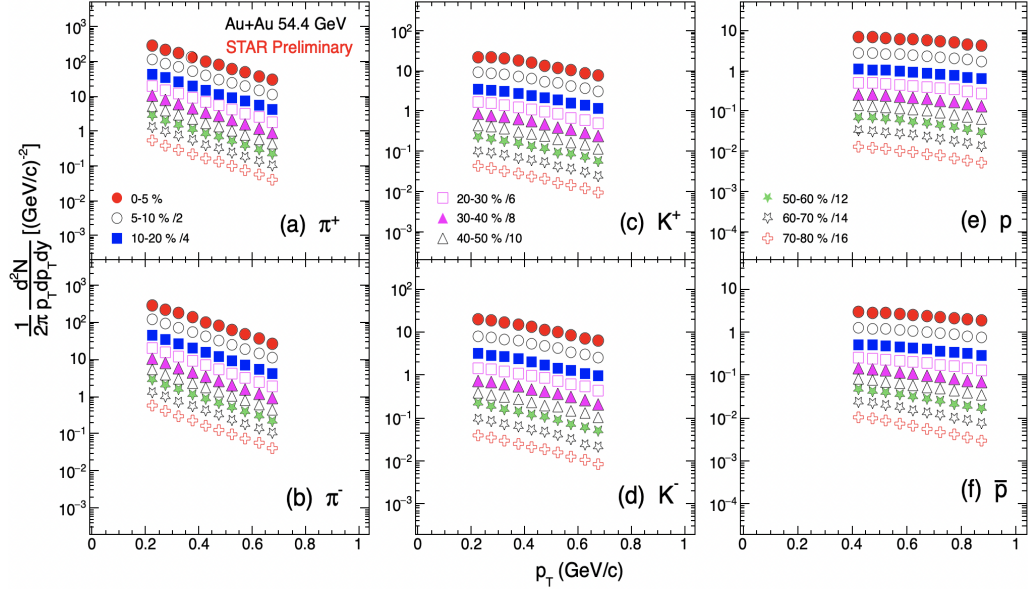


Figure 3.13: p_T spectra of π^\pm , K^\pm , and $p(\bar{p})$ measured at mid-rapidity ($|y| < 0.1$) in Au+Au collisions at $\sqrt{s_{NN}} = 54.4$ GeV in STAR using TPC. Spectra are plotted for nine centrality classes, with some scaled for clarity. Uncertainties represent total systematic and statistical uncertainties added in quadrature, primarily dominated by systematic errors.

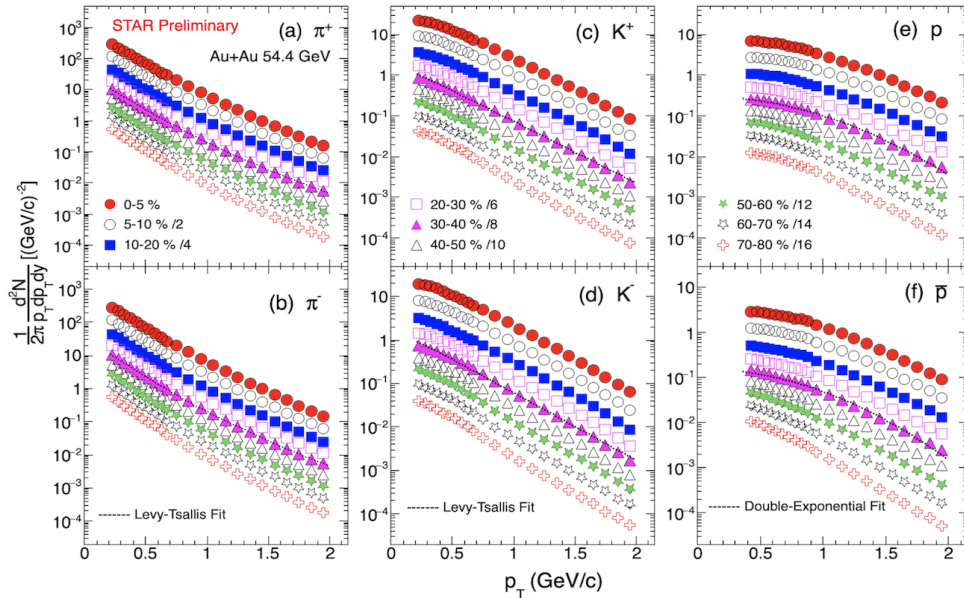


Figure 3.14: p_T spectra of π^\pm , K^\pm , and $p(\bar{p})$ measured at mid-rapidity ($|y| < 0.1$) in Au+Au collisions at $\sqrt{s_{NN}} = 54.4$ GeV in STAR using TPC and TOF. Spectra are plotted for nine centrality classes, with some scaled for clarity. Fits to the p_T spectra are shown for 30-40% centrality using a Levy function for pions and kaons and a double exponential for (anti)protons. Uncertainties represent total systematic and statistical uncertainties added in quadrature, primarily dominated by systematic errors.

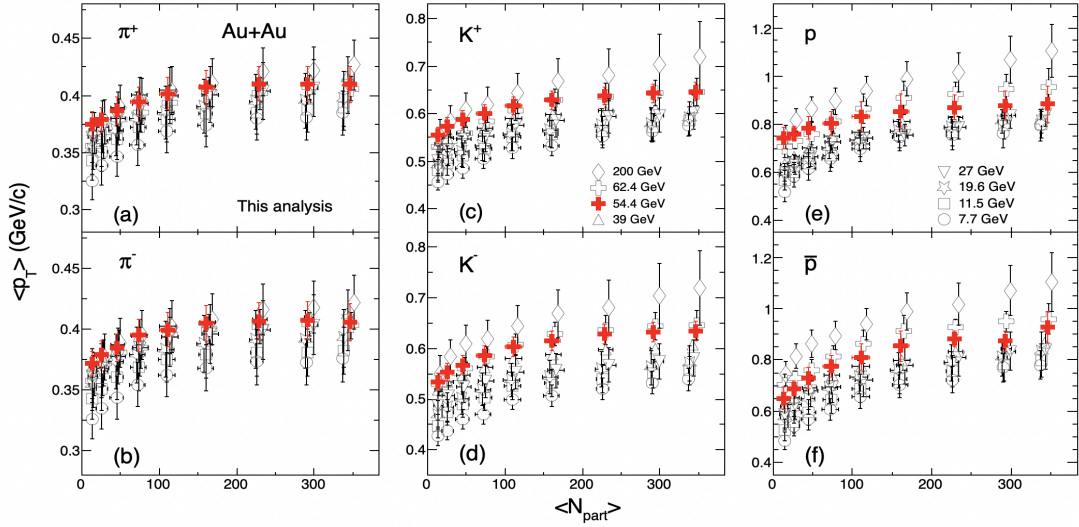


Figure 3.15: The average transverse momentum ($\langle p_T \rangle$) distributions of π^+ , π^- , K^+ , K^- , p , and \bar{p} as a function of the number of participants ($\langle N_{\text{part}} \rangle$) for Au+Au collisions at $\sqrt{s_{\text{NN}}} = 54.4$ GeV are examined. These findings are combined with those from Au+Au collisions at various beam energies reported by STAR [108, 113, 115]. The uncertainties encompass total systematic and statistical uncertainties added in quadrature.

shapes across centrality classes, displaying a faster fall with increasing p_T due to substantial contributions from resonance decay at low- p_T . For kaons and (anti)protons, the spectra gradually flatten as centrality increases. The proton spectra exhibit a more concave nature from peripheral to central collisions, indicating progressively stronger radial flow effects in central collisions with higher particle production.

3.5.2 Average Transverse Momentum ($\langle p_T \rangle$)

We can study the changes in the measured spectral shapes of different particles by using the variable $\langle p_T \rangle$, taking into account both energy and centrality. This measure offers insights into the behavior of different types of particles in the transverse direction. The calculation for $\langle p_T \rangle$ is done using the following formula:

$$\langle p_T \rangle = \frac{\int_0^\infty p_T 2\pi p_T f(p_T) dp_T}{\int_0^\infty 2\pi p_T f(p_T) dp_T},$$

The $\langle p_T \rangle$ values for π^\pm , K^\pm , p , and \bar{p} are determined at mid-rapidity ($|y| < 0.1$) from the measured p_T spectra up to $p_T = 2$ GeV/c. These values are then extrapolated to the unmeasured region up to $p_T = 10$ GeV/c using different fitting functions. The variable $\langle p_T \rangle$ characterizing changes in spectral shapes. Systematic uncertainties on $\langle p_T \rangle$ depend on the fit function used for spectra extrapolation. These uncertainties are estimated using different functional forms for the extrapolation of the p_T -spectra.

Figure 3.15 displays mid-rapidity $\langle p_T \rangle$ for π^+ , π^- , K^+ , K^- , p , and \bar{p} as a function

of N_{part} in Au+Au collisions at $\sqrt{s_{NN}} = 54.4$ GeV, compared with other RHIC energies [108, 113, 115]. The figure shows that $\langle p_T \rangle$ for π^\pm , K^\pm , and $p(\bar{p})$ increases with higher $\langle N_{\text{part}} \rangle$ or centrality. This means that radial flow effects get stronger from peripheral to central collisions. $\langle p_T \rangle$ and radial flow also increase from pions to kaons and from kaons to protons. This matches the observations from the p_T spectra, where heavier particles are more affected by collective flow. The $\langle p_T \rangle$ in Au+Au collisions at $\sqrt{s_{NN}} = 54.4$ GeV follows the trend observed with other BES energies.

3.5.3 Particle Yields (dN/dy)

The total number of particles tells about the overall entropy produced in a heavy-ion collision. The p_T -spectra reveals the transverse dynamics, while the dN/dy versus y shows the longitudinal dynamics. The total integrated particle yield at mid-rapidity, obtained by integrating the invariant yield over p_T , is given by:

$$\frac{dN}{dy} = \int f(p_T) 2\pi p_T dp_T$$

The values of dN/dy for π^\pm , K^\pm , p , and \bar{p} are determined at mid-rapidity ($|y| < 0.1$) from the measured p_T spectra up to $p_T = 2$ GeV/c. They are then extrapolated to the unmeasured region up to $p_T = 10$ GeV/c using different fitting functions. Pions and kaons are fitted with the Levy function and protons/antiprotons with a double exponential function. Systematic uncertainties on these extrapolated yields are estimated by comparing results from different fit functions. These functions are discussed earlier.

Figure 3.16 shows the measured dN/dy for π^+ , π^- , K^+ , K^- , p , and \bar{p} , normalized by $\langle N_{\text{part}} \rangle / 2$, as a function of $\langle N_{\text{part}} \rangle$ in Au+Au collisions at $\sqrt{s_{NN}} = 54.4$ GeV. These yields are compared with published results from Au+Au collisions at $\sqrt{s_{NN}} = 7.7, 19.6, 27, 39, 62.4,$ and 200 GeV, measured by the STAR detector at RHIC [108, 113, 115].

The dependence on collision centrality at $\sqrt{s_{NN}} = 54.4$ GeV is comparable to that observed at BES-I energies. The normalized yields for π^\pm , K^\pm , and p increase from peripheral to central collisions. However, \bar{p} shows a weak centrality dependence. The rise in proton yields per participating nucleon with increasing collision centrality is attributed to significant baryon stopping at most central collisions. The particle yields determined at mid-rapidity demonstrate sensitivity to the initial energy density. This observation provides valuable insights into the intricate interplay between particle production mechanisms and the evolving conditions of the collision system.

Figure 3.17 presents $(dN/dy)/(\langle N_{\text{part}} \rangle / 2)$, as a function of $\sqrt{s_{NN}}$ for π^\pm , K^\pm , p , and \bar{p} in Au+Au collisions with 0–5% centrality at $\sqrt{s_{NN}} = 54.4$ GeV. The plot includes data from other BES-I energies and published results from the Alternating Gradient Synchrotron (AGS) [116–123], Super Proton Synchrotron (SPS) [124–127], and RHIC

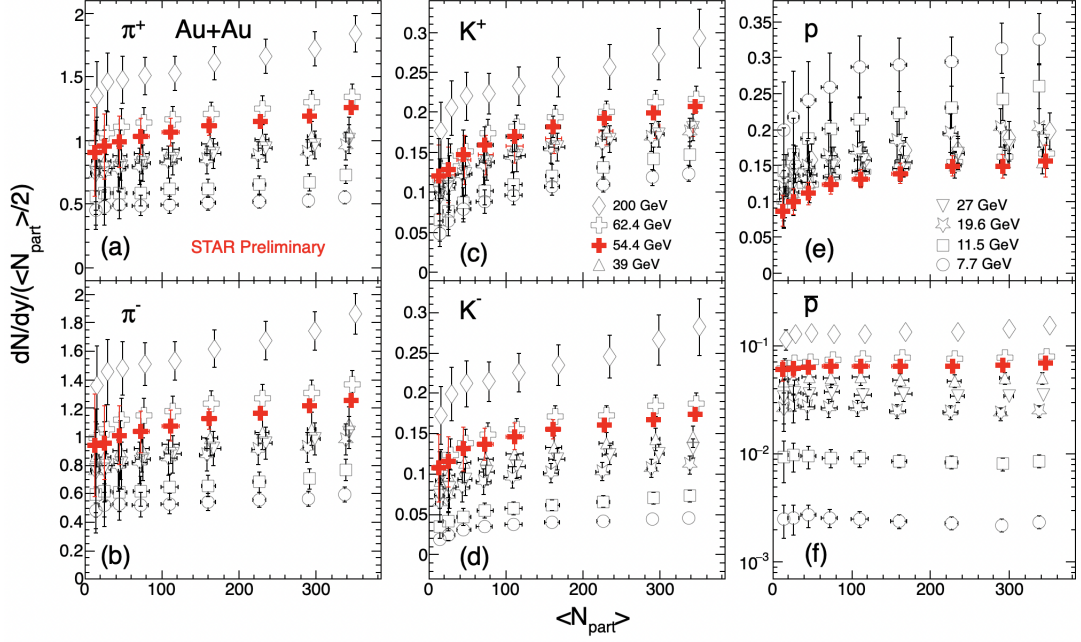


Figure 3.16: dN/dy of π^+ , π^- , K^+ , K^- , p , and \bar{p} scaled by $0.5 \times \langle N_{\text{part}} \rangle$ as a function of $\langle N_{\text{part}} \rangle$ for Au+Au collisions at $\sqrt{s_{\text{NN}}} = 54.4$ GeV. The results are compared with Au+Au collisions at $\sqrt{s_{\text{NN}}} = 200$ GeV, along with dN/dy values at various other beam energies from STAR [108, 113, 115]. The uncertainties represent total systematic and statistical uncertainties added in quadrature.

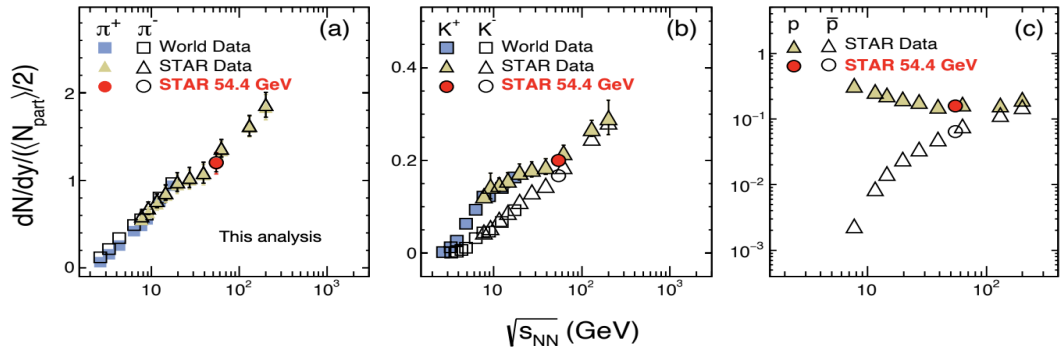


Figure 3.17: The scaled yields, dN/dy , of π^+ , π^- , K^+ , K^- , p , and \bar{p} , normalized by $\langle N_{\text{part}} \rangle / 2$ are presented as a function of $\sqrt{s_{\text{NN}}}$ for Au+Au collisions at $\sqrt{s_{\text{NN}}} = 54.4$ GeV. These results are compared with data from AGS, SPS, and RHIC at various collision energies. The statistical and systematic uncertainties have been combined in quadrature [108, 113, 115].

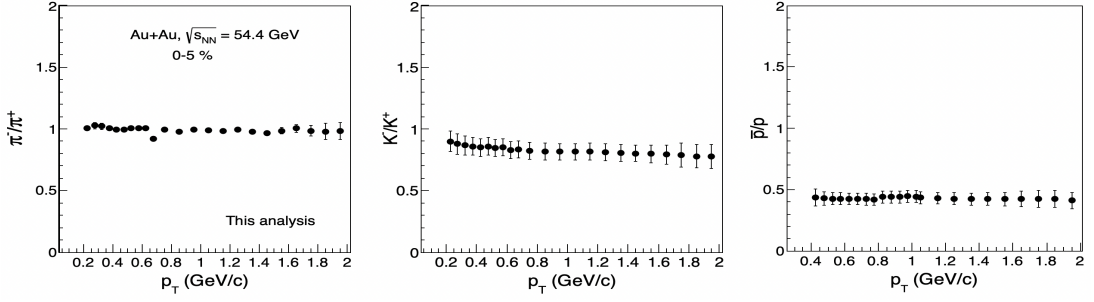


Figure 3.18: Ratios of π^-/π^+ , K^-/K^+ , and \bar{p}/p as a function of p_T in 0-5% central Au+Au collisions at $\sqrt{s_{NN}} = 54.4$ GeV, measured by the STAR detector at RHIC.

[128–130] experiments. Observations show an increasing trend in the yields of charged pions, kaons, and antiprotons with increasing collision energy. In contrast, proton yields exhibit a decreasing trend as the collision energy rises due to more baryon stopping at lower energies. The pion yields show a linear increase with collision energy but exhibit a kink around 19.6 GeV, suggesting a possible shift in the particle production mechanism at this energy. The kaon yields display an interesting pattern, with K^+ and K^- production differing significantly between AGS and BES energies. K^+ production is influenced by both associated and pair production, with associated production dominating at lower energies and pair production at higher energies, while K^- production is primarily driven by pair production. Proton yields increase at lower energies due to baryon stopping, with higher yields at 7.7 GeV compared to 200 GeV. At top RHIC energies, proton and antiproton yields are comparable due to pair production, and antiproton yields generally rise with energy. The outcome at $\sqrt{s_{NN}} = 54.4$ GeV aligns with the broader energy dependence trends observed at AGS, SPS, RHIC, and LHC energies.

This analysis helps us understand how particle production changes with energy in different collision systems, showing the complex processes that control how different particles are produced in heavy-ion collisions.

3.5.4 Particle Ratios

Particle ratios can be used to investigate the bulk properties of the system, including baryon content, strangeness production, and the Coulomb potential of the charged source. These ratios are calculated based on different integrated yields, collectively providing information on the chemical freeze-out conditions. The ratios of π^-/π^+ , K^-/K^+ , \bar{p}/p , K^+/π^+ , K^-/π^- , and \bar{p}/π^+ measured as functions of p_T , centrality, and energy at $\sqrt{s_{NN}} = 54.4$ GeV in Au+Au collisions are presented here. The error bars represent statistical and systematic errors added in quadrature. The results are compared with other RHIC energies [108, 113, 115].

Figure 3.18 shows the π^-/π^+ , K^-/K^+ , and \bar{p}/p ratios as functions of p_T in Au+Au

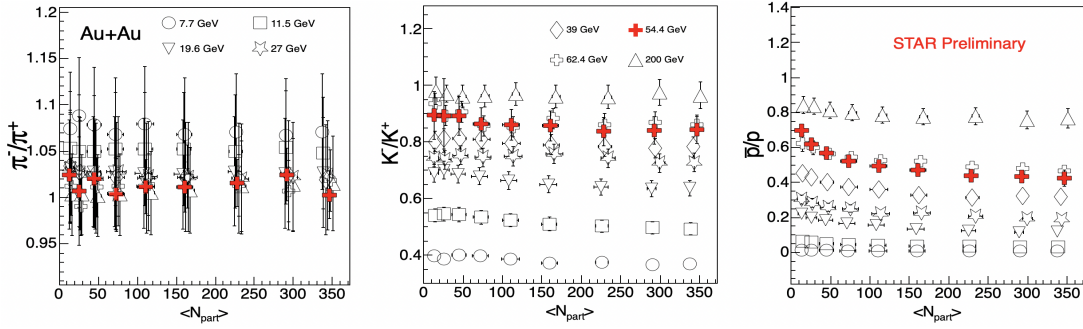


Figure 3.19: Ratios of π^-/π^+ , K^-/K^+ , and \bar{p}/p as a function of $\langle N_{\text{part}} \rangle$ in Au+Au collisions at $\sqrt{s_{\text{NN}}} = 54.4$ GeV. The results are compared with Au+Au collisions at $\sqrt{s_{\text{NN}}} = 200$ GeV, along with corresponding values for various other beam energies from STAR. The uncertainties represent total systematic and statistical uncertainties added in quadrature.

collisions at $\sqrt{s_{\text{NN}}} = 54.4$ GeV for most central events. Remarkably, the anti-particle-to-particle ratios show minimal p_T dependence. This observation suggests that particles and their anti-particles undergo freeze-out simultaneously and share similar radial flow dynamics.

Figure 3.19 shows the centrality dependence of π^-/π^+ , K^-/K^+ , and \bar{p}/p in Au+Au collisions at $\sqrt{s_{\text{NN}}} = 54.4$ GeV, with comparisons to other RHIC energies. Both statistical and systematic errors are combined for particle ratios.

The π^-/π^+ ratio shows weak dependence on centrality, suggesting a consistent pion production mechanism across peripheral to central collisions. The flat K^-/K^+ ratio shows uniform production mechanisms across centrality and indicates similar collective flow for K^- and K^+ , aligning with observations at lower energies. The \bar{p}/p ratio is lower in central collisions compared to peripheral. This indicates that more protons and antiprotons are annihilated in central collisions. In central collisions, where a larger volume of hot, dense nuclear matter is created, the minor variation in the \bar{p}/p ratio with centrality might suggest that antiprotons are being absorbed within this extensive collision area. Another possible reason for this centrality dependence could be the increased stopping of baryons in the central region.

Figure 3.20 shows different particle ratios such as K^+/π^+ , K^-/π^- , p/π^+ , and \bar{p}/π^- for Au+Au collisions at $\sqrt{s_{\text{NN}}} = 54.4$ GeV. For comparison, results from the STAR experiment at other beam energies are also included. Both K^+/π^+ and K^-/π^- ratios increase from peripheral to mid-central collisions and then remain almost constant with $\langle N_{\text{part}} \rangle$. This trend is related to strangeness equilibrium, as described by various thermodynamical models [131, 132]. These models explain this behavior as the system size changes from peripheral to central collisions, transitioning from a canonical to a grand-canonical description. This ratio is also influenced by baryon stopping at mid-rapidity. The general behavior with energy is consistent with the results in Au+Au collisions at $\sqrt{s_{\text{NN}}} = 54.4$ GeV.

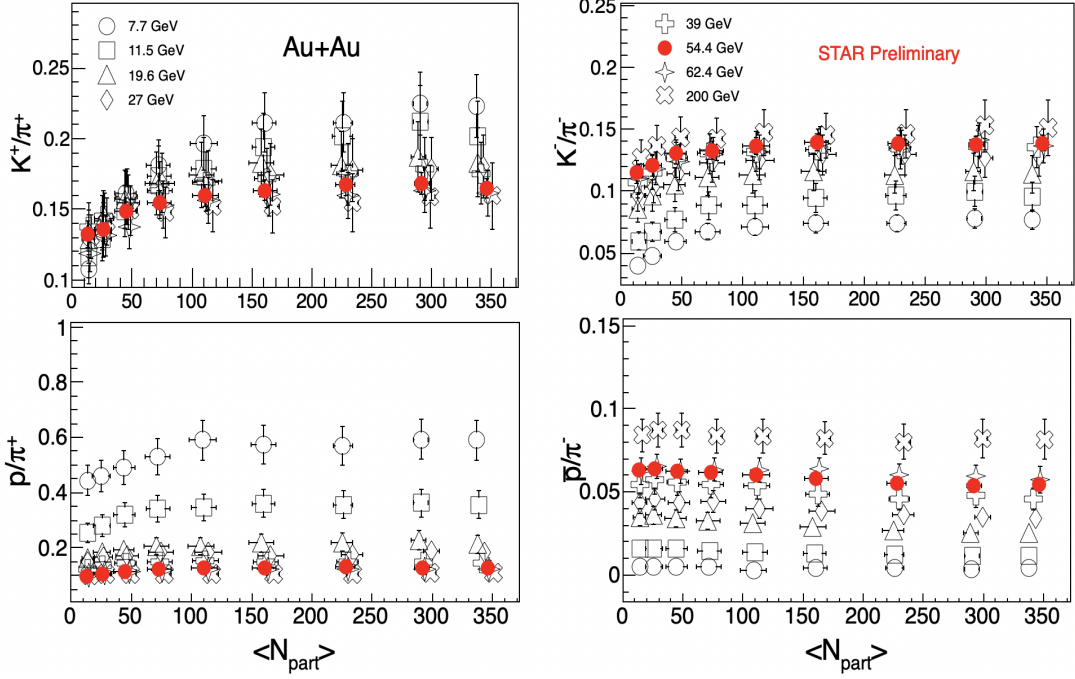


Figure 3.20: Ratios of K^+/π^+ , K^-/π^- , p/π^+ , and \bar{p}/π^- as a function of $\langle N_{\text{part}} \rangle$ in Au+Au collisions at $\sqrt{s_{\text{NN}}} = 54.4$ GeV. The results are compared with Au+Au collisions at $\sqrt{s_{\text{NN}}} = 200$ GeV, along with corresponding values for various other beam energies from STAR. The uncertainties represent total systematic and statistical uncertainties added in quadrature.

The \bar{p}/π^- ratio characterizes antibaryon production relative to total particle multiplicity, showing independence from the number of participants. At higher RHIC energies, the \bar{p}/π^- ratio remains unaffected by net-baryon density, while at low energies, stronger effects from baryon stopping and net-baryon density are evident. \bar{p}/π^- ratio in Au+Au collisions at $\sqrt{s_{\text{NN}}} = 54.4$ GeV follows similar trends as previously published results from STAR.

Baryons originate from both pair production and transport from initial colliding nuclei at beam rapidities. Understanding baryon transport sheds light on the early evolution of heavy-ion collisions. The p/π^+ ratios consistently increase with centrality at lower RHIC energies but remain constant at mid to higher energies (27–200 GeV), as illustrated in Fig. 3.20. The p/π^+ ratio in Au+Au collisions at $\sqrt{s_{\text{NN}}} = 54.4$ GeV follows a similar trend as observed at the higher RHIC energies of 62.4 and 200 GeV.

Figure 3.21 illustrates various integrated particle ratios in Au+Au collisions at $\sqrt{s_{\text{NN}}} = 54.4$ GeV, presenting π^-/π^+ , K^-/K^+ , and \bar{p}/p ratios as functions of $\sqrt{s_{\text{NN}}}$. The comparisons include AGS, SPS, STAR, and ALICE energies.

The π^-/π^+ ratio, initially higher than unity at lower energies, tends to approach unity at higher beam energies. This behavior suggests an increasing dominance of pair production over resonance decays.

The K^-/K^+ ratio gradually increases with collision energy and approaches unity. This

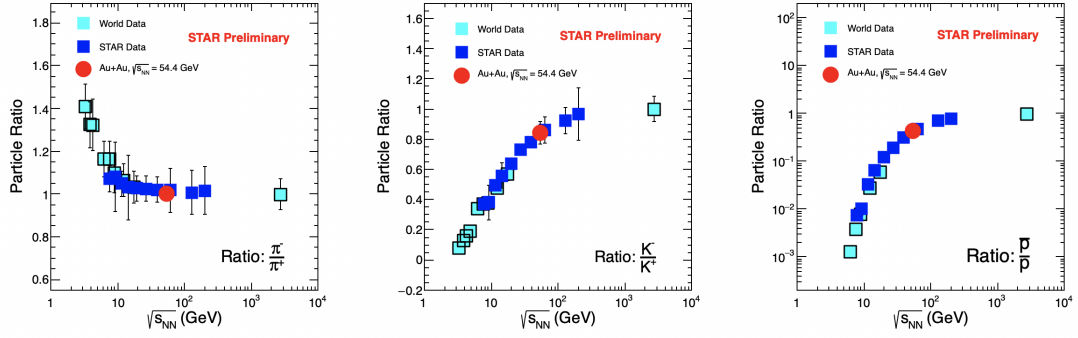


Figure 3.21: Ratios of π^-/π^+ , K^-/K^+ , and \bar{p}/p at midrapidity ($|y| < 0.1$) in central 0–5% Au+Au collisions at $\sqrt{s_{NN}} = 54.4$ GeV, compared to previous results from AGS [133–139], SPS [140–143], RHIC [113, 144], and LHC [145]. AGS results correspond to 0–5%, SPS to 0–7%, top RHIC to 0–5% (62.4 and 200 GeV) and 0–6% (130 GeV), and LHC to 0–5% central collisions. Errors shown are the quadrature sum of statistical and systematic uncertainties.

can be understood by considering the production mechanisms of K^+ and K^- , which result from a combination of pair production and associated production. In pair production, both K^+ and K^- are produced in equal numbers. However, in associated production, only K^+ is produced via reactions like $N + N \rightarrow N + X + K^+$ or $\pi + N \rightarrow X + K^+$, where N is a nucleon and X is a hyperon (e.g., Λ or Ξ). Thus, in heavy-ion collisions, K^+ is produced through both pair production and associated production, whereas K^- is mainly produced via pair production.

At lower energies, associated production dominates, resulting in more K^+ being produced. At higher beam energies, pair production becomes the dominant mechanism, producing equal numbers of K^+ and K^- . As the collision energy increases, the net baryon density decreases, leading to a reduction in K^+ production via associated production. Additionally, gluon-gluon fusion into strange quark-antiquark pairs increases the pair production rate with rising collision energy. These combined effects explain the behavior of the K^-/K^+ ratio as a function of collision energy.

The \bar{p}/p ratio increases with $\sqrt{s_{NN}}$, approaching unity at higher collision energies. This trend signifies a decrease in net baryon density as collision energy increases. It is important to mention that at low energies, the absorption of antiprotons in the baryon-rich environment is crucial.

3.5.5 Freeze-out Properties

In heavy-ion collisions, the initial stages involve a highly energetic interaction of colliding nuclei, creating a state of hot and dense matter known as the fireball. As the system expands and cools, different freeze-out stages govern the particle production process. Two key freeze-out stages are chemical freeze-out and kinetic freeze-out.

Chemical freeze-out occurs when inelastic collisions cease and the particle composition

is fixed. It is characterized by parameters such as the chemical freeze-out temperature (T_{ch}), baryon chemical potential (μ_{B}), and strangeness chemical potential (μ_{S}). These parameters reflect the freeze-out conditions and offer insights into the early stages of the collision system.

Kinetic freeze-out follows chemical freeze-out and marks the point at which particle interactions cease and particles cease to scatter. The blast-wave model [114], inspired by hydrodynamics, is employed to describe the kinetic freeze-out properties. By fitting p_T -spectra, this model yields information about the freeze-out temperature and collective flow of the produced particles.

In summary, the freeze-out properties in heavy-ion collisions, encompassing both chemical and kinetic freeze-out, provide essential information about the evolution of the colliding system, shedding light on the expansion dynamics of the fireball.

The invariant yields and p_T spectra of particles are useful tools for understanding the freeze-out properties of the system. The kinetic freeze-out parameters, which include the kinetic freeze-out temperature (T_{kin}) and radial flow velocity (β), are determined by fitting the measured particle p_T spectra in Au+Au collisions at $\sqrt{s_{\text{NN}}} = 54.4$ GeV using the blast-wave model [114]. These quantities provide insight into the transverse expansion of the system. In this study, we follow previously established methods to examine the kinetic freeze-out properties in Au+Au collisions at $\sqrt{s_{\text{NN}}} = 54.4$ GeV.

Assuming a radially boosted thermal source with a kinetic freeze-out temperature T_{kin} and a transverse radial flow velocity β , the p_T distribution of the particles is given by:

$$\frac{dN}{p_T dp_T} \propto \int_0^R r dr m_T I_0 \left(\frac{p_T \sinh \rho(r)}{T} \right) K_1 \left(\frac{m_T \cosh \rho(r)}{T_{\text{kin}}} \right), \quad (3.4)$$

where

$$m_T = \sqrt{p_T^2 + m^2} \quad (m = \text{mass of the hadron}),$$

$$\rho(r) = \tanh^{-1}(\beta).$$

I_0 and K_1 are modified Bessel functions of the first and second kind, respectively. $\beta = \beta_S \left(\frac{r}{R}\right)^n$, β represents the flow velocity, β_S is the surface velocity, $\frac{r}{R}$ is the relative radial position in the thermal source, and n is the exponent of the flow velocity profile. To obtain the average transverse radial flow velocity $\langle\beta\rangle$, the equation provided is $\langle\beta\rangle = \frac{2\beta_S}{2+n}$. In the context of heavy-ion collisions, π^\pm , K^\pm , p , and \bar{p} spectra are often fitted simultaneously with the blast-wave model.

Kinetic freeze-out parameters are simultaneously extracted through a blast-wave fit to π^\pm , K^\pm , and $p(\bar{p})$ spectra, as shown in Fig. 3.22 for Au+Au collisions at $\sqrt{s_{\text{NN}}} = 54.4$ GeV. The pion spectra are fitted above $p_T > 0.5$ GeV/ c due to the influence of resonance decays on the low p_T part. Additionally, the Blast-wave model is sensitive to

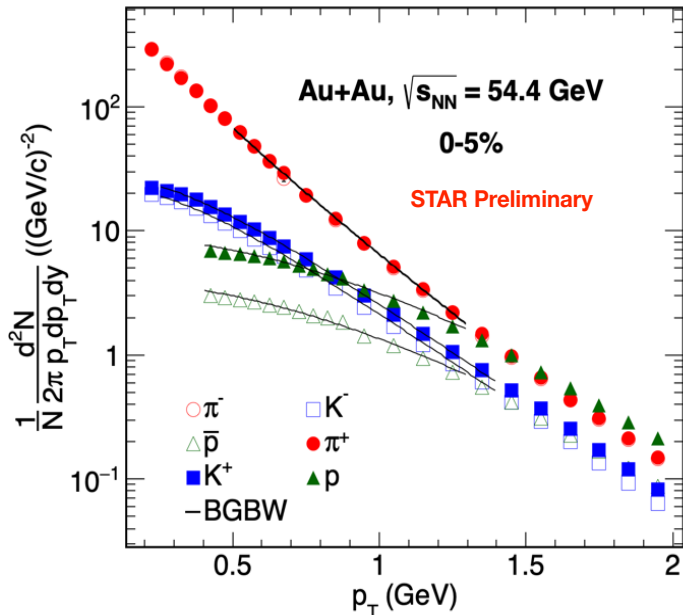


Figure 3.22: Simultaneous blast-wave fit to the p_T spectra of π^\pm , K^\pm , $p(\bar{p})$ in Au+Au collisions at $\sqrt{s_{\text{NN}}} = 54.4$ GeV in the 0–5% centrality class within $|y| < 0.1$. The uncertainties represent the total systematic and statistical uncertainties added in quadrature.

the p_T range of the spectra. The extracted Blast-wave parameters for Au+Au collisions at $\sqrt{s_{\text{NN}}} = 54.4$ GeV are within a similar p_T range as that for other BES-I energies $\sqrt{s_{\text{NN}}} = 7.7 - 39$ GeV i.e. p_T fit ranges for pions, is 0.5 to 1.3 GeV/c; for kaons, it spans 0.25 to 1.4 GeV/c; and for (anti)protons, the range is 0.4 to 1.3 GeV/c.

Figure 3.23 shows the anti-correlation between T_{kin} and $\langle\beta\rangle$, in Au+Au collisions at $\sqrt{s_{\text{NN}}} = 54.4$ GeV. It can be observed that T_{kin} increases from central to peripheral collisions, indicating that the fireball in central collisions has a longer lifetime. On the other hand, $\langle\beta_T\rangle$ decreases from central to peripheral collisions, suggesting a more rapid expansion in central collisions.

3.6 Summary

Various observables related to identified particle production in Au+Au collisions at $\sqrt{s_{\text{NN}}} = 54.4$ GeV are presented, including p_T -spectra of π^\pm , K^\pm , and $p(\bar{p})$ in mid-rapidity ($|y| < 0.1$) for nine centrality classes (0-5%, 5-10%, ..., 70-80%). Observables such as average transverse momentum ($\langle p_T \rangle$), particle yields (dN/dy), particle ratios, and kinetic freeze-out properties are shown as functions of energy and collision centrality. These results are compared with corresponding findings from BES-I energies at $\sqrt{s_{\text{NN}}} = 7.7$ to 39, GeV, as well as higher energy results from STAR at 62.4 and 200 GeV in Au+Au collisions.

The $\langle p_T \rangle$ values for π , K , and p increase from peripheral to central collisions in Au+Au

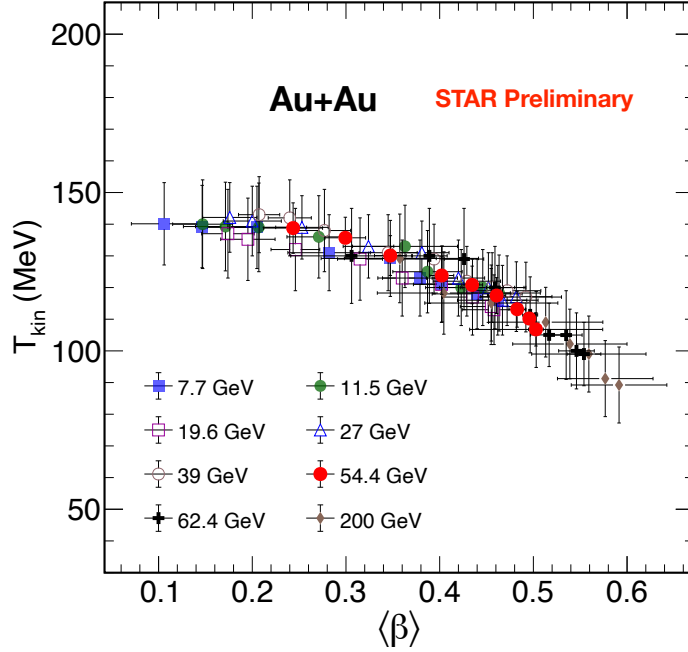


Figure 3.23: The variation of kinetic freeze-out temperature (T_{kin}) with the mean transverse velocity ($\langle\beta\rangle$) in Au+Au collisions at $\sqrt{s_{NN}} = 54.4$ GeV. The uncertainties shown include both total systematic and statistical uncertainties added in quadrature.

collisions at $\sqrt{s_{NN}} = 54.4$ GeV, indicating a growing radial flow effect in more central collisions. This rise in $\langle p_T \rangle$ from π to K and then to p suggests an increase in radial flow with the particle mass.

The integrated particle yields dN/dy in mid-rapidity ($|y| < 0.1$) of π^\pm , K^\pm , and p do not scale with $\langle N_{part} \rangle$; rather, they slowly increase from peripheral to central collisions in Au+Au collisions at $\sqrt{s_{NN}} = 54.4$ GeV. However, it does not show a strong centrality dependence for \bar{p} . For energy dependence, the dN/dy for π , K , and \bar{p} increases as collision energy rises, whereas for p , it decreases with increasing energy. This behavior is directly influenced by baryon stopping at lower RHIC energies.

The π^-/π^+ ratio exhibits a weak centrality dependence, indicating a consistent pion production mechanism across different collision regions. The flat K^-/K^+ ratio suggests similar production mechanisms and collective flow for kaons regardless of centrality, consistent with lower-energy observations. The \bar{p}/p ratio increases from central to peripheral collisions, reflecting the greater proton-antiproton annihilation and baryon stopping in central collisions compared to peripheral ones at RHIC energies. The particle ratios K^+/π^+ and K^-/π^- rise from peripheral to mid-central collisions and then level off with $\langle N_{part} \rangle$, reflecting strangeness equilibrium as the system transitions from a canonical to grand-canonical description. This behavior, also influenced by baryon stopping, is consistent with results at $\sqrt{s_{NN}} = 54.4$ GeV. The \bar{p}/π^- ratio remains constant across different centralities, showing no significant dependence on net-baryon density at higher energies

but more influence at lower energies. The p/π^+ ratio increases with centrality at lower RHIC energies but stabilizes at higher energies, following the trend observed in 62.4 and 200 GeV collisions.

For energy dependence, the π^-/π^+ ratio, initially greater than one at lower energies, approaches unity as beam energy increases, indicating the growing dominance of pair production over resonance decays. The K^-/K^+ ratio also increases with collision energy and nears unity. This is due to a shift from associated production, which mainly creates K^+ , to pair production, which generates equal amounts of K^+ and K^- , as energy rises. The \bar{p}/p ratio increases with $\sqrt{s_{NN}}$, approaching unity at higher energies, reflecting a decrease in net baryon density.

Kinetic freeze-out parameters are obtained from a simultaneous Blast-wave fit to π^\pm , K^\pm , and $p(\bar{p})$ spectra in Au+Au collisions at $\sqrt{s_{NN}} = 54.4$ GeV. The kinetic freeze-out temperature T_{kin} decreases from peripheral to central collisions, suggesting a short-lived fireball in peripheral collisions. Conversely, the average flow velocity $\langle\beta\rangle$ increases from peripheral to central collisions, indicating significant radial flow effects in central collisions. This demonstrates an interesting anti-correlation between T_{kin} and $\langle\beta\rangle$.

Chapter 4

Energy dependence of particle production in Au+Au collisions using AMPT model

4.1 Introduction

Heavy-ion collision experiments offer a unique opportunity to explore the behavior of nuclear matter under extreme energy densities and temperatures. QCD, the theory that describes the strong nuclear force, predicts that at the extreme energy densities produced in heavy-ion collisions, hadronic matter undergoes a transition into a deconfined state of quarks and gluons, known as QGP [28, 91, 146–148]. Advanced research facilities such as RHIC at BNL and the LHC at CERN are dedicated to investigating various properties of the QGP. A key objective of these experiments is to map the QCD phase diagram, commonly represented as temperature (T) versus baryon chemical potential (μ_B). In pursuit of this goal, RHIC launched the Beam Energy Scan (BES) program in 2010, gathering data from Au+Au collisions at $\sqrt{s_{NN}} = 7.7 - 200$ GeV. The BES program covered a broad range of μ_B values, from 20 to 420 MeV [94–104]. Lattice QCD calculations suggest that the phase transition from hadronic matter to QGP takes place within this range of μ_B [149].

In this chapter, we study the bulk properties of the system in Au+Au collisions at $\sqrt{s_{NN}} = 7.7, 27, 39, 62.4,$ and 200 GeV using the multi-phase transport (AMPT) model. We utilize three distinct sets of input parameters for both the string melting (AMPT-SM) and default (AMPT-Def) versions of AMPT [150]. Key bulk properties such as transverse momentum (p_T) spectra, integrated yields (dN/dy), mean transverse mass ($\langle m_T \rangle$), and particle ratios across various collision energies are analyzed. Additionally, we investigate the kinetic freeze-out (KFO) parameters by fitting the transverse momentum spectra using a hydrodynamically inspired blast-wave model [151]. KFO represents the point of last

scattering for hadrons produced in heavy-ion collisions, defining the surface where their momentum get fixed. The study of freeze-out properties provides crucial insights into the evolution of the medium produced in heavy-ion collisions, offering a deeper understanding of the dynamics and behavior of the system under extreme conditions.

A Multi-Phase Transport (AMPT) model

The AMPT model is a hybrid Monte Carlo event generator designed to simulate the dynamics of relativistic heavy-ion collisions [150]. AMPT stands for A Multi-Phase Transport model, a sophisticated hybrid approach for simulating heavy-ion collisions at ultra-relativistic energies [152–154]. The AMPT model generates fluctuating initial conditions using the Heavy Ion Jet INteraction Generator (HIJING) model [155]. HIJING provides a detailed description of the spatial and momentum distributions of both minijet partons and soft string excitations in the early stages of a heavy-ion collision. These initial conditions incorporate the inherent event-by-event fluctuations in the positions and momenta of the produced particles, which are crucial for accurately modeling the complex dynamics of the collision. The inclusion of these fluctuations allows the AMPT model to more realistically simulate the subsequent evolution of the system, capturing the effects of initial state variations on the final observables, such as particle spectra, collective flow, and correlations in heavy-ion collisions. The evolution of partonic interactions within the AMPT model is governed by Zhang’s Parton Cascade (ZPC) [156], which simulates the scattering and propagation of partons during the early stages of a heavy-ion collision. The parton-parton scattering process is characterized by the differential cross-section, which is given by the formula:

$$\frac{d\sigma}{dt} \approx \frac{9\pi\alpha_s^2}{2(t - \mu^2)^2}, \quad (4.1)$$

where σ represents the cross-section of partonic two-body scattering, t is the Mandelstam variable corresponding to four-momentum transfer, α_s is the strong coupling constant, and μ denotes the Debye screening mass in the partonic medium. This expression describes how partons interact within the evolving system, accounting for the screening effects that reduce the range of strong interactions due to the presence of a dense medium. The ZPC model is crucial for understanding the transport properties of partons, which influence the formation and evolution of the QGP and contribute to observable signatures, such as jet quenching and collective flow, in heavy-ion collisions.

The Debye screening mass, μ , is affected by medium effects, which in turn have a significant impact on the partonic scattering cross-section, σ . When μ is treated as medium-dependent, it allows for more accurate simulations that better match experimental observations. Moreover, while the total particle multiplicity in a collision appears to

be relatively insensitive to changes in σ , the elliptic flow, v_2 , can be strongly influenced. Specifically, a larger σ tends to enhance the elliptic flow, leading to more pronounced collective behavior in the final-state particles [157]. This sensitivity to the partonic cross-section underscores the importance of accurately modeling partonic interactions to capture the underlying dynamics of the Quark-Gluon Plasma and its subsequent evolution.

In the AMPT-Def version, the formation of hadrons from quarks and antiquarks is governed by the Lund String Model, which utilizes a symmetric fragmentation function described by:

$$f(z) \propto z^{-1}(1-z)^a \exp(-bm_T^2/z), \quad (4.2)$$

where z represents the light-cone momentum fraction of the produced hadrons relative to the fragmenting string. The parameters a and b , known as Lund string fragmentation parameters, control the shape of the fragmentation function, while m_T is the transverse mass of the produced hadrons [158]. This mechanism determines how the momentum is distributed among the hadrons during the fragmentation process.

In contrast, the String Melting version (AMPT-SM) replaces this hadronization approach with a quark coalescence model, where quarks and antiquarks directly recombine to form hadrons. This method is particularly suited for environments with high parton densities, such as those found in relativistic heavy-ion collisions. The average squared transverse momentum, $\langle p_T^2 \rangle$, of produced particles is directly proportional to the string tension, κ , which represents the energy per unit length of a string. The string tension can be expressed as:

$$\langle p_T^2 \rangle \propto \kappa = \frac{1}{b(2+a)},$$

where a and b are the parameters governing the fragmentation process. As shown in Eq. (4.2), these parameters play a crucial role in determining the transverse momentum distribution of particles produced in heavy-ion collisions. Specifically, higher values of a and/or b result in a smaller $\langle p_T^2 \rangle$, leading to a sharper, more peaked p_T spectrum. Conversely, smaller values of a and b result in a flatter p_T distribution, indicating a broader range of transverse momenta among the produced particles [153]. This relationship highlights the sensitivity of particle spectra to the underlying fragmentation dynamics and the influence of string tension on the particle production mechanisms in heavy-ion collisions.

The AMPT takes initial conditions from HIJING [155]. This process includes the spatial and momentum distributions of minijet partons and soft string excitations. The subsequent evolution of these minijet partons, predominantly composed of gluons, is modeled using Zhang's Parton Cascade (ZPC) model [156], which currently accounts for parton-parton elastic scatterings with an in-medium cross section based on perturbative QCD.

ZPC governs partonic interactions, where the differential scattering cross-section is approximated as:

$$\frac{d\sigma}{dt} \approx \frac{9\pi\alpha_s^2}{2(t - \mu^2)^2}, \quad (4.3)$$

Here, σ represents the parton-parton scattering cross-section, t is the Mandelstam variable for three-momentum transfer, α_s is the strong coupling constant, and μ is the Debye screening mass in partonic matter. In the ZPC model, the elastic scattering cross section is determined by a parameterized formula involving the strong coupling constant (α_s), Mandelstam variables (s and t), and an effective screening mass (μ) dependent on the temperature and density of partonic matter. Following minijet parton interactions, the model incorporates the Lund string fragmentation model, as implemented in the PYTHIA program, to facilitate the fragmentation of minijet partons and their combination with parent strings.

The default AMPT model has demonstrated success in reproducing measured rapidity distributions, particle ratios, and spectra of low transverse momentum pions and kaons in heavy-ion collisions at the SPS and RHIC. The AMPT-SM (String Melting) version operates on the premise that once the energy density surpasses a critical threshold (approximately $1 \text{ GeV}/\text{fm}^3$), the coexistence of color strings and partons becomes energetically unfavorable. As a result, these color strings “melt” into low-momentum partons at the beginning of the ZPC stage. Unlike the default version of AMPT, where hadrons are formed through string fragmentation, the partons in the AMPT-SM version undergo hadronization via a spatial quark coalescence mechanism. In this process, nearby quarks combine to form hadrons based on their proximity and quantum numbers, rather than through string fragmentation, providing a better description of the parton-hadron transition, especially in conditions of high partonic density, such as those found in the early stages of heavy-ion collisions [159]. This approach allows the model to more accurately simulate the dynamics of systems where partonic degrees of freedom dominate, such as the QGP.

The flow chart showing the particle production in Default and String Melting version of AMPT are shown in the Fig. 4.1.

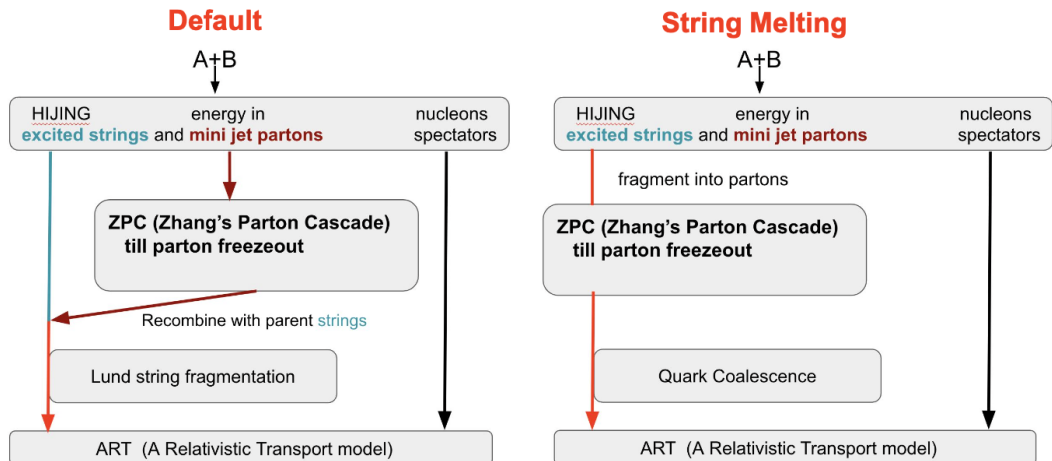


Figure 4.1: Configuration of the Default (Left) and String Melting (Right) AMPT model [150].

	a	$b(\text{GeV}^{-2})$	α_s	$\mu(\text{fm}^{-1})$	σ (mb)
Set 1	0.55	0.15	0.33	2.265	3
Set 2	2.2	0.15	0.33	2.265	3
Set 3	0.5	0.9	0.33	3.2	1.5

Table 4.1: Values of a and b related to the Lund string fragmentation function, as well as α_s and μ , significant for the parton scattering cross section [160].

The specific parameters employed in the present study are outlined in Table I. The different choices of these parameters were made by insights derived from previous studies [152–154]. In Set-1 and Set-2, the a parameter is varied, while b and σ are kept constant. A sharper p_T spectrum is expected with a larger value of a . In Set-1 and Set-3, all three parameters a , b , and σ are changed. In Set-3, these values have been reduced to observe their impact on the bulk properties. In the following sections, we will compare the AMPT model results for various configurations with experimental data.

4.2 Analysis Details

We studied the mid-rapidity p_T spectra, dN/dy , and mean transverse mass ($\langle m_T \rangle$) for π^\pm , K^\pm , p , \bar{p} , K_S^0 , Λ , and ϕ , as well as particle ratios, in the most central Au+Au collisions at $\sqrt{s_{NN}} = 7.7, 27, 39, 62.4, \text{ and } 200$ GeV. The results are provided for both the AMPT-SM and AMPT-Default versions and are compared with data from the STAR experiment. We have used the charged particle multiplicity in the pseudorapidity range $|\eta| < 0.5$ to calculate the different centralities for all energies in the model. Using the p_T -spectra, we have calculated various derived quantities such as dN/dy , $\langle m_T \rangle$, and particle ratios, and compared them with the published STAR data for different energies. We have

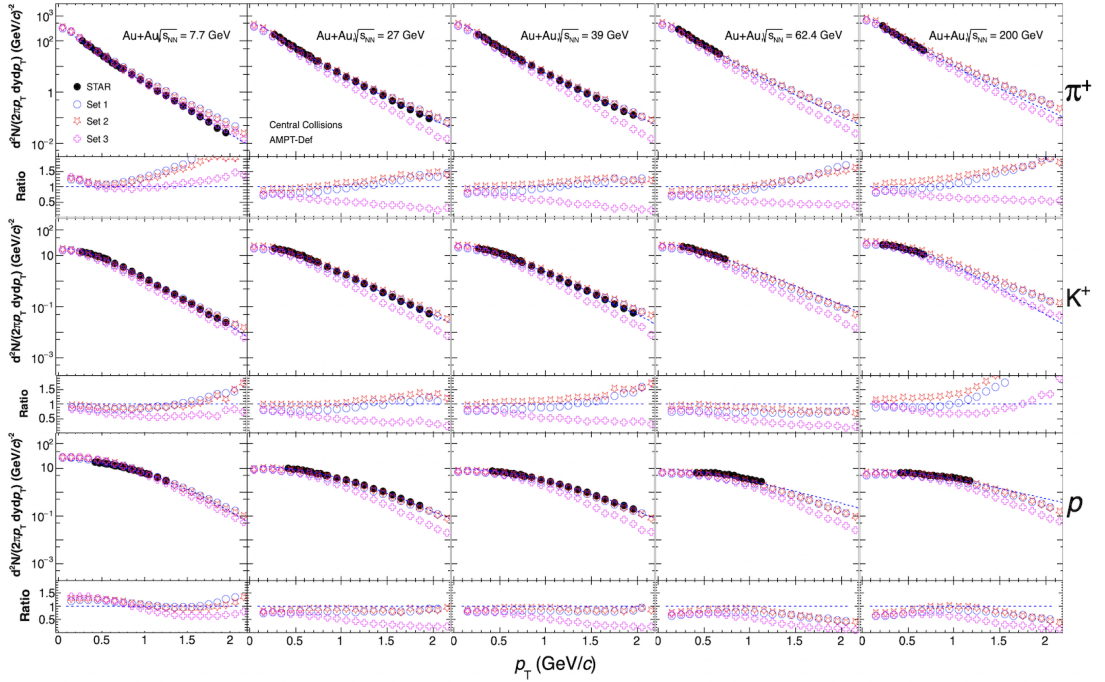


Figure 4.2: Invariant yield of π^+ (upper row), K^+ (middle row) and proton (lower row) as a function of p_T for 0 – 5% centrality in Au+Au collision at $\sqrt{s_{\text{NN}}} = 7.7, 27, 39, 62.4$ and 200 GeV using AMPT-Def versions. The AMPT results are compared with the corresponding experimental data which is fitted with a Levy function [161]. The ratio of data to fit function is also shown in the lower panels for each pad.

also employed these particle spectra to calculate freeze-out parameters such as freeze-out temperature and radial flow velocities. All these calculations are performed for three different sets listed in TABLE 4.1 using the AMPT model. The results and discussion section presents a detailed discussion of this study.

4.3 Results and Discussion

We present the p_T -spectra, dN/dy , $\langle m_T \rangle$, and ratios of π^\pm , K^\pm , p , \bar{p} , K_S^0 , Λ , and ϕ at $\sqrt{s_{\text{NN}}} = 7.7, 27, 39, 62.4, \text{ and } 200$ GeV. These results are obtained using both the AMPT String Melting and default configurations.

Transverse Momentum Spectra

Figure 4.2 compares the mid-rapidity p_T spectra of π^+ , K^+ , and p in the most central Au+Au collisions, using the AMPT-Default configuration, with STAR data at $\sqrt{s_{\text{NN}}} = 7.7, 27, 39, 62.4, \text{ and } 200$ GeV [100]. The experimental data is fitted with the Levy-Tsallis function, and the lower panel in each plot shows the ratio of the invariant yield ($d^2N/2\pi p_T dy dp_T$) from the fit function to that from AMPT-Default for different input parameters. It is observed that Set-1 and Set-2 match the data well, especially at lower

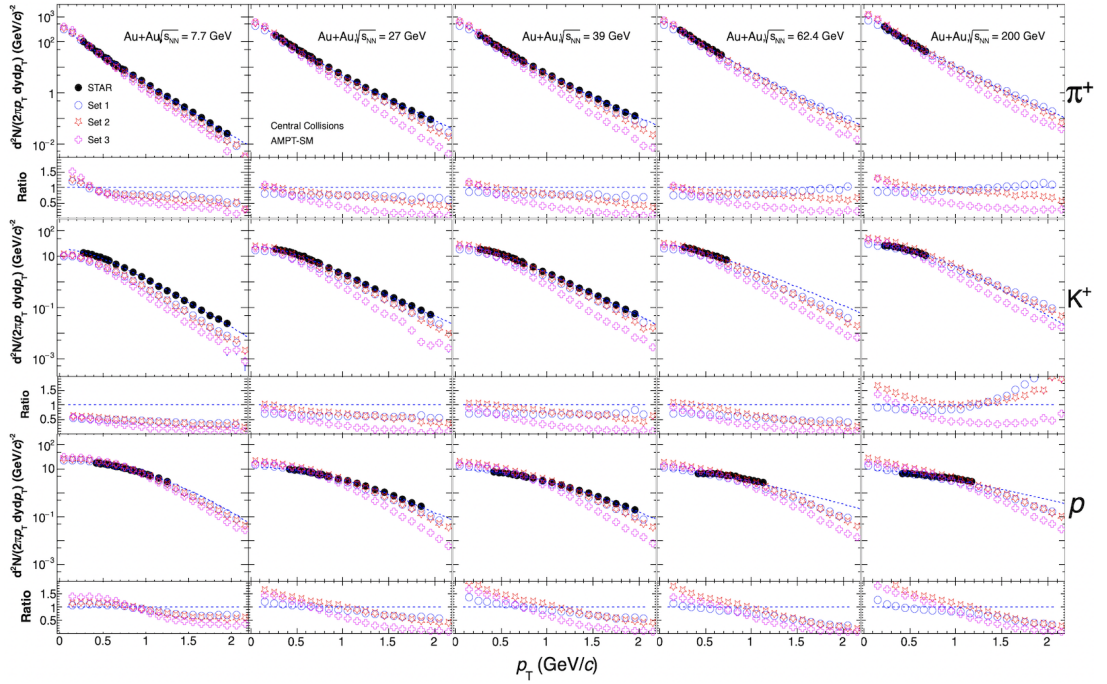


Figure 4.3: Invariant yield of π^+ (upper row), K^+ (middle row) and proton (lower row) as a function of p_T for 0 – 5% centrality in Au+Au collision at $\sqrt{s_{\text{NN}}} = 7.7, 27, 39, 62.4$ and 200 GeV using AMPT-SM versions. The AMPT results are compared with the corresponding experimental data which is fitted with a Levy function [161]. The ratio of data to fit function is also shown in the lower panels for each pad.

energies, while Set-3 consistently underestimates the data.

Similar to Fig. 4.2, Fig. 4.3 compares the mid-rapidity p_T spectra of π^+ , K^+ , and p in the most central Au+Au collisions using the AMPT-SM model with the STAR data at $\sqrt{s_{\text{NN}}} = 7.7, 27, 39, 62.4,$ and 200 GeV. The STAR experimental data is fitted using the Levy-Tsallis function, and the lower panel in each plot shows the ratio of the invariant yield from the fit function to the yield obtained with AMPT-SM for different input parameter sets. Among the three parameter sets, Set-2 describes the data well at higher energies, but it does not accurately capture the trends at lower energies. Additionally, compared to π^+ and p , the p_T spectra of K^+ show a noticeable deviation from the experimental data for all sets of the AMPT-SM model used in this study. This difference may be due to the unique properties associated with the strangeness quantum number. We have also verified that similar results hold true for antiparticles.

Furthermore, we observe that the invariant yield decreases consistently with increasing p_T across all particle types and parameter sets for both AMPT-Default and AMPT-SM. Additionally, the inverse slopes of the particle spectra follow a consistent order, with π being less steep than K , and K being less steep than p , which aligns with the trends observed in the experimental data.

Figures 4.4 and 4.5 compare the mid-rapidity p_T spectra of K_s^0 , Λ , and ϕ from the AMPT model with STAR data in the most central Au+Au collisions at $\sqrt{s_{\text{NN}}} = 7.7,$

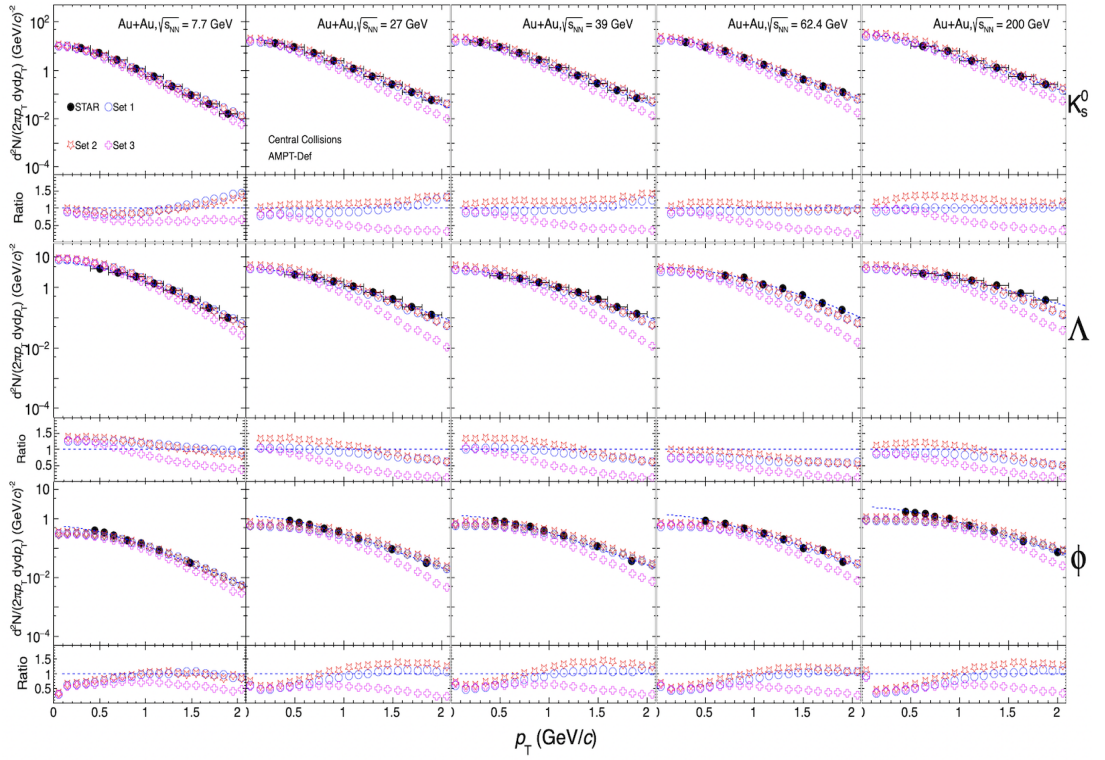


Figure 4.4: Invariant yield of K_S^0 (upper row), Λ (middle row) and ϕ (lower row) as a function of p_T for most central events in Au+Au collision at $\sqrt{s_{NN}} = 7.7, 27, 39, 62.4$ and 200 GeV are shown in each column using AMPT-Def. The ratio of data to fit function is also shown in the lower panels for each pad.

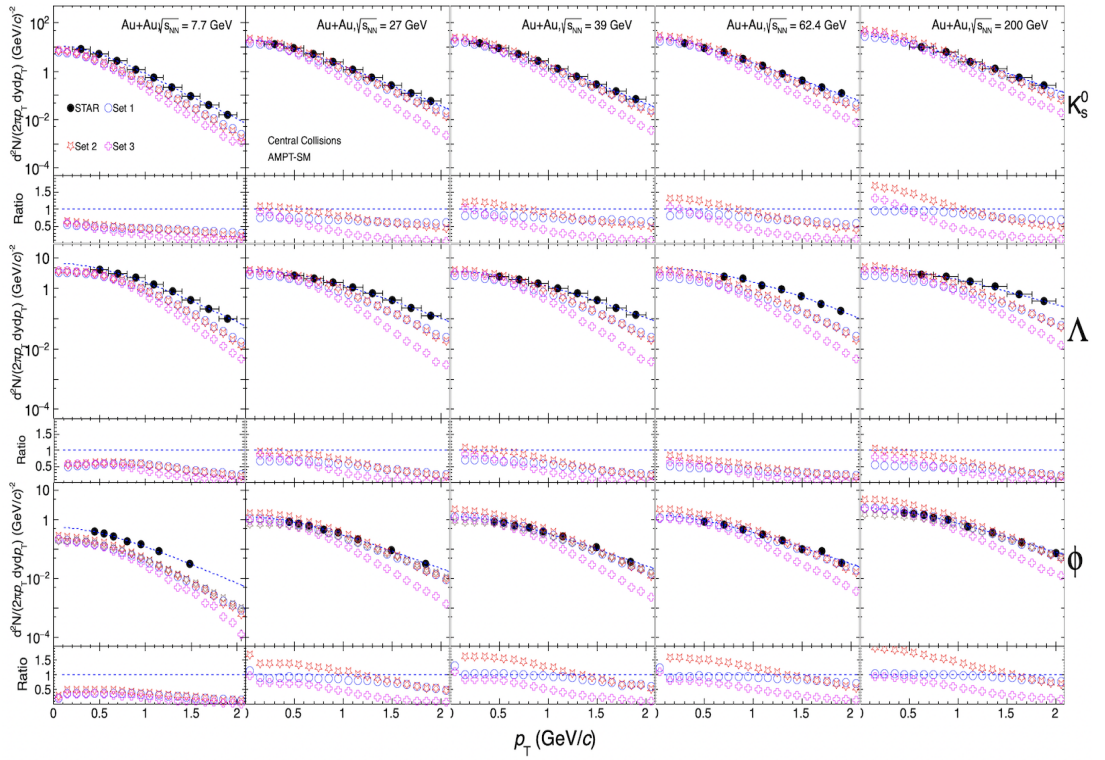


Figure 4.5: Invariant yield of K_S^0 (upper row), Λ (middle row) and ϕ (lower row) as a function of p_T for most central events in Au+Au collision at $\sqrt{s_{NN}} = 7.7, 27, 39, 62.4$ and 200 GeV are shown in each column using AMPT-SM. The ratio of data to fit function is also shown in the lower panels for each pad.

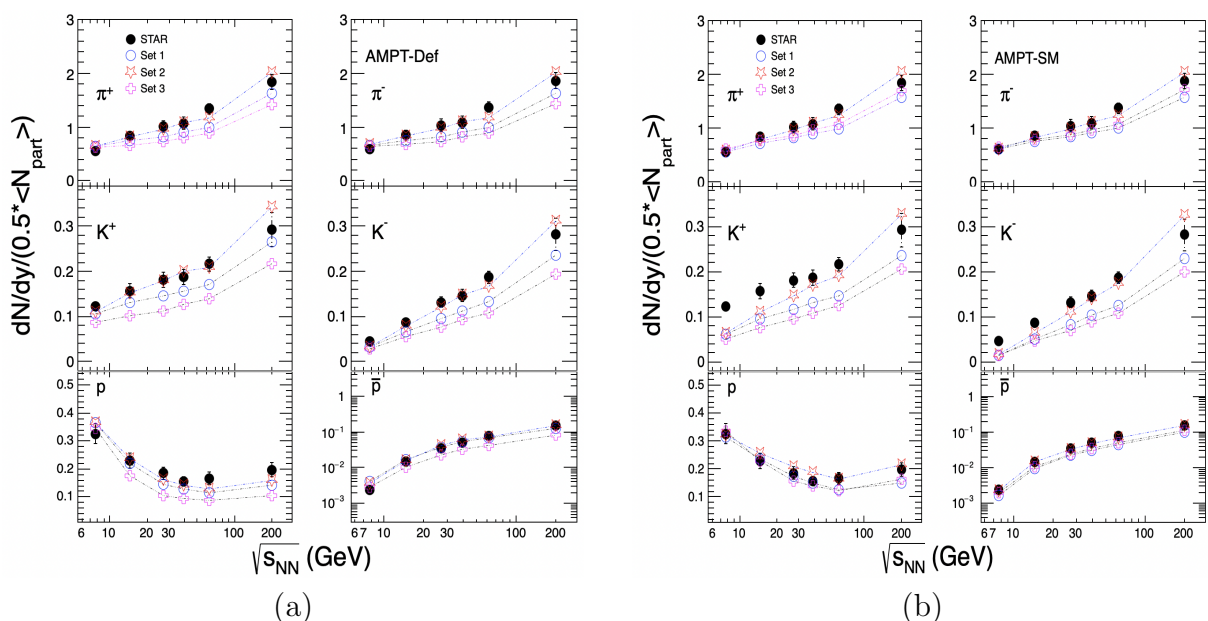


Figure 4.6: Energy dependence of $(dN/dy)/(\langle N_{\text{part}} \rangle/2)$ for particle (π^+ , K^+ , p) and anti-particle (π^- , K^- , \bar{p}) for central (0-5%) Au+Au collisions using AMPT-Def (a) and AMPT-SM (b). The AMPT results shown in open markers are compared with the corresponding experimental data (solid marker).

27, 39, 62.4, and 200 GeV for the AMPT-Default and AMPT-SM versions, respectively [162]. The STAR data is fitted with the Levy-Tsallis function, and the lower panel in each plot shows the ratio of the invariant yield from the fit function to the yield obtained from the AMPT model. We observe that, among the parameter sets, Set-1 in AMPT-Default accurately describes the p_T spectra of strange hadrons. However, in the case of AMPT-SM, no specific set consistently matches the data.

p_T integrated yield, Mean transverse mass ($\langle m_T \rangle$) and Particle Ratios

Figure 4.6 compares how the particle yields (dN/dy) for π^\pm , K^\pm , p , and \bar{p} change with energy, normalized by half of the average number of participating nucleons ($\langle N_{\text{part}} \rangle/2$), in the most central Au+Au collisions at $\sqrt{s_{\text{NN}}} = 7.7, 27, 39, 62.4,$ and 200 GeV. These results are obtained using the AMPT model and are compared with the STAR experiment data.

We observe that among the different sets of input parameters, Set-2 provides the best description of the particle yields for AMPT-Default at lower energies and AMPT-SM at higher energies, as shown in Fig. 4.6(a) and Fig. 4.6(b). The normalized yields of π^\pm , K^\pm , p , and \bar{p} are seen to increase with increasing collision energy. However, the yield of p decreases with increasing energy due to significant baryon stopping, which is more prominent at lower energies.

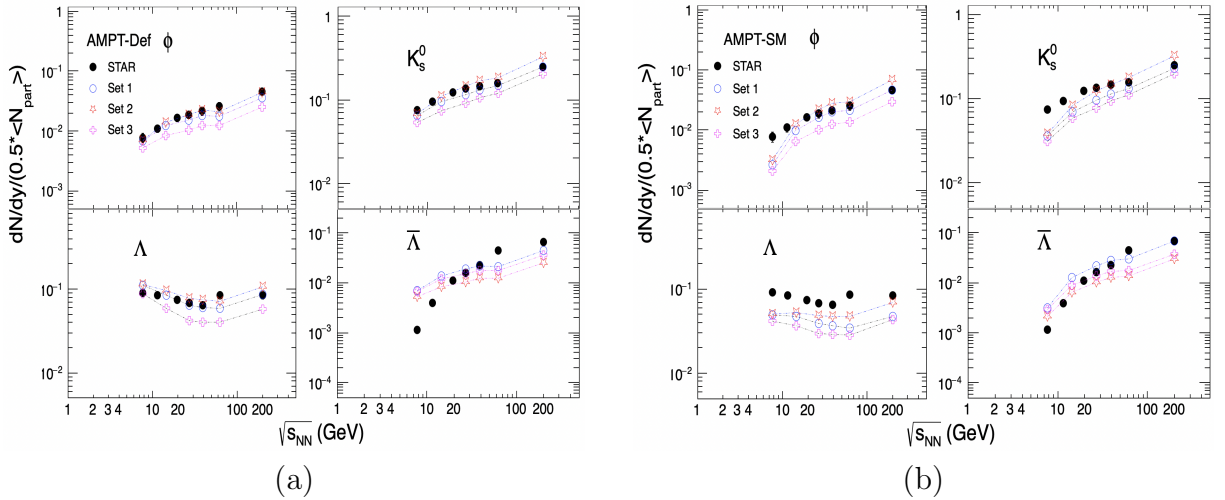


Figure 4.7: Energy dependence of $(dN/dy)/(\langle N_{\text{part}} \rangle / 2)$ for K_S^0 , Λ , ϕ , and $\bar{\Lambda}$ for central Au+Au collisions using AMPT-Def (a) and AMPT-SM (b). The AMPT results shown in open markers are compared with the corresponding experimental data (solid marker).

Figure 4.7 compares the energy dependence of dN/dy for K_S^0 , Λ , $\bar{\Lambda}$, and ϕ , normalized by $\langle N_{\text{part}} \rangle / 2$, in the most central Au+Au collisions at $\sqrt{s_{\text{NN}}} = 7.7, 27, 39, 62.4,$ and 200 GeV. These results are calculated using the AMPT model and are compared with the STAR data. We find that Set-1 and Set-2 of the AMPT-Default version better describe the yields of strange hadrons.

In a thermodynamic system, the average transverse mass, $\langle m_T \rangle - m_0$, can be an indicator of the temperature of the system, where m_0 is the rest mass of the particle. It has been suggested that the energy dependence of $\langle m_T \rangle - m_0$ might serve as a potential signal of a first-order phase transition between the hadronic medium and the QGP [163]. Figures 4.8(a) and 4.8(b) show how $\langle m_T \rangle - m_0$ changes with energy for π^\pm , K^\pm , p , and \bar{p} in the most central Au+Au collisions, calculated using the AMPT-Default and AMPT-SM models, respectively. We observe that all three sets of input parameters qualitatively capture the trend seen in the experimental data. Figures 4.9(a) and 4.9(b) display the energy dependence of $\langle m_T \rangle - m_0$ for K_S^0 , Λ , $\bar{\Lambda}$, and ϕ in the most central Au+Au collisions, also using the AMPT-Default and AMPT-SM models, respectively. We find that Set-1 of the AMPT-Default version describes the data well, while all parameter sets used in AMPT-SM tend to underpredict the data.

The energy dependence of antiparticle-to-particle ratios provides important insights into the mechanisms of particle production in heavy-ion collisions [108]. Figure 4.10 shows how the ratios π^-/π^+ , K^-/K^+ , and \bar{p}/p change with collision energy in the most central Au+Au collisions, as calculated using the AMPT model. The upper panel compares the AMPT-Default calculations with experimental data [164–170], while the lower panel shows the comparison with AMPT-SM calculations.

We observe that the π^-/π^+ ratio is greater than one at lower energies, mainly due

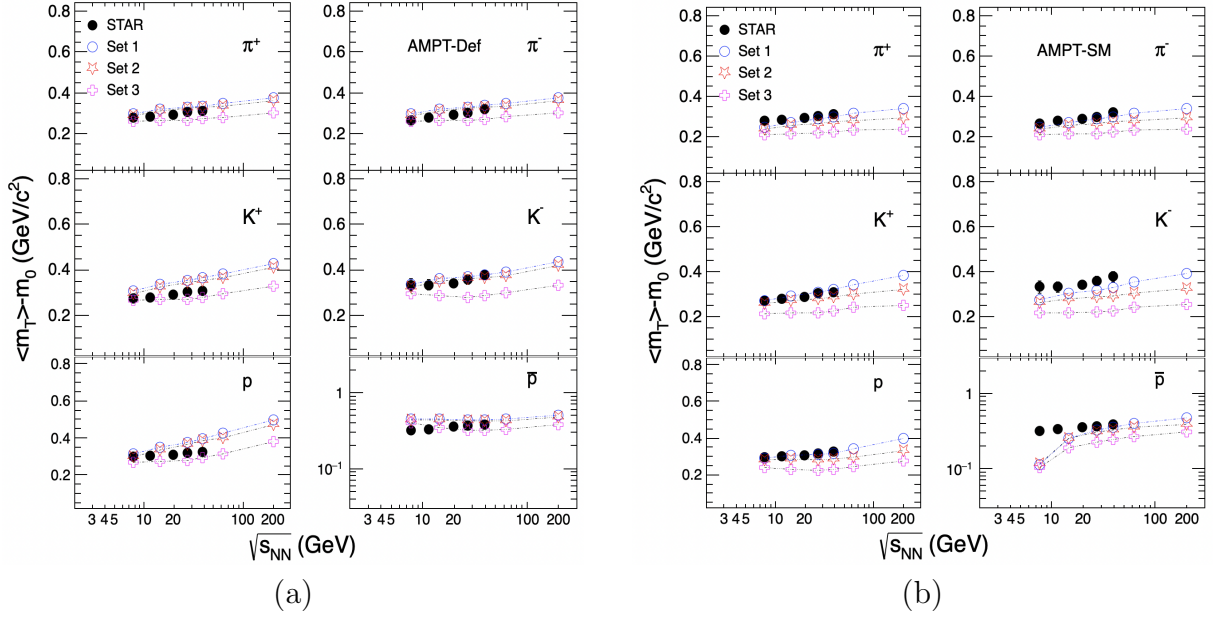


Figure 4.8: $\langle m_T \rangle - m_0$ of π^\pm , K^\pm , p , and \bar{p} as a function of $\sqrt{s_{NN}}$ at midrapidity ($|y| < 0.1$). Results are presented for 0-5% central Au+Au collisions using AMPT-Def (a) and AMPT-SM (b). The AMPT results shown in open markers are compared with the corresponding experimental data (solid marker).

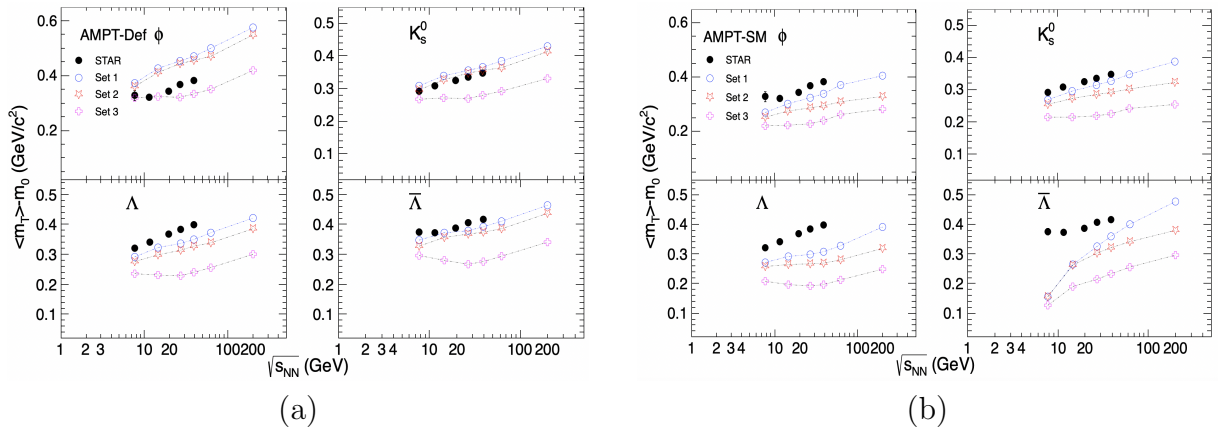


Figure 4.9: $\langle m_T \rangle - m_0$ of K_S^0 , Λ , ϕ , and $\bar{\Lambda}$ as a function of $\sqrt{s_{NN}}$ at midrapidity. Results are presented for 0-5% central Au+Au collisions using AMPT-Def (a) and AMPT-SM (b). The AMPT results shown in open markers are compared with the corresponding experimental data (solid marker).

to significant contributions from resonance decays, such as those from Δ baryons. The K^-/K^+ ratio decreases as the energy decreases, primarily due to the associated production of K^+ . Similarly, the \bar{p}/p ratio also decreases with decreasing energy, which is influenced by baryon stopping at lower energies. However, as the energy increases, all antiparticle to particle ratios approach unity, indicating the dominance of pair production at higher energies. These observations are consistent with the data.

Interestingly, the systematic effects caused by variations in model parameters tend to cancel out in particle ratios, resulting in no significant energy dependence on the input parameters. We find that all parameter sets of both AMPT-Default and AMPT-SM models are able to describe the experimental data well.

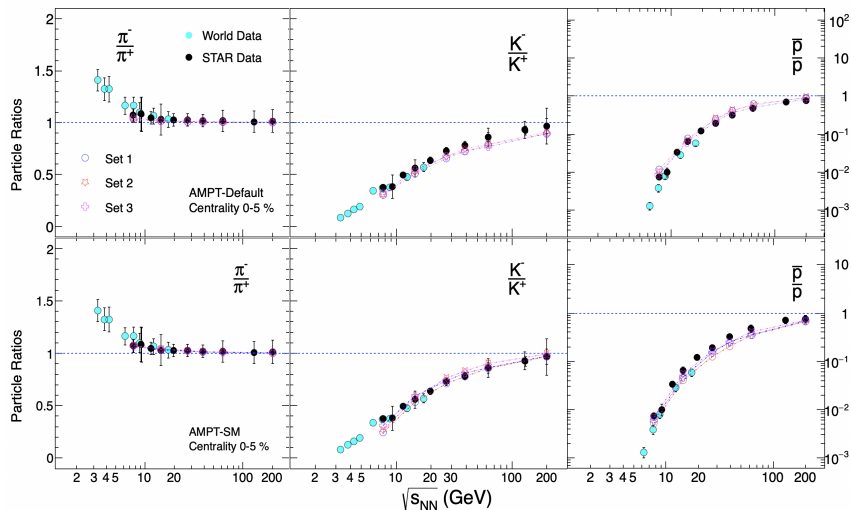


Figure 4.10: π^-/π^+ , K^-/K^+ , and \bar{p}/p ratios at midrapidity ($|y| < 0.1$) in central 0–5% Au+Au collisions at $\sqrt{s_{NN}} = 7.7, 27, 39, 62.4$ and 200 GeV using AMPT-Def (upper panel) and AMPT-SM (lower panel). The AMPT results shown in open markers are compared with the published experimental data (solid marker).

Kinetic Freeze-out Parameters

In this section, we discuss the kinetic freeze-out parameters obtained using a blast-wave model applied to Au+Au collisions at different center-of-mass energies. In this approach, we simultaneously fit the p_T spectra of π^\pm , K^\pm , p , and \bar{p} using the blast-wave model, similar to how it has been done in experimental studies [151] [101].

The blast-wave model is based on hydrodynamic principles and provides an accurate description of particle behavior at low p_T . However, it is not well-suited for describing the high-momentum (high p_T) processes that involve harder collisions. The model assumes that all particles share a common radial flow velocity profile and the same thermal freeze-out temperature [171].

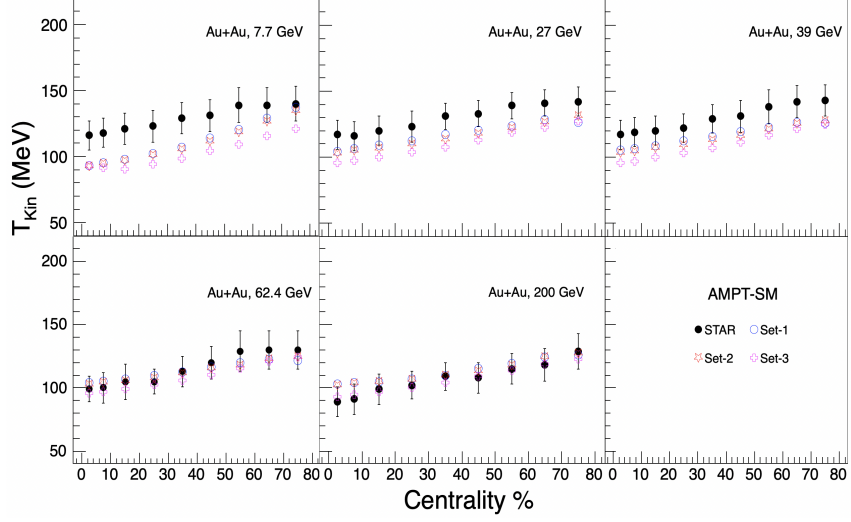


Figure 4.11: Centrality dependence of kinetic freeze-out temperature (T_{kin} in MeV) in different collision energies for three different Sets in Au+Au collisions using AMPT.

The blast-wave model, as discussed in Section 3.5.5, assumes a thermal source that is radially boosted, characterized by a kinetic freeze-out temperature (T_{kin}) and a transverse radial flow velocity (β).

Figure 4.11 illustrates how the kinetic freeze-out temperature, T_{kin} , varies with both energy and centrality in Au+Au collisions at different energies: $\sqrt{s_{NN}} = 7.7, 27, 39, 62.4,$ and 200 GeV. We observe that all the sets of input parameters used in the AMPT-SM model are able to capture the trend where T_{kin} decreases as centrality increases, which is consistent with experimental data.

Figure 4.12 shows how the average radial flow velocity, $\langle\beta\rangle$, changes with centrality in Au+Au collisions at different energies. We observe that none of the input parameter sets for the AMPT-SM model reasonably describe the data for $\langle\beta\rangle$.

In Figure 4.13, an anti-correlation between T_{kin} and $\langle\beta\rangle$ is presented. This figure shows that all configurations of the AMPT-SM model capture this anti-correlation behavior, although Set-3 deviates more significantly from the experimental data compared to the other two sets.

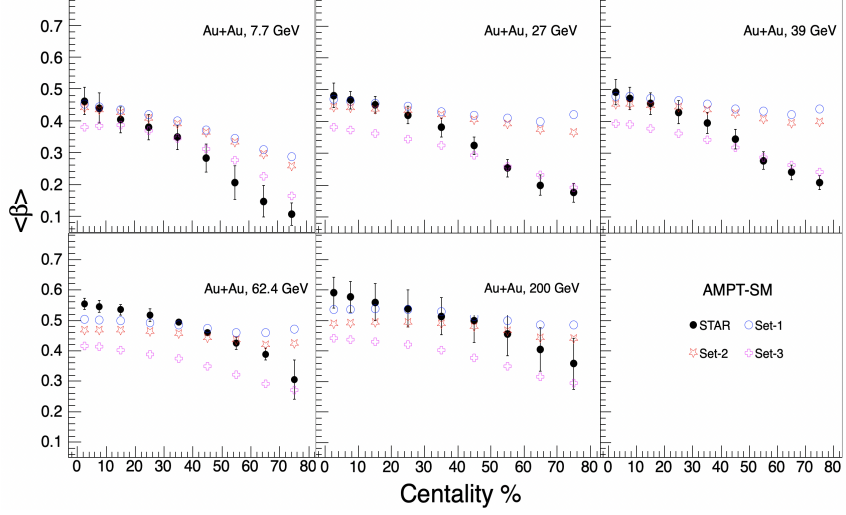


Figure 4.12: Centality dependence of $\langle\beta\rangle$ in different collision energies for three different Sets in Au+Au collisions using AMPT.

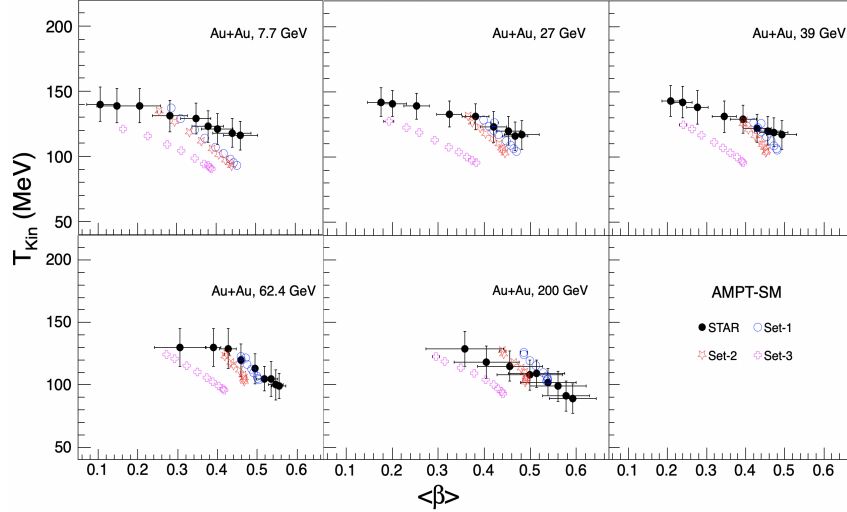


Figure 4.13: Variation of T_{kin} with $\langle\beta\rangle$ for three different Sets for different collision energies. The centrality increases from left to right for a given energy.

Summary

This study presents the p_T , dN/dy , $\langle m_T \rangle$, and particle ratios for various particles like π^\pm , K^\pm , p , \bar{p} , K_s^0 , Λ , and ϕ in Au+Au collisions at different energies: $\sqrt{s_{NN}} = 7.7, 27, 39, 62.4, \text{ and } 200 \text{ GeV}$. The results are obtained using both the AMPT Default and String Melting models and are compared with experimental data.

The AMPT model accurately captures the p_T spectra trends for π^\pm , K^\pm , p , \bar{p} , especially at lower energies, with Set-1 and Set-2 of the AMPT-Default model performing best and at higher energy for AMPT-SM version. However, AMPT-SM shows some discrepancies, particularly for strange hadrons like K^+ . The study also shows that particle yields generally increase with energy, although p yields decrease due to baryon stopping at lower energies. For strange hadrons, such as K_s^0 , Λ , $\bar{\Lambda}$, and ϕ , Set-1 and Set-2 of the AMPT-Default version provide a better description of the p_T spectra across different energies.

Set-2 of the AMPT-Default and AMPT-SM versions best describe the yields of π^\pm , K^\pm , p , and \bar{p} as energy increases, while Set-1 and Set-2 of the AMPT-Default version with higher cross-section value better describe the yields of K_s^0 , Λ , $\bar{\Lambda}$, and ϕ , across different energies.

All three sets of input parameters qualitatively capture the trend of $\langle m_T \rangle - m_0$ with energy for π^\pm , K^\pm , p , and \bar{p} , while AMPT-Default version best describes the data for K_s^0 , Λ , $\bar{\Lambda}$, and ϕ , with AMPT-SM underpredicting the data across all parameter sets.

The particle ratios π^-/π^+ , K^-/K^+ , and \bar{p}/p from both the AMPT-Default and AMPT-SM models match well with experimental data across different energies, as the systematic effects caused by variations in model parameters tend to cancel out in particle ratios.

For kinetic freeze-out study, all input parameter sets of the AMPT-SM model successfully capture the trend of decreasing kinetic freeze-out temperature (T_{kin}) with increasing centrality, consistent with experimental data. However, none of the parameter sets provide a reasonable description of the average radial flow velocity ($\langle \beta \rangle$). Additionally, the AMPT-SM model configurations accurately capture the observed anti-correlation between T_{kin} and $\langle \beta \rangle$, with Set-3 deviating more significantly from the data.

Overall, the AMPT model offers a good representation of the experimental data for the bulk properties of various particles (π^\pm , K^\pm , p , \bar{p} , K_s^0 , Λ , and ϕ) across different energy ranges, using specific input parameter sets.

Chapter 5

STAR Forward Upgrade

5.1 Introduction

Precise measurements of gluon and sea quark distributions in protons and nuclei offer a key to unlocking profound questions about nuclear properties. These inquiries explore both the spatial and momentum distributions of these constituents, as well as the contribution of sea quarks and gluons (and their orbital angular momentum) to the nucleon spin. These measurements also address important questions, such as whether the density of gluons reaches a saturation point within nuclei at high energies and, if so, what the universal characteristics of gluonic matter are in this saturated state. A central question is how do quarks of various flavors become colorless hadrons in nuclear matter, and its impact on the quark confinement mechanisms within nucleons [172].

To comprehensively address these scientific goals, experimental measurements spanning a broad range of Bjorken- x values, covering both high and low regimes, are crucial [173]. The STAR forward physics program gives a unique opportunity to explore these questions and contribute to a deeper understanding of the underlying physics. This effort is supported by the significant upgrades implemented in the detectors within the forward rapidity range ($2.5 < \eta < 4$), featuring the integration of a Forward Calorimeter System (FCS) and an enhanced Forward Tracking System (FTS).

The prior use of the forward pion detector and the forward meson spectrometer by STAR has demonstrated its ability to address key questions in cold QCD physics through detailed measurements in the forward rapidity region. PHENIX and STAR results reveal significant transverse single-spin asymmetries (A_N) in inclusive hadron production. Initially observed in $p + p$ collisions at fixed-target energies and low p_T , these asymmetries now extend to RHIC's highest energy ($\sqrt{s} = 500, \text{ GeV}$) and larger p_T . This trend is illustrated in Figure 5.1, which presents a comprehensive overview of global data as a function of Feynman- x . Notably, these asymmetries demonstrate minimal dependence on \sqrt{s} across a broad energy spectrum ranging from 4.9 GeV to 500 GeV.

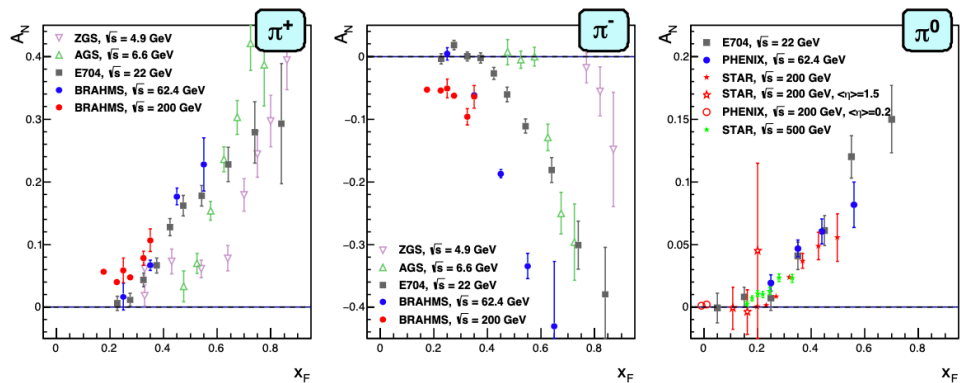


Figure 5.1: Measurements of transverse single spin asymmetry for both charged and neutral pions across various center-of-mass energies, as a function of Feynman- x [174].

The forward upgrade will facilitate access to previously observed charged hadron asymmetries at the highest center-of-mass energies at RHIC. It will validate the correlation between charged hadron asymmetries and center-of-mass energy.

The unique capability of the RHIC enables collisions with polarized proton beams. Analyzing these collisions, especially at forward rapidities, could enhance our understanding of nucleon spin structure. A complete understanding of the nucleon spin structure requires not only unpolarized and helicity distributions but also the transversity distribution. Transversity, defined as the net transverse polarization of quarks within a transversely polarized proton, offers crucial insights into the spin structure of hadrons. The disparity between helicity and transversity distributions for quarks and antiquarks establishes a direct x -dependent link to non-vanishing orbital angular momentum components in the wave function of the proton. Recent advancements in transversity measurements have sparked interest in accessing the nucleon tensor charge. Calculating the transverse charge on the lattice with high precision enables comparisons between experimental results and early-stage QCD calculations. These calculations are vital for understanding how hadronic observables in low-energy reactions can be sensitive to potential effects beyond the standard model (BSM), such as tensor couplings to hadrons. BSM physics includes phenomena like interactions with ultra-cold neutrons and nuclei, which can offer insights into new physics through anomalies in hadronic reactions. Successful transversity measurements in semi-inclusive deep-inelastic scattering (SIDIS) experiments have utilized symmetric distributions of single pions, associating transversity with the transverse-momentum-dependent (TMD) Collins fragmentation function [175]. Additionally, azimuthally asymmetric distributions of di-hadrons have linked transversity to the “interference fragmentation function” (IFF) within the collinear factorization framework [176]. However, current SIDIS experiments have not probed beyond $x \sim 0.3$ for Bjorken- x values in transversity extraction.

Forward upgrade provides access to transversity in the $x > 0.3$ region by extending

measurements of di-hadron and Collins asymmetries in the forward direction. This valence quark region, crucial for calculating the tensor charge, encompasses 70% of its contribution from $0.1 < x < 1.0$.

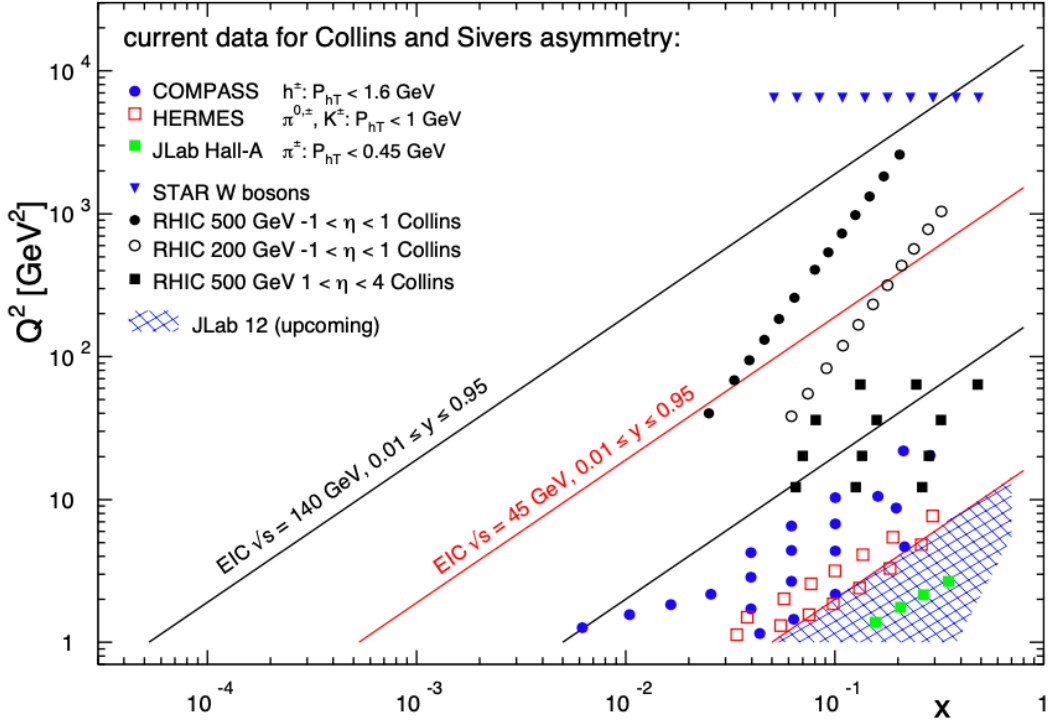


Figure 5.2: The x - Q^2 plane includes future EIC and JLab-12 GeV data, current SIDIS data, and RHIC W-boson data, all sensitive to the Sivers function and transversity multiplied by the Collins FF in the TMD framework [174].

Forward region measurements of STAR, particularly of Collins and di-hadron asymmetry sensitive to transversity, aim to explore new x -ranges and investigate transversity flavor dependence. In Figure 5.2, the coverage of $x - Q^2$ that can be achieved with RHIC measurements is shown, in comparison to the anticipated coverage from the future EIC, JLab-12, and the existing semi-inclusive deep inelastic scattering world data.

The need for precise assessments of nuclear parton distribution functions (nPDFs) at low x values is crucial for understanding the initial conditions in A+A collisions. Figure 5.3 illustrates how forward instrumentation of STAR aims to investigate the moderate Q^2 and medium-to-low x regions, which are currently devoid of data and expected to show substantial nuclear effects on sea quarks and gluons. Utilizing forward calorimetry, which is key for distinguishing electrons from hadrons, facilitates the analysis of sea quark nuclear modifications through the Drell-Yan R_{pA} ratio, a method uniquely free from the influence of final state dynamics and suited for sea quark suppression studies. Likewise, integrating charged particle tracking with electromagnetic calorimetry supports the detection of direct photon suppression at forward rapidities, serving as an effective technique to examine the

anticipated suppression of gluons at low x .

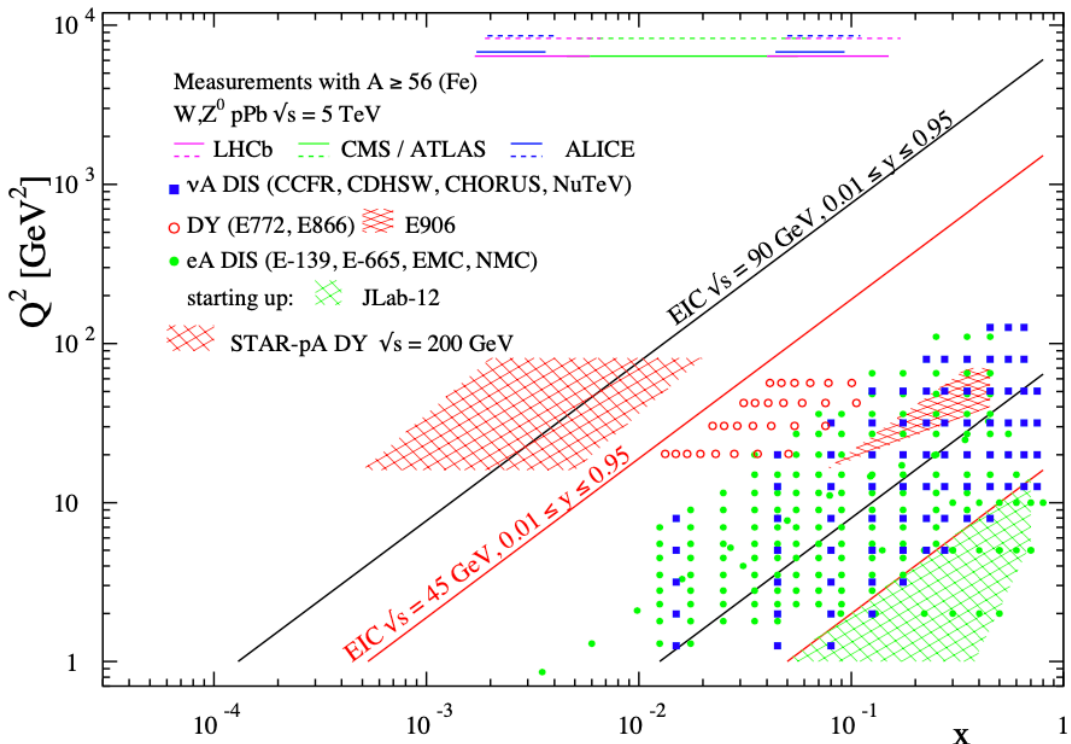


Figure 5.3: The range of kinematic exploration across x - Q^2 by past, present, and future experiments, which restricts nPDFs with precise parton kinematics on an event-by-event basis and excludes fragmentation in the final state [174].

The upgraded Forward Tracking System features an advanced combination of a FST combining 3 Silicon disks and 4 Small-Strip Thin Gap Chamber (sTGC) wheels. Illustrated in Figure 5.4, the silicon detectors are positioned in proximity to the interaction point at z -locations ranging from approximately 140 cm to 200 cm. In contrast, the sTGCs are situated at greater distances, with z -locations spanning from 300 cm to 360 cm, positioned within the magnet pole tip opening. Notably, the silicon sensors are situated within the region of the homogeneous 0.5 T STAR magnetic field, while the sTGCs reside in a region where the magnetic field undergoes a gradual change, introducing increased complexity to charged particle tracking.

Notably, the construction of the electromagnetic and hadronic calorimeters reached successful completion by the end of 2020. These components were not only fully installed but also meticulously instrumented and commissioned during the RHIC running period in 2021. Furthermore, the tracking detectors were installed according to schedule in the summer and fall of 2021, ensuring their readiness for the commencement of Run-22. It is noteworthy that the entire process of constructing, installing, and commissioning these four systems was accomplished during the challenging period of the pandemic. Despite the adversities faced, substantial efforts were dedicated to maintaining the forward up-

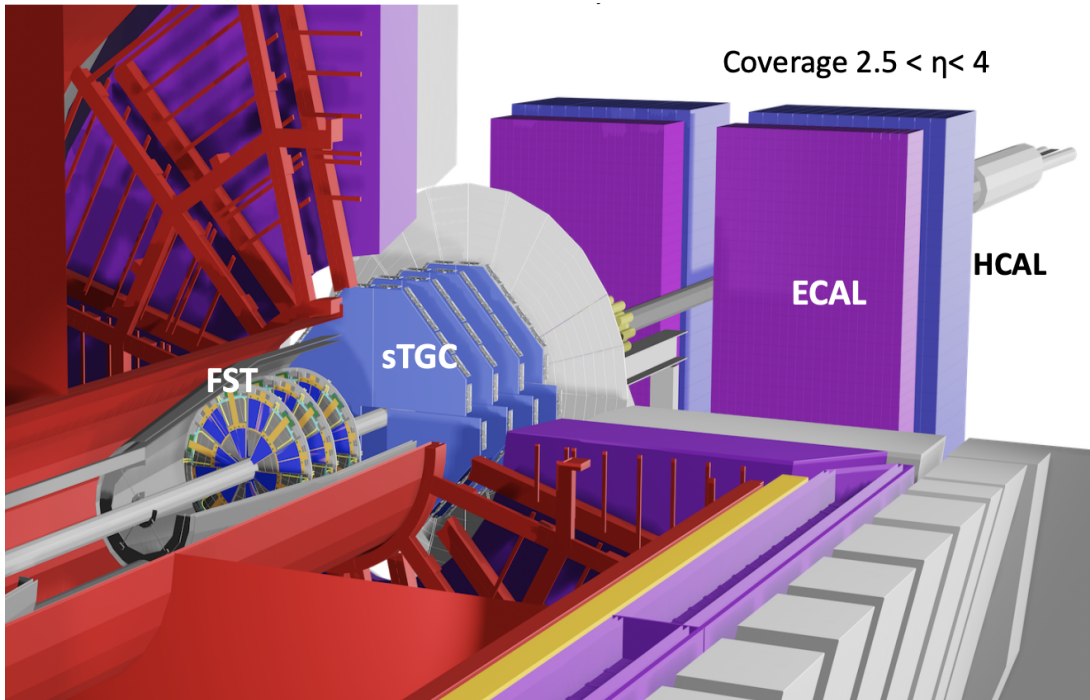


Figure 5.4: An illustration of the STAR detector includes the forward tracking system and calorimeter. Silicon mini-strip disk detectors are close to the interaction point, followed by pentagonal sTGC detectors. The event plane detector (grey disk) acts as a preshower detector for the forward calorimeter system (purple and blue)[174].

grades on schedule. Remarkably, during Run-22, the forward upgrades demonstrated exceptional performance, seamlessly collecting data throughout the run despite difficulties encountered on the machine side. Looking ahead, the forward upgrades are poised to continue their data collection efforts in parallel with sPHENIX through Run-25.

5.2 Forward Upgrade

The STAR Forward Upgrade comprises two key detector systems designed to enhance the experimental capabilities of the STAR experiment. The first detector system is the FTS, which includes three Silicon discs, known as the Forward Silicon Tracker (FST), and four small-strip Thin Gap Chambers (sTGC). This system is integral for precise tracking of particles as they move through the forward region of the detector. The second system is the Forward Calorimeter System (FCS), which consists of an Electromagnetic Calorimeter (ECal) and a Hadronic Calorimeter (HCal). The FCS is crucial for measuring the energy of particles, enabling a detailed study of particle interactions in the forward region.

5.2.1 Forward Tracking System

The FTS is a sophisticated assembly within the STAR Forward Upgrade, consisting of three Silicon discs and four sTGC. The Silicon discs, collectively known as the FST, are responsible for high-precision tracking of charged particles. These discs are complemented by the sTGCs, which enhance the system's ability to determine particle trajectories accurately. Together, these components provide vital tracking information, enabling us to reconstruct the paths of particles produced in high-energy collisions with great precision.

5.2.1.1 Forward Silicon Tracker

Aim of including the FST in forward upgrade in the STAR experiment at Brookhaven National Laboratory is having better detection of charged particles in forward rapidity region. FST is one of the sub-detectors of the forward upgrade, which measures the products of these ion collisions in the forward direction and can reconstruct their three-dimensional (3D) trajectories and momentum. FST consists of three layers of identical Silicon disks, each disk housing 12 modules. Each module is equipped with 3 single-sided double-metal Silicon mini-strips sensors, read out by 8 APV chips. The inner sensor radius of each disk is 5-16.5 cm and the outer sensor radius is 16.5-28 cm, with both the inner and outer sensors being approximately 12 cm long. The sensors are made up of 320 μm microstrip sensors, with the inner sensor containing 4x128 strips and the outer sensor containing 64 strips. The APV25 frontend readout chip, designed for CMS Silicon strip detector, consists of 128 front-end input pads and control/output pads, preamplifier, shaper, 192 analog pipelines, capacitor filter, and multiplexer [177]. The chip is fabricated in a 0.25 μm CMOS process, consuming approximately 360 mW/chip and occupying an area of about 1 cm^2 . The silicon disks are connected to electronic readout chains through flexible hybrids made of 25 μm thick Kapton and 17.5-35 μm thick Cu layers. There are also inner and outer signal cables, T-boards, patch panel boards, readout modules, readout controllers, crates, and cooling systems that are required for the FST to function. The mechanical structure is a key component of the FST and is designed to support the sensor modules and assemble the detector. It consists of inner and outer hybrid structures, cooling tubes, and structures. The FST is designed to have 484 modules, with each module containing two silicon sensors and eight APV25 chips. The mechanical and electronic components are designed to support the sensor modules assembly and to allow for integration with the supporting structure. Figure 5.5 shows a figure of 3 silicon discs and its module [178].

The successful installation of the FST was completed on August 13th, 2021, marking a significant milestone. Inaugural collision data for pp collisions at 510 GeV were recorded on December 15, 2021. Throughout the entirety of Run-22, the FST exhibited seamless operation, running smoothly without significant interruptions. The implementation of

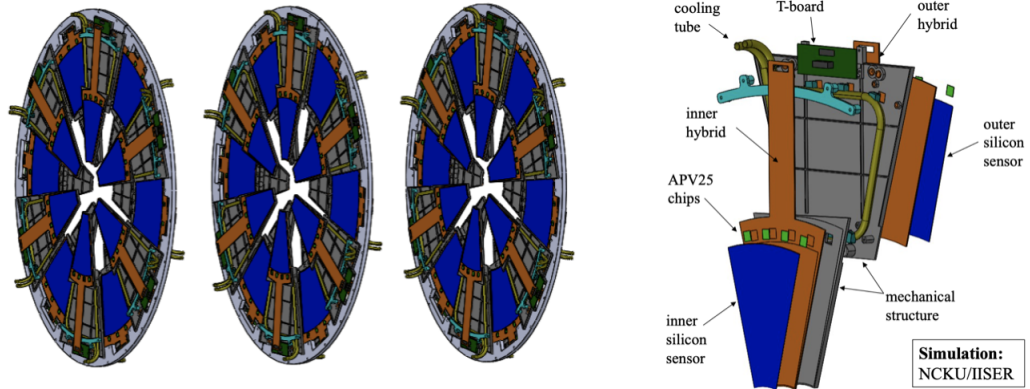


Figure 5.5: Module design of STAR’s Forward Silicon Tracker with its three silicon discs [178].

the slow control software ensured minimal intervention and oversight by the shift crew, underscoring the robustness and reliability of the detector’s operational framework.

5.2.1.2 small-strip Thin Gap Chambers

The right panel of Fig. 5.6 illustrates the layout of an sTGC chamber. It comprises a gold-plated tungsten anode wire plane and two cathode planes. The anode plane consists of 340 wires pitched at 1.8 mm intervals, each wire measuring $50 \mu\text{m}$ in diameter. These wires are positioned between the two cathode planes. The cathode planes are composed of 1.5 mm thick FR4 board and copper strips (pads). On one side of the cathode plane, copper strips are arranged perpendicular to the wires to facilitate accurate coordinate measurements. Conversely, copper pads are present on the opposite side of the cathode plane. These copper strips, spaced at intervals of 3.2 mm, function as readout electrodes and are meticulously designed to achieve excellent position resolution, reaching as fine as $100 \mu\text{m}$. Furthermore, both cathode planes are coated with a high-resistance graphite-epoxy mixture to enhance their performance. The sTGC setup at STAR Forward Upgrade comprises four identical planes, each featuring four pentagonal-shaped gas chambers with double-sided and diagonal strips providing x, y, and z coordinates in each plane. Constructed at Shandong University in China, sixteen chambers and approximately five spare chambers were produced. A custom-designed aluminum frame facilitated integration within the pole-tip of the STAR magnet and around the beam pipe on the west side of STAR. The schematic diagram shown in Figure 5.6 (left panel) shows four sTGCs at distances of 307 cm, 325 cm, 343 cm, and 361 cm from the interaction points, respectively.

Operated with a quenching gas mixture of n-Pentane and CO_2 (45%:55% by volume) at a typical high voltage of 2900 V, the sTGC chambers functioned in a high amplification

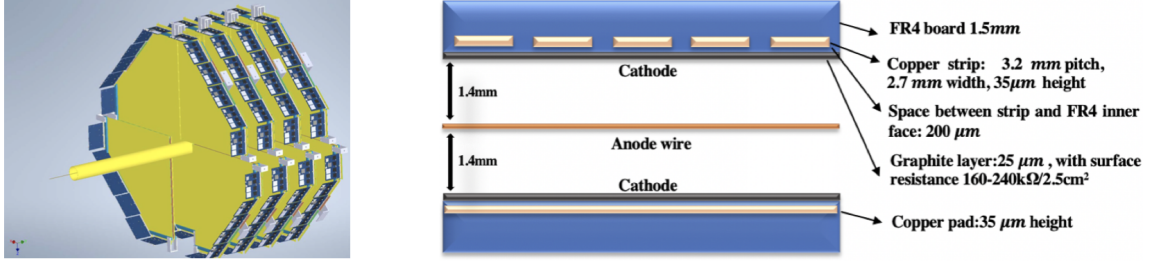


Figure 5.6: On the left panel, a set of four pentagon-shaped sTGCs is shown, while the right panel displays the layout of a sTGC chamber.

mode. Installation occurred before Run-22, and commissioning took place in the initial weeks of the run. The high voltage operating point was fine-tuned for optimal efficiency, with stable operation and acceptable leakage current even under high luminosity.

An in-house-designed gas system, responsible for mixing and delivering the gas along a long-heated path to the chambers, met operational requirements and performed exceptionally well during Run-22.

5.2.2 Forward Calorimeter System

The STAR FCS aims to explore QCD physics across a broad spectrum of Bjorken x values, focusing particularly on the extremities of high and low regions. Previous efforts using detectors like the Forward Pion Detector (FPD) and Forward Meson Spectrometer (FMS), along with recent enhancements such as a refurbished FMS and new pre-shower and post-shower detectors, have highlighted significant QCD physics prospects in the forward domain. To surpass current achievements, the current FCS outlines a forward detector upgrade boasting improved detection capabilities for neutral pions, photons, electrons, jets, and leading hadrons within a range of pseudo-rapidity from 2.5 to 4. This forward upgrade not only facilitates the study of longitudinal structures in the initial state, relevant to the breakdown of boost invariance in heavy ion collisions but also enables exploration of the transport properties of hot and dense matter, particularly near regions of perfect fluidity.

FCS is composed of two vital components: the ElectroMagnetic Calorimeter, featuring 1486 towers, and the Hadronic Calorimeter, consisting of 520 towers. The integration and calibration of all SiPM sensors, front-end electronics boards, and the readout & triggering boards known as DEP were meticulously carried out during Run-21. The FCS comprises a Spaghetti ElectroMagnetic Calorimeter (SPACal) followed by a Lead and Scintillating Plate sampling Hadronic Calorimeter (HCal), with the SPACal exhibiting exceptional density and compactness. Incorporating the PHENIX ECal as a cost-effective alternative, albeit with a slight compromise in compensation, ensures seamless integration

with minimal dead zones between the ECal and HCal. Wavelength-shifting slats facilitate light collection from the HCal scintillating plates, detected by photon sensors at the end of the HCal, with both calorimeters sharing the same cost-effective readout electronics and photo-sensors.

Before the commencement of Run-22, signal splitter boards for the west EPD detector were installed, and the west EPD was utilized as a pre-shower detector in electron triggers. Figure 5.7 illustrates a diagram of the FCS.

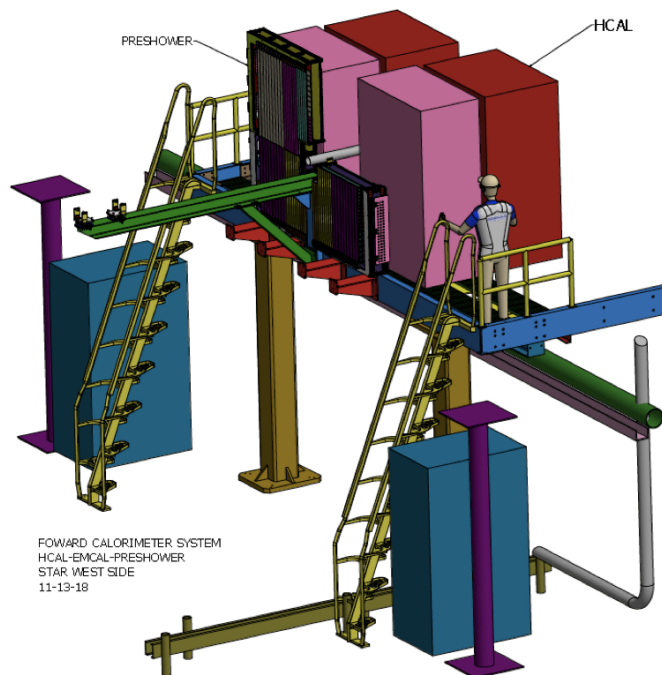


Figure 5.7: A 3D CAD representation of the FCS within the STAR detector model [172].

5.3 Details of Tracking Algorithm

In any high-energy physics experiment, it is very important to estimate the kinetic properties of particles that are produced during a collision as accurately as possible. These properties include the position, direction, and momentum of the particles at the point where they are created. To achieve this accuracy, a group of highly sensitive detectors is placed near the area where the particle beams collide. When charged particles are produced in the collision, they travel through these detectors and ionize the detector material, which allows multiple precise measurements of their position along their paths. It is important that these detectors do not significantly alter the paths of the particles. Therefore, the detectors should be designed with as little material as possible to minimize any disturbance to the particles' trajectories. Accurately determining the kinematic variables of high-energy particles as they move through different parts of the detector is

crucial. Therefore, the process of track reconstruction is very important and discussed in the following section.

5.3.1 Track reconstruction

Track reconstruction is one fundamental part of the event reconstruction in high energy physics experiments. In a simplified view, it can be divided into the procedure of finding track candidates, the pattern recognition, and the estimation of the parameters that describe the particle trajectory, the track fit. A charged particle, when traversing through the detector, leaves a trace through electronic signals (hits) on sensitive detector elements. In pattern recognition, the collection of hits has to be found that has been caused by one single particle. Misidentified hits (in the following called fake hits) need to be avoided, since they usually decrease the final track resolution or may even lead to wrong track signatures and consequently sometimes to a wrong particle identification. The collection of hits are then further processed in the track fitting to estimate the associate trajectory parameters. In the track fit, some level of discrimination can be applied that helps to eliminate or flag fake hits by their unproportional contribution to fit quality measures, such as the χ^2 of the fit. A relatively clean input sample provided by the pattern recognition that is characterised by high efficiency while containing only few ghost tracks is, however, required not only for an optimisation of the computing time, but also for the stability of track fitting process. The objective of the FST simulation is to check the tracking performance of the forward silicon tracker. The key steps of track finding and track fitting are discussed in the following section.

- **Track finding:** The quality assessment of a track reconstruction application relies on two key parameters: the track reconstruction efficiency and the resolution of track parameters. These parameters, traditionally, correspond to the distinct tasks of track finding and track fitting, with the latter elaborated upon in next Section. The track finder takes as input a list of hits either within selected regions or across the entire detector. Its objective is to identify hits associated with a specific particle, grouping them into subsets. Each subset contains hits belonging to the trajectory of a single particle, and the total number of subsets aligns with the count of particles passing through the detector.

- **Track fitting:**

Track fitting involves estimating track parameters based on a given set of measurements. These measurements inherently carry uncertainty arising from detector resolution and positioning uncertainties due to misalignment. Additionally, a track model needs to be defined, typically derived from the solution of the transport equation in the detector setup. While analytical track models suffice in ideal scenarios

(e.g., absence of magnetic field or in a homogeneous magnetic field), for the magnetic field configuration of the STAR experiment, numerical methods are essential. Considering successive interactions with detector material, the track fit must incorporate these effects. Conceptually, the track fit combines the detector geometry, measurements, and algorithmic modules for parameter transport through the magnetic field setup. The track fitting procedure aims to determine the parameters of the curve that describe the trajectory. It takes as input the positions of all hits within a subset identified by the track finder. The output is a list of particles, each represented by an estimate of the corresponding track parameters.

For track finding, the Cellular Automata (CA) algorithm is used, and for track fitting, GENFIT2 is used. CA is a computational paradigm used in particle tracking, inspired by the concept of discrete elements proposed by Leucippus and Democritus around 450 BC. It simulates a discrete dynamical system where the evolution is governed by local interactions among constituent elements represented as a grid of cells. In the context of particle tracking, a CA-based approach models the propagation of particle trajectories through a detector system. The detector is represented as a grid of cells, with each cell corresponding to a discrete volume element. The state of each cell represents whether a particle is present or absent within that volume element at a given time step. The evolution of the CA system is determined by fixed rules that define how the state of each cell changes over successive time steps based on the states of neighboring cells. These rules capture the physics of particle interactions with the detector material and the propagation of particle trajectories through the detector. One of the key advantages of CA-based approaches for particle tracking is their ability to handle complex detector geometries and large combinatorial challenges associated with high track densities. CA algorithms can efficiently explore the combinatorial space of possible particle trajectories and identify likely track candidates based on local interactions within the detector. The cellular automaton method [179] forms short track segments, known as tracklets, within neighboring detector planes, and then connects them to create complete tracks as shown in Fig. 5.8. Cellular automata, which are fundamentally local and parallel, manage to avoid the necessity for exhaustive combinatorial searches, even when used on regular computers. Due to the structured nature of information processed by cellular automata, there is a notable reduction in the volume of data to be handled during the track search. Cellular automata typically utilize a simple track model, ensuring computational simplicity and a rapid algorithm.

After track finding, the detector measurements are grouped into sets of hits, ideally corresponding to specific particles. Track fitting then becomes essential for estimating track parameters and their uncertainties, enabling the determination of particles' kinematic properties. This information is crucial for reconstructing short-lived particles and

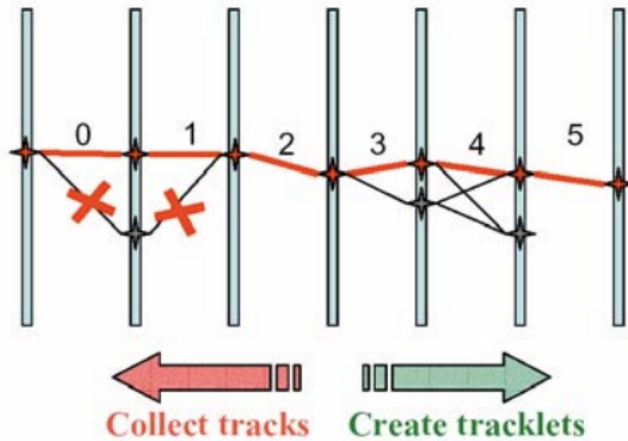


Figure 5.8: A basic representation of the cellular automaton algorithm: generating tracklets, linking and numbering them based on potential trajectory alignment, and then grouping tracklets into track candidates [180].

conducting physics analysis. Typically, track fitting algorithms rely on a track model, representing the theoretical motion equation for charged particles within the tracking detector volume. However, certain factors such as multiple scattering, ionization, and radiative energy loss affect particle motion, introducing perturbations that influence the reconstruction of particle kinematics. Proper track fitting methods account for these effects, with the Kalman filter method being the most common algorithm in high-energy physics (HEP) applications. Although track parameters can theoretically be derived from hit measurements using least squares fitting, the Kalman filter method is preferred in practical scenarios. Its recursive nature allows for computationally simpler and numerically optimized implementation. Unlike the least squares fit, which operates with matrices whose dimension equals the number of measurements in the track, the Kalman filter method works with matrices of dimensionality equal to the number of fitted parameters. The Kalman filter method offers several advantages:

- It provides an optimal estimate with minimal dispersion, ensuring unbiased results.
- Its recursive nature enables fitting of partially reconstructed tracks during track finding.
- It does not require a global track model valid for the entire track length but utilizes a local track model valid only between consecutive measurements.

Genfit2 [181] is a track-fitting tool that is used in particle physics experiments for reconstructing particle trajectories based on detector signals. It is based on Kalman filter algorithm. Genfit2 works by combining measured hits from different tracking subdetectors and fitting them to create track candidates. It also allows for the refinement of tracks

by adding missing hits and performing vertex finding and fitting. The process of track fitting in GENFIT 2 starts with the collection of measured hits from the detector. These hits are associated with a track candidate, which is then fitted using the measurements and track representations. The fitting algorithms in GENFIT 2 use the measurements and track representations to calculate the trajectory of the particle and refine the track by adding missing hits and gathering information from different tracking subdetectors. The final track is obtained by combining trajectories pointing to the same origin through vertex finding and fitting [182].

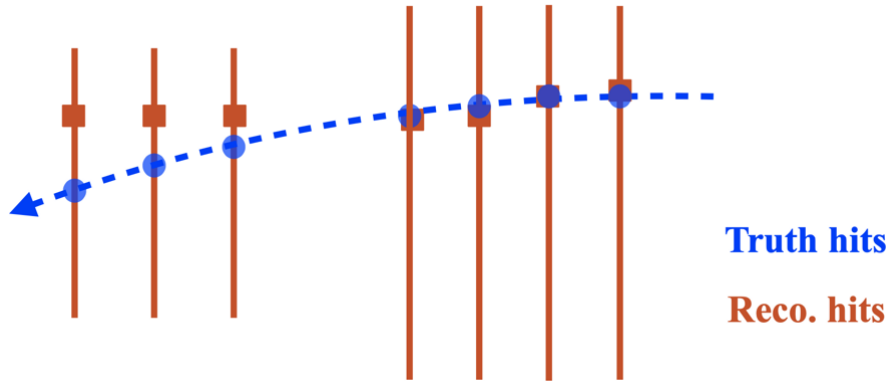


Figure 5.9: Schematic of MC track passing through 3 Si and four sTGC. MC (Truth) and Reconstructed (Reco.) hits are shown.

Once we have successfully reconstructed the particle track using the methods discussed previously, the next step is to calculate the tracking efficiency. The tracking efficiency is calculated by the ratio of the reconstructed tracks (N_{reco}) (i.e., obeys the same selection criteria as applied to the real data) to the Monte Carlo truth tracks (N_{truth}).

$$\text{Tracking Efficiency} = \frac{N_{reco}}{N_{truth}} \quad (5.1)$$

Figure 5.9 illustrates the truth hits (in blue) and the reconstructed hits (in red) as a simulated Monte Carlo (MC) track, under the presence of a magnetic field, passes through three silicon detectors and four small-strip Thin Gap Chambers.

5.4 Analysis Method

The entire simulation process is summarized in the flowchart as shown in Fig. 5.10. Each step in the flowchart is crucial for understanding and processing the data collected from particle interactions. Below is an expanded explanation of each step:

1. **Generator** In the initial step of our simulation, we generate particle tracks using various event generators, as given below.

- **Single Particle Gun:** This generates single particles such as π^+/π^- with varying energies (0.2, 1.0, 2.0 GeV) and different particle counts (1-300 particles). This step is essential for studying the basic interactions of individual particles.
- **PYTHIA:** Used to generate 250k minimum bias (MB) events, focusing on primary particles. PYTHIA is a well-established tool for simulating high-energy physics events, providing a broad spectrum of particle interactions.
- **HIJING:** Generated 25k minimum bias events, concentrating on primary particles. HIJING is particularly valuable for simulating heavy-ion collisions, offering insights into complex particle dynamics.

2. Detector Simulation (GEANT)

GEANT is utilized to simulate the passage of generated particles through the detector material. This step involves detailed modeling of how particles interact with the detector, providing realistic data for further analysis. We pass the tracks generated by the event generator through GEANT to obtain the hit information. Different configurations of the detector elements (Silicon layers and sTGCs) are tested to understand their performance.

3. Track Reconstruction

- **Reconstruct Hit:** The hits recorded by the detector are reconstructed into tracks, allowing for the determination of particle trajectories.
- **Enlarge Hit Errors:** The hit errors are enlarged by a factor of $\frac{1}{\sqrt{12}}$. This adjustment simulates a condition where the detector resolution is not perfect or to account for uncertainties.

4. Final Step

- **Tracking Codes:** The final tracking analysis is performed using codes. These codes likely contain algorithms for refining track reconstruction and applying further corrections.

The summarized steps are presented in the flowchart below:

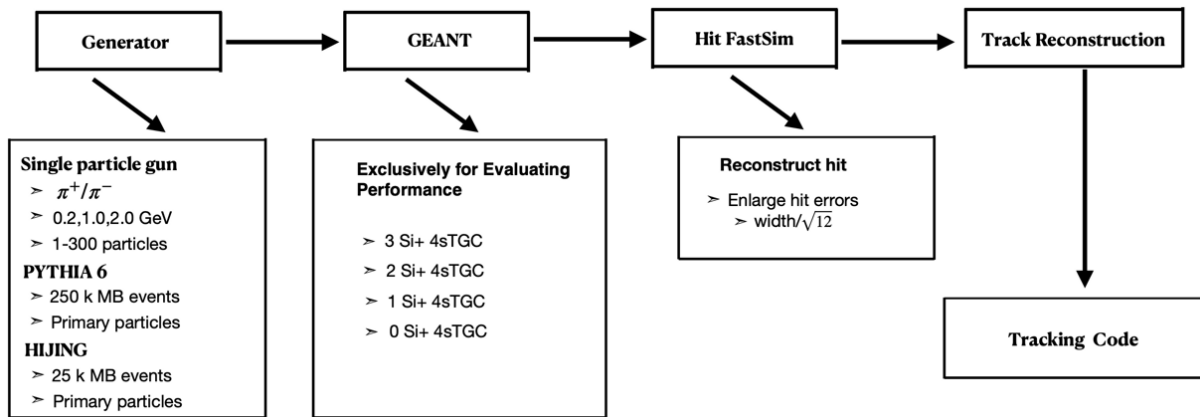


Figure 5.10: Flowchart summarizing the simulation and analysis pipeline.

5.5 Results and Discussion

5.5.1 Position Resolution Study

In the initial phase of our simulation work, we have conducted a detailed analysis to generate and reconstruct muon tracks under specific conditions and evaluate the tracking efficiency. We used silicon discs with 8 uniform radial segments ranging from 5.0 cm (inner radius) to 28.0 cm (outer radius) and 12x128 azimuthal segments covering 2π radians. The analysis was carried out as follows:

1. Use a single particle gun to simulate events with a track density of 5 tracks per event, for a total of 1000 events.
2. Generate muon tracks within the pseudorapidity (η) range of 2.5-4.0 and transverse momentum (p_T) range of 0.2-5.0 GeV/c.
3. Pass the generated tracks through the GEANT simulation for different combinations (Si and sTGCs layers) and position resolutions of silicon discs.
4. Use tracking code to reconstruct tracks from hits obtained from GEANT.
5. Calculate the tracking efficiency as a function of η .

In this part of the simulation, we systematically assessed the efficiency of the forward tracking system by varying the position resolution of the silicon discs. The objective was to observe how the efficiency of track reconstruction evolves with changes in the position resolution. Commencing with a resolution of $1 \mu\text{m}$, we incrementally increased it up to $100 \mu\text{m}$, analyzing its impact on efficiency across different η values.

In the specific case of utilizing only 3 Silicon disks, our investigation into efficiency as a function of η and varying blur in the X and Y directions (σ_X and σ_Y) yields insightful observations as shown in Fig. 5.11.

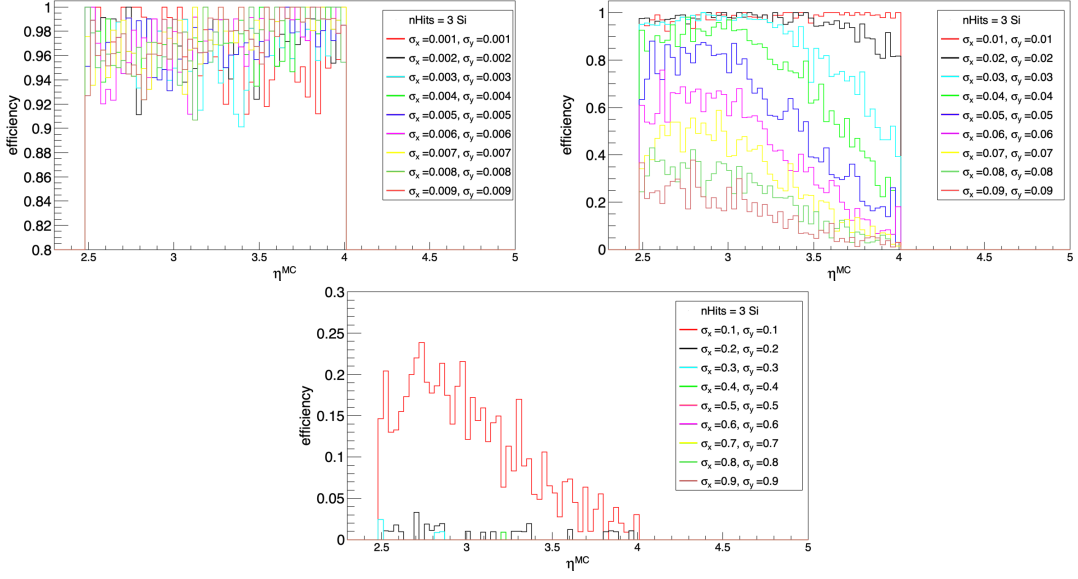


Figure 5.11: Tracking efficiency with 3 silicon disks and no sTGC layers. σ_X and σ_Y values are given in mm.

Within the range of σ_X and σ_Y values from 1 to 9 μm , a consistent and unvarying efficiency as a function of η . This suggests a stable and reliable track reconstruction performance within this lower range of blur values. As we extend the σ_X and σ_Y values to the range of 10 to 90 μm , a clear decrease in efficiency is observed. The reduction in efficiency within this moderate range indicates that, with an increase in the blur in the X and Y directions, the precision of track reconstruction experiences a noticeable decline. Furthermore, an important observation occurs when the σ_X and σ_Y values surpass 100 μm . The efficiency exhibits a sharp decline in this higher range, approaching almost zero. This significant decrease implies a critical threshold beyond which the track reconstruction efficiency is severely compromised. The decreasing efficiency at higher σ_X and σ_Y values highlights how sensitive the system is to increased position uncertainties. This could make it harder to accurately track particle paths, especially when there are only three Silicon disks available.

Furthermore, we included hits from the sTGC detector to investigate the system's performance comprehensively. Specifically, we expanded the scenario from 3 Si disks to 7 hits (comprising 3 Si disks and 4 sTGC hits). These variations in hit configurations are illustrated in Figure 5.12, providing insights into the interplay between position resolution, hit count, and track reconstruction efficiency.

In both cases, using 7 hits (3 Si + 4 sTGC) and only 3 Silicon disks, we observed similar patterns in efficiency as a function of η under varying blur values in the X and Y directions (σ_X and σ_Y). For σ_X and σ_Y values within the range of 1 to 9 μm , the efficiency remains consistent and stable across different η values, indicating reliable track

reconstruction performance in both configurations.

As σ_X and σ_Y increase to the range of 10 to 90 μm , we observe a gradual decrease in efficiency with increasing η . This suggests that as the blur in the X and Y directions grows, the track reconstruction efficiency begins to decline in a similar manner for both scenarios.

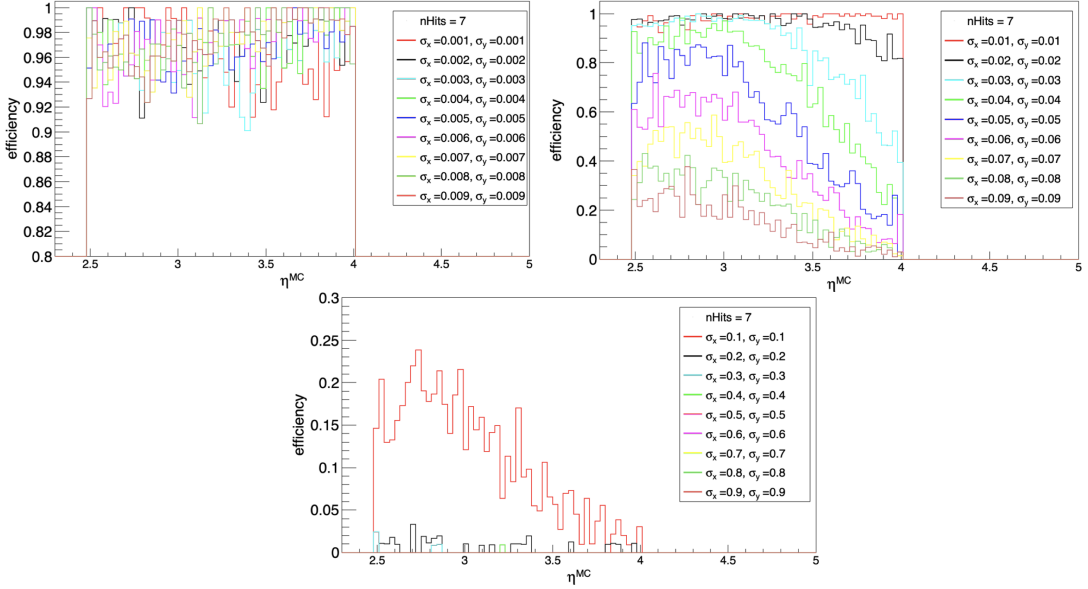


Figure 5.12: Tracking efficiency with 3 silicon disks and 4 sTGC layers. σ_X and σ_Y values are given in mm.

When σ_X and σ_Y exceed 100 μm , the efficiency drops sharply, approaching nearly zero. This step decline marks a critical threshold beyond which track reconstruction becomes significantly less precise. The reduced efficiency at higher blur values highlights the system's sensitivity to increased position uncertainties, making accurate particle path reconstruction more challenging. These results are summarized in Fig. 5.13.

The findings reveal that the system's performance is similarly affected by position resolution in both configurations.

5.5.2 Tracking Efficiency

In the next part of our simulation, we are looking at tracking efficiency 4 sTGC hits, using STARSIM as the tool for creating events.

The analysis is conducted through the following steps:

1. Use STAR simulator to generate 1 μ^\pm /event.
2. Generate muon tracks within the pseudorapidity (η) range of 2.45-4.05 and transverse momentum (p_T) range of 0.2-2.0 GeV/c.

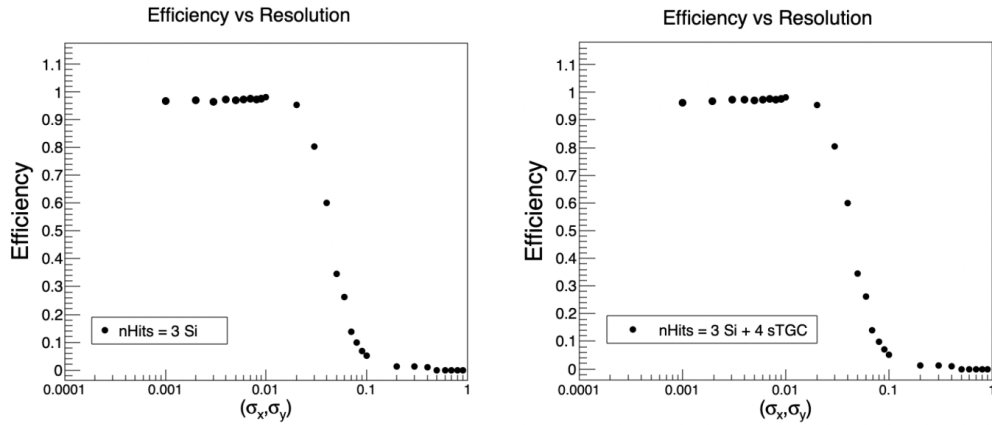


Figure 5.13: Summary plot for position resolution study.

3. Pass the generated tracks through the GEANT simulation.
4. Use tracking code to reconstruct tracks from hits obtained from GEANT.
5. Calculate the tracking efficiency as a function of η , ϕ , and p_T .
6. Finally, calculate momentum and inverse momentum resolution.

There are different possibilities for finding hits, as shown in the quality plot in Fig. 5.14. We can see that we get almost 93% track with 4/4 hits while a small fraction, 6% track with 3/4 hits.

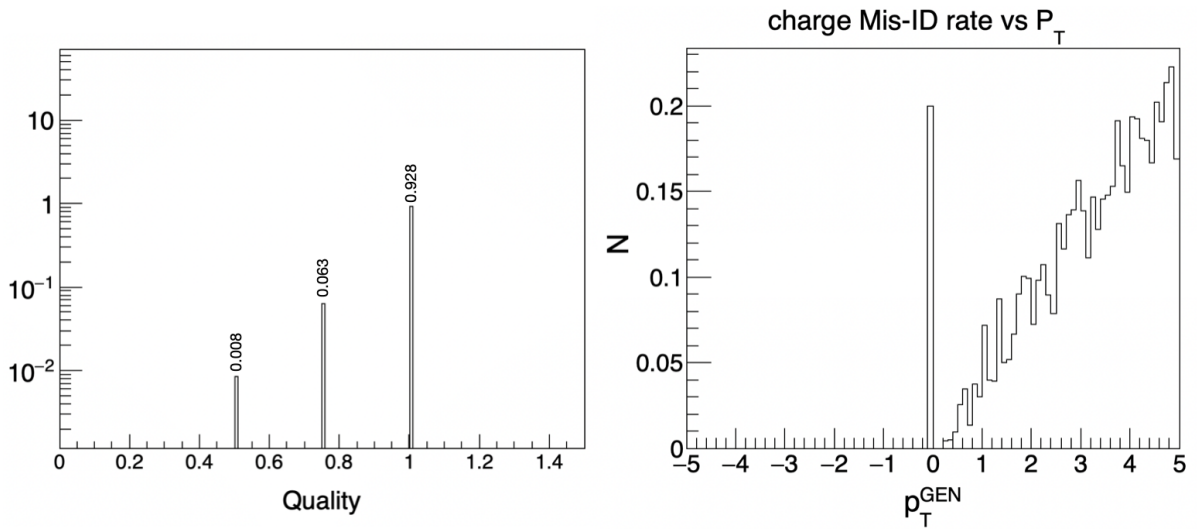


Figure 5.14: QA plots for tracking using four sTGC hits

When we require all four hits to be present, we find a tracking efficiency of about 95% as a function of η , ϕ , and p_T , indicating that our tracking method is effective at identifying and reconstructing tracks in the simulated events as shown in Fig. 5.15.

However, when we consider all possible combinations of hits, rather than just the four hits together, we observe a slightly higher efficiency as a function of η , ϕ , and p_T . These findings are illustrated in Figure 5.15. The momentum resolution is 39%, indicating the precision in determining particle momentum. The inverse momentum resolution is 46%. In the subsequent phase of our study, we evaluate the tracking efficiency, explicitly focusing on the detection and reconstruction of tracks associated with four sTGC hits. The events are generated using the PYTHIA event generator, and the comprehensive steps for this analysis are detailed below.

1. Use the PYTHIA 8 event generator to simulate p+p collisions at $\sqrt{s} = 510\text{GeV}$, generating 5,000 events
2. Generate charged particle tracks within the η range of 2.45-4.05 and p_T range of 0.2-2.0 GeV/c.
3. Pass the generated tracks through the GEANT simulation.
4. Use tracking code to reconstruct tracks from hits obtained from GEANT.
5. Calculate the tracking efficiency as a function of η , ϕ , and p_T .
6. Calculate momentum and inverse momentum resolution and check the effect of including Si hits with sTGC hits on efficiency.

When we require all four hits to be present, we find a tracking efficiency of about 90% as a function of η , ϕ , and p_T , indicating that our tracking method is effective at identifying and reconstructing tracks in the simulated events using the PYTHIA 8 event generator. Figure 5.16 tracking efficiency as a function of η , ϕ , and p_T using the PYTHIA 8. Without including the Si hits in refitting, the momentum resolution is 32%, and the inverse momentum resolution is 40% in this case.

In the next part of our study, momentum and inverse momentum resolution analysis were conducted with and without the Silicon refit. In this study, we calculated the tracking across different radii segments of the Silicon discs, specifically at 0.2 cm, 0.3 cm, 0.4 cm, 0.6 cm, 0.8 cm, 1.0 cm, 1.25 cm, 1.5 cm, 1.75 cm, 2.0 cm, 2.25 cm, and 2.75 cm. The primary vertex σ_{XY} resolution was fixed to 0.02 mm, and the analysis involved 128×12 divisions in the azimuthal angle.

Without the silicon refit, the momentum resolution and inverse momentum resolution are approximately 32% and 40%, respectively, as shown in the Fig. 5.17. By applying the Silicon refit, we observed a significant improvement: the momentum resolution improved to approximately 24%, and the inverse momentum resolution decreased to around 28%. The study also indicates that the momentum and inverse momentum measurements remain consistent as the radius of the Silicon discs increases as shown in Fig. 5.18.

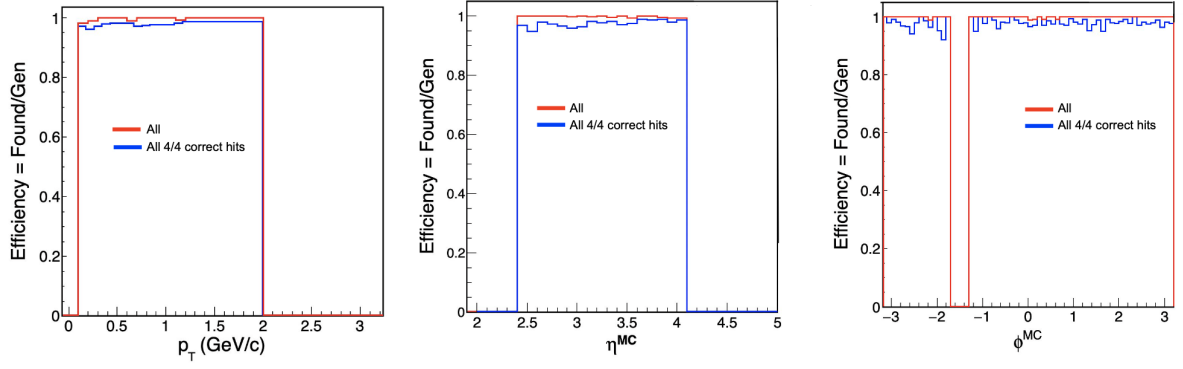


Figure 5.15: Tracking efficiency of sTGCs as a function of p_T , η , and ϕ using the STAR simulator (STAR SIM).

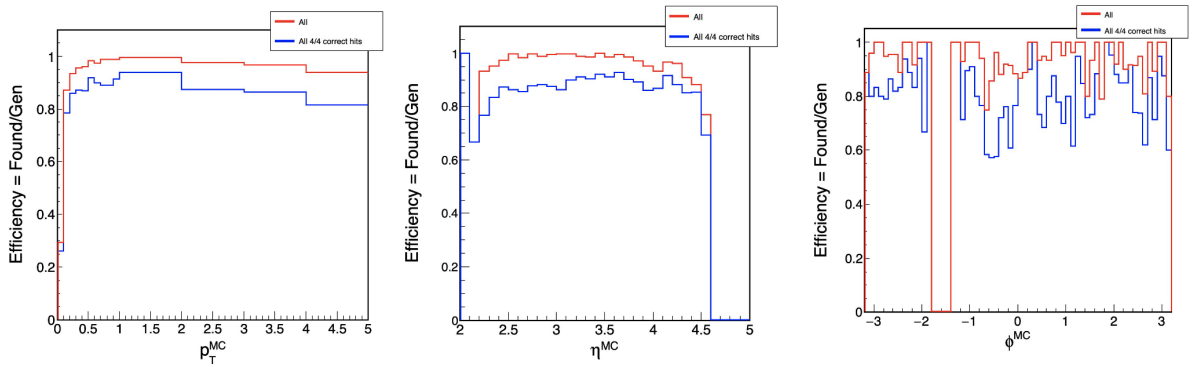


Figure 5.16: Tracking efficiency of sTGCs as a function of p_T , η , and ϕ using the PYTHIA8.

In the next part of our study, momentum and inverse momentum resolution were analyzed as functions of the primary vertex σ_{PV} resolution, with the Silicon disc radius fixed at 0.2 cm. In this study, we evaluated resolutions for σ_{PV} values of 0.02 mm, 0.04 mm, 0.06 mm, 0.1 mm, 0.4 mm, 0.8 mm, and 1.0 mm. The results showed that the momentum resolution remained nearly constant across the primary vertex resolutions. In contrast, the inverse momentum resolution increased significantly and saturated with the primary vertex σ_{PV} resolution beyond 0.2 mm as shown in Fig. 5.19.

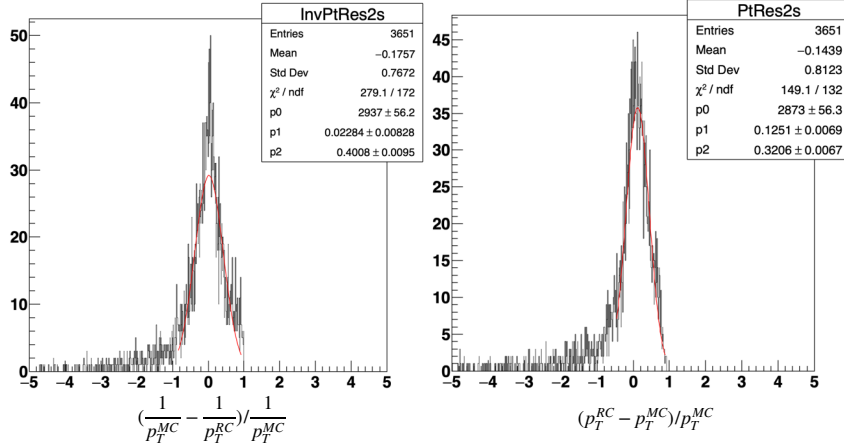


Figure 5.17: Momentum ($\sigma(p_T)$) and inverse momentum ($\sigma(1/p_T)$) resolution.

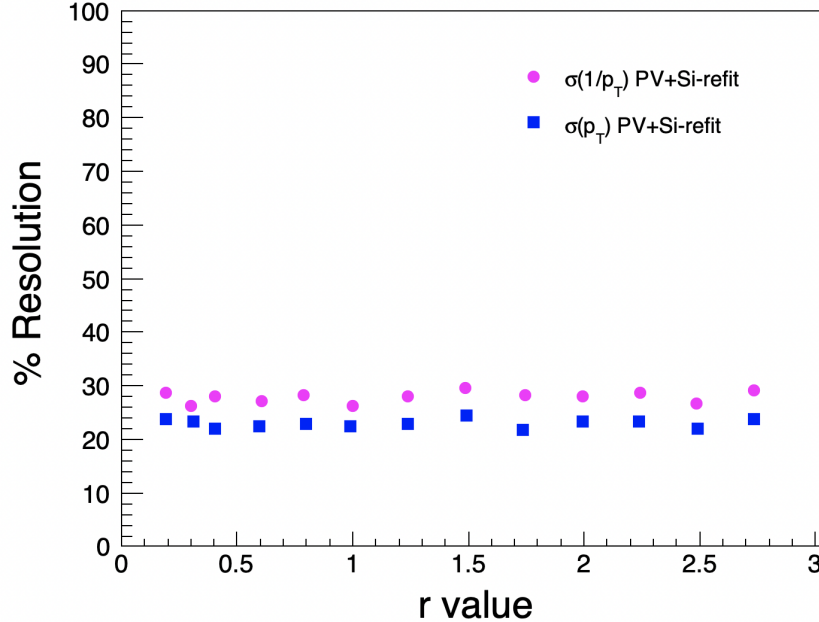


Figure 5.18: Momentum ($\sigma(p_T)$) and inverse momentum ($\sigma(1/p_T)$) resolution as a function of radius values of Silicon discs.

In the last part of our study, we studied the effect of changing the z-location of silicon discs and building the geometry. The analysis steps are as follows:

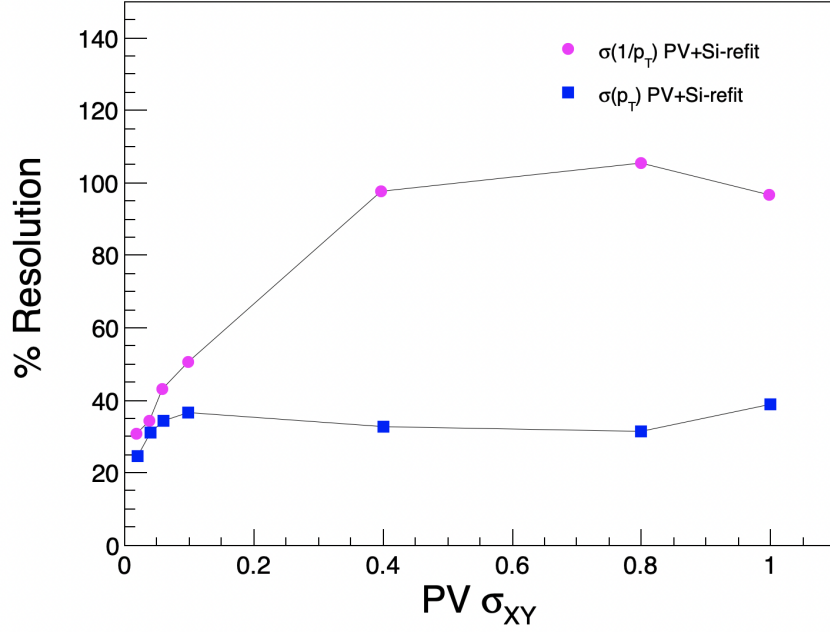


Figure 5.19: Momentum ($\sigma(p_T)$) and inverse momentum ($\sigma(1/p_T)$) resolution as a function of primary vertex resolution.

1. Generate MC events using STAR Simulator where 1 μ^+ per event is generated with $2.45 < \eta < 4.05$ and $0.2 < p_T < 2 \text{ GeV}/c$.
2. Default Z location for three silicon discs is taken as 154.48, 177.98, and 201.47 cm.
3. Modify Geometry (z location of Silicon discs) in GEANT.
4. Rebuild geometry and generate simulation.
5. Find z-position of GEANT hit for 3 Si discs.

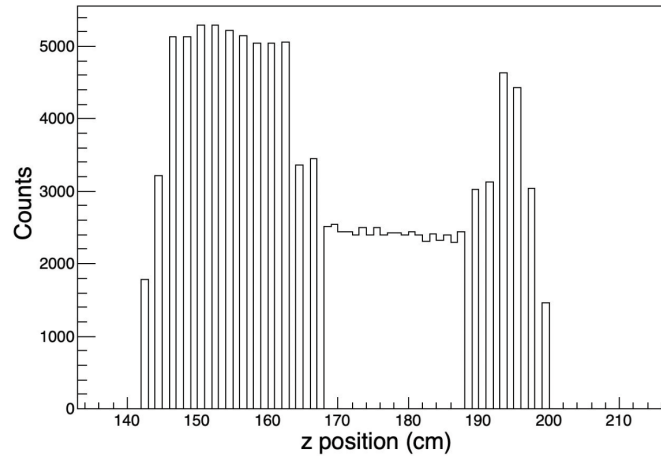


Figure 5.20: combined Z-distribution of Si discs.

Each of the three silicon discs undergoes simultaneous displacement in the forward and backward directions in five distinct steps, each spanning a distance of 2 cm. Subsequently, the geometry is reconstructed, and events are generated to analyze the impact of these positional adjustments. The GEANT hit positions are determined along the z -axis using the existing geometry. It is important to note that the hit positions become constrained to zero after reaching a distance of 200 cm, reflecting limitations imposed by the global geometry configuration as shown in Fig. 5.20. This iterative exploration of disc movements allows for a comprehensive understanding of how alterations in disc positions influence the simulated events while considering the constraints dictated by the overall geometry.

5.6 Summary

The integration of the FCS and FTS, including the FST and sTGC, can significantly improve particle detection capabilities across a wide forward rapidity range ($2.4 < \eta < 4.1$). Our study comprehensively evaluated the tracking efficiency, momentum resolution, and inverse momentum resolution of the FTS under various conditions using detailed simulations.

Tracking efficiency was assessed by varying the positional resolution of the silicon disks, ranging from 1 to 100 μm . The system maintained robust performance with an efficiency of approximately 90% when four hits were required to be present across η , p_T , and ϕ . The tracking method proved effective, though efficiency began to decline sharply as positional uncertainties exceeded 10 μm , nearing zero beyond 100 μm . This result underscores the sensitivity of the tracking system to positional uncertainties, particularly at higher blur levels.

Using STAR simulator, we found that when all four sTGC hits are required, the tracking efficiency is approximately 95% as a function of η , ϕ , and p_T . The momentum resolution was 39% while the inverse momentum resolution was 46%. Using PYTHIA 8 event generator, we observed a tracking efficiency of approximately 90% under the same conditions, with all four sTGC hits present. This demonstrates that our tracking method remains effective even in more complex multi-particle scenarios. However, without including the Silicon hits in the refitting process, the momentum resolution was reduced to 32%, and the inverse momentum resolution was approximately 40%, highlighting the importance of including Silicon hits for improved accuracy in momentum measurements.

In the next part of our study, we analyzed the momentum and inverse momentum resolutions with and without the Silicon refit across various radii segments of the Silicon discs, ranging from 0.2 cm to 2.75 cm. The primary vertex σ_{PV} resolution was fixed at 0.02 mm, and we divided the azimuthal angle into 128×12 segments for detailed

tracking analysis. By applying the Silicon refit, we observed a significant improvement: momentum resolution improved to approximately 24%, and inverse momentum resolution decreased to around 28%. Importantly, these improvements remained consistent as the radius of the Silicon discs increased.

Additionally, we explored the effect of varying the primary vertex σ_{PV} resolution on momentum and inverse momentum resolution, keeping the Silicon disc radius fixed at 0.2 cm. The study showed that momentum resolution remained stable across different σ_{PV} values, while the inverse momentum resolution increased significantly and eventually saturated when σ_{PV} exceeded 0.2 mm. This indicates that inverse momentum resolution is sensitive to the primary vertex resolution, particularly at lower values.

In the final part of our study, we examined the effect of shifting the z -locations of the three silicon discs from their default positions (154.48 cm, 177.98 cm, and 201.47 cm) forward and backward in steps of 2 cm. After modifying and rebuilding the geometry in GEANT, we analyzed the z -positions of GEANT hits for the silicon discs. The results showed that when the discs were moved beyond 200 cm, the hit positions became constrained to zero due to limitations in the global geometry. This study helped us to understand that shifting the silicon discs too far in the z -direction leads to the hit positions becoming constrained due to limitations in the global geometry.

Chapter 6

Conclusion

This thesis focuses on a detailed study of the bulk properties of the medium produced in Au+Au collisions at $\sqrt{s_{NN}} = 54.4$ GeV using identified hadron spectra measurements from the STAR experiment. This is followed by an analysis of particle production mechanisms across various energies using the AMPT model. Additionally, the thesis includes a performance study of the Forward Tracking System at STAR.

The first part of the thesis delves into the detailed study of various observables related to identified particle production in Au+Au collisions at $\sqrt{s_{NN}} = 54.4$, GeV. These observables include the p_T -spectra of π^\pm , K^\pm , and $p(\bar{p})$ in mid-rapidity ($|y| < 0.1$), measured across nine centrality classes (0-5%, 5-10%, ..., 70-80%). Observables such as average transverse momentum ($\langle p_T \rangle$), particle yields (dN/dy), particle ratios, and kinetic freeze-out properties are shown as functions of energy and collision centrality. These results are compared with corresponding findings from BES-I energies at $\sqrt{s_{NN}} = 7.7$ to 39, GeV, as well as higher energy results from STAR in Au+Au collisions at $\sqrt{s_{NN}} = 62.4$ and 200 GeV.

The $\langle p_T \rangle$ values for π , K , and p increase from peripheral to central collisions in Au+Au collisions at $\sqrt{s_{NN}} = 54.4$ GeV, indicating a growing radial flow effect in more central collisions. This rise in $\langle p_T \rangle$ from π to K and then to p suggests an increase in radial flow with the particle mass. The integrated particle yields dN/dy in mid-rapidity ($|y| < 0.1$) of π^\pm , K^\pm , and p do not scale with $\langle N_{\text{part}} \rangle$; rather, they slowly increase from peripheral to central collisions in Au+Au collisions at $\sqrt{s_{NN}} = 54.4$ GeV. However, it does not show a strong centrality dependence for \bar{p} . For energy dependence, the dN/dy for π^\pm , K^\pm , p , and \bar{p} increases as collision energy rises, whereas for protons (p), it decreases with increasing energy. This behavior of p is directly influenced by baryon stopping at lower RHIC energies.

The π^-/π^+ ratio exhibits a weak centrality dependence, indicating a consistent pion production mechanism across different collision regions. The flat K^-/K^+ ratio suggests similar production mechanisms and collective flow for kaons regardless of centrality, con-

sistent with lower-energy observations. The \bar{p}/p ratio increases from central to peripheral collisions, reflecting the greater proton-antiproton annihilation and baryon stopping in central collisions compared to peripheral ones at RHIC energies. The particle ratios K^+/π^+ and K^-/π^- rise from peripheral to mid-central collisions and then level off with $\langle N_{\text{part}} \rangle$, reflecting strangeness equilibrium as the system transitions from a canonical to grand-canonical description. This behavior, also influenced by baryon stopping, is consistent with observations at other RHIC energies. The \bar{p}/π^- ratio remains constant across different centralities, showing no significant dependence on net-baryon density. The p/π^+ ratio increases with centrality at lower RHIC energies but stabilizes at higher energies, following the trend observed in 62.4 and 200 GeV collisions.

For energy dependence, the π^-/π^+ ratio, initially greater than one at lower energies, approaches unity as beam energy increases, indicating the growing dominance of pair production over resonance decays. The K^-/K^+ ratio also increases with collision energy and nears unity. This is due to a shift from associated production, which mainly creates K^+ , to pair production, which generates equal amounts of K^+ and K^- , as energy rises. The \bar{p}/p ratio increases with $\sqrt{s_{NN}}$, approaching unity at higher energies, reflecting a decrease in net baryon density.

Kinetic freeze-out parameters are obtained from a simultaneous blast-wave fit to π^\pm , K^\pm , and $p(\bar{p})$ spectra in Au+Au collisions at $\sqrt{s_{NN}} = 54.4$ GeV. The kinetic freeze-out temperature T_{kin} decreases from peripheral to central collisions, suggesting a short-lived fireball in peripheral collisions. Conversely, the average flow velocity $\langle \beta \rangle$ increases from peripheral to central collisions, indicating significant radial flow effects in central collisions. This demonstrates an interesting anti-correlation between T_{kin} and $\langle \beta \rangle$.

In the subsequent part of the thesis, we discuss the study of particle production using the AMPT model and compare it with experimental data. Key bulk properties such as particle spectra, integrated yields, average momentum ($\langle m_T \rangle$), as well as freeze-out properties like kinetic temperature (T_{kin}) and flow velocity (β) are analyzed. Data from central Au+Au collisions across a range of center-of-mass energies (7.7 to 200 GeV) are investigated, focusing on particles like π^\pm , K^\pm , p , \bar{p} , K_S^0 , Λ , and ϕ .

Two versions of the AMPT model, Default and String Melting, with distinct parameter sets, are employed and compared with STAR experimental data. The analysis reveals that the spectra of identified hadrons are well-described by specific parameter sets at different energies, notably Set-2 with higher Lund String fragmentation parameter a and higher cross-section value of String Melting version at higher energies and Set-2 of Default version at lower energies. Set-1 of the Default version accurately describes strange hadron spectra across all energy ranges.

Regarding particle ratios, differences in model parameters effectively cancel out, resulting in no energy dependence on input parameters for antiparticle-to-particle ratios.

For p_T integrated yields, Set-2 consistently describes particle yields well across identified hadrons. Set-1 of AMPT-Def model better captures the yields of K_s^0 , Λ , and ϕ .

In terms of mean transverse mass ($\langle m_T \rangle$), there is no specific set that describes all data points for both versions, but an increasing trend similar to data is observed. For kinetic freeze-out parameters, all four sets exhibit similar behavior regarding the centrality dependence of T_{kin} , while none of the parameter sets provide a good description of $\langle \beta \rangle$.

Overall, the kinetic freeze-out parameters T_{kin} decrease with increasing β , consistent with STAR data. There is no single set that distinctly outperforms others in describing all aspects of the data, emphasizing the complexity of the particle production mechanisms and the need for comprehensive modeling approaches.

The final section of the thesis focuses on the forward upgrade at STAR. The integration of the FCS and FTS, including the FST and sTGC, can significantly improve particle detection capabilities across a wide forward rapidity range ($2.4 < \eta < 4.1$). Our study comprehensively evaluated the tracking efficiency, momentum resolution, and inverse momentum resolution of the FTS under various conditions using detailed simulations.

Tracking efficiency was assessed by varying the positional resolution of the silicon disks, ranging from 1 to 100 μm . The system maintained robust performance with an efficiency of approximately 90% when four hits were required to be present across η , p_T , and ϕ . The tracking method proved effective, though efficiency began to decline sharply as positional uncertainties exceeded 10 μm , nearing zero beyond 100 μm . This result underscores the sensitivity of the tracking system to positional uncertainties, particularly at higher blur levels.

Using STAR simulator, we found that when all four sTGC hits are required, the tracking efficiency is approximately 95% as a function of η , ϕ , and p_T . The momentum resolution was 39% while the inverse momentum resolution was 46%. Using PYTHIA 8 event generator, we observed a tracking efficiency of approximately 90% under the same conditions, with all four sTGC hits present. This demonstrates that our tracking method remains effective even in more complex multi-particle scenarios. However, without including the Silicon hits in the refitting process, the momentum resolution was reduced to 32%, and the inverse momentum resolution was approximately 40%, highlighting the importance of including Silicon hits for improved accuracy in momentum measurements.

In the next part of our study, we analyzed the momentum and inverse momentum resolutions with and without the Silicon refit across various radii segments of the Silicon discs, ranging from 0.2 cm to 2.75 cm. The primary vertex σ_{PV} resolution was fixed at 0.02 mm, and we divided the azimuthal angle into 128×12 segments for detailed tracking analysis. By applying the Silicon refit, we observed a significant improvement: momentum resolution improved to approximately 24%, and inverse momentum resolution decreased to around 28%. Importantly, these improvements remained consistent as the

radius of the Silicon discs increased.

Additionally, we explored the effect of varying the primary vertex σ_{PV} resolution on momentum and inverse momentum resolution, keeping the Silicon disc radius fixed at 0.2 cm. The study showed that momentum resolution remained stable across different σ_{PV} values, while the inverse momentum resolution increased significantly and eventually saturated when σ_{PV} exceeded 0.2 mm. This indicates that inverse momentum resolution is sensitive to the primary vertex resolution, particularly at lower values.

In the final part of our study, we examined the effect of shifting the z-locations of the three silicon discs from their default positions (154.48 cm, 177.98 cm, and 201.47 cm) forward and backward in steps of 2 cm. After modifying and rebuilding the geometry in GEANT, we analyzed the z-positions of GEANT hits for the silicon discs. The results showed that when the discs were moved beyond 200 cm, the hit positions became constrained to zero due to limitations in the global geometry. This study helped us to understand that shifting the silicon discs too far in the z-direction leads to the hit positions becoming constrained due to limitations in the global geometry.

The forward upgrade at STAR, with its advanced electromagnetic and hadronic calorimeters and precise tracking detectors, greatly improves the ability to measure and analyze particle interactions in the forward direction. Throughout Run-22, the forward upgrades demonstrated exceptional performance, seamlessly collecting data. The forward upgrades at STAR are set to continue data collection efforts in parallel with sPHENIX through Run-25, significantly enhancing our understanding of QCD physics in the forward region.

References

1. J. J. Thomson. [XL. Cathode Rays](#). *The London, Edinburgh, and Dublin Philosophical Magazine and Journal of Science* **44**, 293 (1897).
2. E. Rutherford. [Bakerian Lecture: Nuclear constitution of atoms](#). *Proc. R. Soc. Lond. A* **97**, 374 (1920).
3. J. Chadwick. [The existence of a neutron](#). *Proc. R. Soc. Lond. A* **136**, 692 (1932).
4. B. Carithers & P. Grannis. Discovery of the top quark. *SLAC Beam Line* **25**. [SLAC Beam Line 25, 4 (1995)], 4 (1995).
5. S. L. Glashow. [Partial-symmetries of weak interactions](#). *Nuclear Physics* **22**, 579 (1961).
6. A. Salam & J. Ward. [Electromagnetic and weak interactions](#). *Physics Letters* **13**, 168 (1964).
7. S. Weinberg. [A Model of Leptons](#). *Phys. Rev. Lett.* **19**, 1264 (1967).
8. A. Maggiora. A.M.E.L.I.E. Apparatus for Muon Experimental Lifetime Investigation and Evaluation. arXiv: [2306.10712 \[physics.ed-ph\]](#).
9. P. W. Higgs. [Broken symmetries, massless particles and gauge fields](#). *Phys. Lett.* **12**, 132 (1964).
10. P. W. Higgs. [Broken Symmetries and the Masses of Gauge Bosons](#). *Phys. Rev. Lett.* **13**, 508 (1964).
11. F. Englert & R. Brout. [Broken Symmetry and the Mass of Gauge Vector Mesons](#). *Phys. Rev. Lett.* **13**, 321 (1964).
12. G. Aad *et al.* [Observation of a new particle in the search for the Standard Model Higgs boson with the ATLAS detector at the LHC](#). *Phys. Lett. B* **716**, 1. arXiv: [1207.7214 \[hep-ex\]](#) (2012).
13. S. Chatrchyan *et al.* [Observation of a new boson at a mass of 125 GeV with the CMS experiment at the LHC](#). *Physics Letters B* **716**, 30 (2012).
14. D. J. Gross & F. Wilczek. [Asymptotically Free Gauge Theories. I](#). *Phys. Rev. D* **8**, 3633 (1973).

15. D. J. Gross & F. Wilczek. [Ultraviolet Behavior of Non-Abelian Gauge Theories.](#) *Phys. Rev. Lett.* **30**, 1343 (1973).
16. G. Dissertori. *The Standard Theory of Particle Physics* 113 (WORLD SCIENTIFIC, 2016).
17. A. Andronic, P. Braun-Munzinger, K. Redlich & J. Stachel. [Decoding the phase structure of QCD via particle production at high energy.](#) *Nature* **561**, 321 (2018).
18. J. C. Collins & M. J. Perry. [Superdense Matter: Neutrons or Asymptotically Free Quarks?](#) *Phys. Rev. Lett.* **34**, 1353 (1975).
19. B. Jacak & P. Steinberg. [Creating the perfect liquid in heavy-ion collisions.](#) *Physics Today* **63**, 39. eprint: https://pubs.aip.org/physicstoday/article-pdf/63/5/39/16668397/39_1_online.pdf (2010).
20. F. Karsch. [Lattice results on QCD thermodynamics.](#) *Nucl. Phys. A* **698** (eds T. J. Hallman, D. E. Kharzeev, J. T. Mitchell & T. S. Ullrich) 199. arXiv: [hep-ph/0103314](https://arxiv.org/abs/hep-ph/0103314) (2002).
21. A. Aprahamian *et al.* [Reaching for the horizon: The 2015 long range plan for nuclear science.](#) *The 2015 long range plan for nuclear science* (2015).
22. T. L. collaboration, R. Aaij, *et al.* [Centrality determination in heavy-ion collisions with the LHCb detector.](#) *Journal of Instrumentation* **17**, P05009 (2022).
23. <https://particlesandfriends.wordpress.com/2016/10/14/evolution-of-collisions-and-qgp/>.
24. J. D. Bjorken. [Highly relativistic nucleus-nucleus collisions: The central rapidity region.](#) *Phys. Rev. D* **27**, 140 (1983).
25. J. Adams *et al.* [Experimental and theoretical challenges in the search for the quark–gluon plasma: The STAR Collaboration’s critical assessment of the evidence from RHIC collisions.](#) *Nuclear Physics A* **757**, 102 (2005).
26. O. Y. Barannikova. *Probing collision dynamics at RHIC. 17th International Conference on Ultra Relativistic Nucleus-Nucleus Collisions (Quark Matter 2004)* (2004). arXiv: [nucl-ex/0403014](https://arxiv.org/abs/nuel-ex/0403014).
27. J. Cleymans & K. Redlich. [Chemical and thermal freeze-out parameters from 1A to 200A GeV.](#) *Phys. Rev. C* **60**, 054908 (1999).
28. J. Adams *et al.* [Experimental and theoretical challenges in the search for the quark gluon plasma: The STAR Collaboration’s critical assessment of the evidence from RHIC collisions.](#) *Nucl. Phys. A* **757**, 102. arXiv: [nucl-ex/0501009](https://arxiv.org/abs/nuel-ex/0501009) (2005).
29. [Elliptic flow of \$\pi\$, \$K\$, \$p\$ and \$\phi\$ in Pb-Pb collisions at the Large Hadron Collider.](#) *Proceedings of the Conference on Placeholder Title* (2016).

30. J. Adams *et al.* [Directed flow in Au+Au collisions at \$\sqrt{s_{NN}} = 62.4\$ GeV](#). *Phys. Rev. C* **73**, 034903 (2006).
31. L. V. Bravina *et al.* Collective effects in heavy-ion collisions. *Nucl. Phys. A* **566**, 461c (1994).
32. L. V. Bravina, L. P. Csernai, P. Levai & D. Strottman. Relativistic heavy-ion collisions. *Phys. Rev. C* **50**, 2161 (1994).
33. L. P. Csernai & D. Rohrlich. [Third flow component as QGP signal](#). *Phys. Lett. B* **458**, 454. arXiv: [nucl-th/9908034](#) (1999).
34. Z. W. Lin & C. M. Ko. [Partonic effects on the elliptic flow at relativistic heavy ion collisions](#). *Phys. Rev. C* **65**, 034904 (2002).
35. L. W. Chen & C. M. Ko. [Charm elliptic flow at RHIC](#). *Phys. Rev. C* **72**, 024906 (2005).
36. L. W. Chen. *Private communication*. Personal communication with X. L. Zhu in 2005. (2005).
37. H. Sorge. [Elliptical flow: A Signature for early pressure in ultrarelativistic nucleus-nucleus collisions](#). *Phys. Rev. Lett.* **78**, 2309. arXiv: [nucl-th/9610026](#) (1997).
38. S. A. Bass *et al.* [Microscopic models for ultrarelativistic heavy ion collisions](#). *Prog. Part. Nucl. Phys.* **41**, 255. arXiv: [nucl-th/9803035](#) (1998).
39. M. Bleicher *et al.* [Relativistic hadron hadron collisions in the ultrarelativistic quantum molecular dynamics model](#). *J. Phys. G* **25**, 1859. arXiv: [hep-ph/9909407](#) (1999).
40. X. L. Zhu. *Private communication*. Personal communication with X. L. Zhu in 2005. (2005).
41. J. Adams *et al.* [Azimuthal anisotropy in Au+Au collisions at \$\sqrt{s_{NN}} = 200\$ GeV](#). *Phys. Rev. C* **72**, 014904 (2005).
42. P. Huovinen *et al.* [Radial and elliptic flow at RHIC: further predictions](#). *Physics Letters B* **503**, 58 (2001).
43. S. A. Voloshin, A. M. Poskanzer & R. Snellings. [Collective phenomena in non-central nuclear collisions](#). *Landolt-Bornstein* **23** (ed R. Stock) 293. arXiv: [0809.2949 \[nucl-ex\]](#) (2010).
44. D. Molnar & S. A. Voloshin. [Elliptic flow at large transverse momentum from quark coalescence](#). *Phys. Rev. Lett.* **91**, 092301 (2003).
45. S. A. Voloshin. [Anisotropic flow](#). *Nucl. Phys. A* **715**, 379 (2003).

46. A. Adare *et al.* Enhanced production of direct photons in Au+Au collisions at $\sqrt{s_{NN}} = 200$ GeV and implications for the initial temperature. *Phys. Rev. Lett.* **104**, 132301. arXiv: 0804.4168 [nucl-ex] (2010).
47. C. Yang. Direct photon production in Au + Au collisions at $\sqrt{s_{NN}} = 200$ GeV at STAR. *Nucl. Phys. A* **931** (eds P. Braun-Munzinger, B. Friman & J. Stachel) 691. arXiv: 1408.2371 [hep-ex] (2014).
48. M. J. Russcher. Direct photons in d + Au and p + p collisions. *J. Phys. G* **34** (eds Y.-G. Ma *et al.*) S1033. arXiv: nucl-ex/0701071 (2007).
49. S. Turbide, R. Rapp & C. Gale. Photon production in relativistic nuclear collisions at SPS and RHIC energies. *Int. J. Mod. Phys. A* **19** (eds M. Frank & C. S. Kalman) 5351. arXiv: hep-ph/0408119 (2004).
50. A. Adare *et al.* Detailed measurement of the e^+e^- pair continuum in p + p and Au+Au collisions at $\sqrt{s_{NN}} = 200$ GeV and implications for direct photon production. *Phys. Rev. C* **81**, 034911. arXiv: 0912.0244 [nucl-ex] (2010).
51. J. Rafelski & B. Muller. Strangeness Production in the Quark - Gluon Plasma. *Phys. Rev. Lett.* **48**. [Erratum: *Phys.Rev.Lett.* 56, 2334 (1986)], 1066 (1982).
52. B. Abelev *et al.* Energy and system size dependence of meson production in Cu+Cu and Au+Au collisions. *Physics Letters B* **673**, 183 (2009).
53. T. Alber. Two-pion interferometry in central nucleus-nucleus collisions at the CERN SPS — Results from experiments NA35 and NA49. *Nuclear Physics A* **590**, 453 (1995).
54. P. Jones *et al.* Hadron yields and hadron spectra from the NA49 experiment. *Nuclear Physics A* **610**. Quark Matter '96, 188 (1996).
55. F. Siklér *et al.* Hadron production in nuclear collisions from the NA49 experiment at 158GeV/c · A. *Nuclear Physics A* **661**, 45 (1999).
56. C. Adler *et al.* Kaon production and kaon to pion ratio in Au+Au collisions at $s(NN)^{1/2} = 130$ -GeV. *Phys. Lett. B* **595**, 143. arXiv: nucl-ex/0206008 (2004).
57. J. Adams *et al.* Transverse-Momentum and Collision-Energy Dependence of High- p_T Hadron Suppression in Au + Au Collisions at Ultrarelativistic Energies. *Phys. Rev. Lett.* **91**, 172302 (2003).
58. J. Adams *et al.* Multistrange Baryon Production in Au-Au Collisions at $\sqrt{s_{NN}} = 130$ GeV. *Phys. Rev. Lett.* **92**, 182301 (2004).
59. C. Adler *et al.* Midrapidity Λ and $\bar{\Lambda}$ Production in Au + Au Collisions at $\sqrt{s_{NN}} = 130$ GeV. *Phys. Rev. Lett.* **89**, 092301 (2002).

60. A. Adare *et al.* *J/ψ* Production in $\sqrt{s_{NN}} = 200$ GeV Cu + Cu Collisions. *Phys. Rev. Lett.* **101**, 122301 (2008).
61. S. Chatrchyan *et al.* Observation of Sequential Υ Suppression in PbPb Collisions. *Phys. Rev. Lett.* **109**, 222301 (2012).
62. M. Gao. Debye screening in the QCD gluonic plasma. *Phys. Rev. D* **41**, 626 (1990).
63. T. Matsui & H. Satz. *J/ψ* Suppression by Quark-Gluon Plasma Formation. *Phys. Lett. B* **178**, 416 (1986).
64. J. D. Bjorken. Energy Loss of Energetic Partons in Quark - Gluon Plasma: Possible Extinction of High p(t) Jets in Hadron - Hadron Collisions. *Report number: FERMILAB-PUB-82-059-THY, FERMILAB-PUB-82-059-T* (1982).
65. M. Gyulassy & M. Plümer. Jet quenching in dense matter. *Physics Letters B* **243**, 432 (1990).
66. X.-N. Wang & M. Gyulassy. Gluon shadowing and jet quenching in A+A collisions at $\sqrt{s} = 200A$ GeV. *Phys. Rev. Lett.* **68**, 1480 (1992).
67. D. d. Enterría & B. Betz. *The Physics of the Quark-Gluon Plasma: Introductory Lectures* (eds S. Sarkar, H. Satz & B. Sinha) 285 (Springer Berlin Heidelberg, Berlin, Heidelberg, 2010).
68. Y. Mehtar-Tani. Jet structure in Heavy-Ion Collisions – A theory overview. *Nuclear and Particle Physics Proceedings* **276-278**. 7th International Conference on Hard and Electromagnetic Probes of High Energy Nuclear Collisions, 41 (2016).
69. K. Aamodt *et al.* Suppression of Charged Particle Production at Large Transverse Momentum in Central Pb-Pb Collisions at $\sqrt{s_{NN}} = 2.76$ TeV. *Phys. Lett. B* **696**, 30. arXiv: 1012.1004 [nucl-ex] (2011).
70. R. Esha. *Exploring the Critical Phenomenon in the QCD Phase Diagram at STAR*. 2019. PhD thesis (PhD Thesis, 2019).
71. <https://science.osti.gov/np/Facilities/User-Facilities/RHIC>.
72. <https://www.crystalinks.com/RHICmap.jpg>.
73. L. Adamczyk *et al.* Global Λ hyperon polarization in nuclear collisions: evidence for the most vortical fluid. *Nature* **548**, 62. arXiv: 1701.06657 [nucl-ex] (2017).
74. M. Anderson *et al.* A description of the STAR TPC. *Nucl. Instrum. Meth. A* **499**, 659 (2003).
75. H. Wieman *et al.* Development of a high-resolution TPC for heavy ion physics. *IEEE Trans. Nuc. Sci.* **44**, 671 (1997).

76. J. Thomas *et al.* [The STAR silicon vertex detector \(SVD\)](#). *Nucl. Instrum. Meth. A* **478**, 166 (2002).
77. M. Anderson *et al.* [The Star time projection chamber: A Unique tool for studying high multiplicity events at RHIC](#). *Nucl. Instrum. Meth. A* **499**, 659. arXiv: [nucl-ex/0301015](#) (2003).
78. H. Bichsel. [A method to improve tracking and particle identification in TPCs and silicon detectors](#). *Nucl. Instrum. Meth. A* **562**, 154 (2006).
79. W. M. Yao *et al.* [Review of Particle Physics](#). *J. Phys. G* **33**, 1 (2006).
80. W. Llope *et al.* [The TOFp/pVPD time-of-flight system for STAR](#). *Nuclear Instruments and Methods in Physics Research Section A: Accelerators, Spectrometers, Detectors and Associated Equipment* **522**, 252 (2004).
81. B. Bonner *et al.* [A single Time-of-Flight tray based on multigap resistive plate chambers for the STAR experiment at RHIC](#). *Nucl. Instrum. Meth. A* **508** (eds P. Fonte, M. Fraga, S. P. Ratti & R. Santonico) 181 (2003).
82. J. Schambach. *Proposed STAR Time of Flight Readout Electronics and DAQ*. 2003. arXiv: [nucl-ex/0305035 \[nucl-ex\]](#).
83. J. Landgraf *et al.* [An overview of the STAR DAQ system](#). *Nuclear Instruments and Methods in Physics Research Section A: Accelerators, Spectrometers, Detectors and Associated Equipment* **499**. *The Relativistic Heavy Ion Collider Project: RHIC and its Detectors*, 762 (2003).
84. C. Adler *et al.* [The RHIC zero degree calorimeters](#). *Nuclear Instruments and Methods in Physics Research Section A: Accelerators, Spectrometers, Detectors and Associated Equipment* **470**, 488 (2001).
85. H. Appelshäuser, J. Bächler, *et al.* [Directed and Elliptic Flow in 158 GeV/Nucleon Pb + Pb Collisions](#). *Phys. Rev. Lett.* **80**, 4136 (1998).
86. B. I. Abelev *et al.* [System-Size Independence of Directed Flow Measured at the BNL Relativistic Heavy-Ion Collider](#). *Phys. Rev. Lett.* **101**, 252301 (2008).
87. https://www.star.bnl.gov/public/bbc/geom/front_view.html.
88. W. Llope *et al.* [The TOFp/pVPD time-of-flight system for STAR](#). *Nuclear Instruments and Methods in Physics Research Section A: Accelerators, Spectrometers, Detectors and Associated Equipment* **522**, 252 (2004).
89. M. Beddo *et al.* [The STAR Barrel Electromagnetic Calorimeter](#). *Nuclear Instruments and Methods in Physics Research Section A: Accelerators, Spectrometers, Detectors and Associated Equipment* **499**. *The Relativistic Heavy Ion Collider Project: RHIC and its Detectors*, 725 (2003).

90. C. Allgower *et al.* [The STAR endcap electromagnetic calorimeter](#). *Nuclear Instruments and Methods in Physics Research Section A: Accelerators, Spectrometers, Detectors and Associated Equipment* **499**. The Relativistic Heavy Ion Collider Project: RHIC and its Detectors, 740 (2003).
91. I. Arsene *et al.* [Quark gluon plasma and color glass condensate at RHIC? The Perspective from the BRAHMS experiment](#). *Nucl. Phys. A* **757**, 1. arXiv: [nucl-ex/0410020](#) (2005).
92. C. Shen & U. Heinz. [The road to precision: Extraction of the specific shear viscosity of the quark-gluon plasma](#). *Nucl. Phys. News* **25**, 6. arXiv: [1507.01558 \[nucl-th\]](#) (2015).
93. B. B. Back *et al.* [The PHOBOS perspective on discoveries at RHIC](#). *Nucl. Phys. A* **757**, 28. arXiv: [nucl-ex/0410022](#) (2005).
94. L. Adamczyk *et al.* [Inclusive charged hadron elliptic flow in Au + Au collisions at \$\sqrt{s_{NN}} = 7.7\text{--}39\$ GeV](#). *Phys. Rev. C* **86**, 054908 (2012).
95. L. Adamczyk *et al.* [Elliptic flow of identified hadrons in Au+Au collisions at \$\sqrt{s_{NN}} = 7.7\text{--}62.4\$ GeV](#). *Phys. Rev. C* **88**, 014902 (2013).
96. L. Adamczyk *et al.* [Observation of an Energy-Dependent Difference in Elliptic Flow between Particles and Antiparticles in Relativistic Heavy Ion Collisions](#). *Phys. Rev. Lett.* **110**, 142301 (2013).
97. L. Adamczyk *et al.* [Beam-Energy Dependence of the Directed Flow of Protons, Antiprotons, and Pions in Au+Au Collisions](#). *Phys. Rev. Lett.* **112**, 162301 (2014).
98. L. Adamczyk *et al.* [Beam-Energy Dependence of Charge Separation along the Magnetic Field in Au + Au Collisions at RHIC](#). *Phys. Rev. Lett.* **113**, 052302 (2014).
99. L. Adamczyk *et al.* [Probing parton dynamics of QCD matter with \$\Omega\$ and \$\phi\$ production](#). *Phys. Rev. C* **93**, 021903 (2016).
100. L. Adamczyk *et al.* [Bulk properties of the medium produced in relativistic heavy-ion collisions from the beam energy scan program](#). *Phys. Rev. C* **96**, 044904 (2017).
101. C. Aidala *et al.* [Measurements of azimuthal anisotropy and charged-particle multiplicity in \$d + Au\$ collisions at \$\sqrt{s_{NN}} = 200, 62.4, 39,\$ and \$19.6\$ GeV](#). *Phys. Rev. C* **96**, 064905 (2017).
102. A. Adare *et al.* [Transverse energy production and charged-particle multiplicity at midrapidity in various systems from \$\sqrt{s_{NN}} = 7.7\$ to \$200\$ GeV](#). *Phys. Rev. C* **93**, 024901 (2016).

103. A. Adare *et al.* Measurement of higher cumulants of net-charge multiplicity distributions in Au + Au collisions at $\sqrt{s_{NN}} = 7.7 - 200$ GeV. *Phys. Rev. C* **93**, 011901 (2016).
104. A. Adare *et al.* Evolution of π^0 Suppression in Au + Au Collisions from $\sqrt{s_{NN}} = 39$ to 200 GeV. *Phys. Rev. Lett.* **109**, 152301 (2012).
105. C. Adler *et al.* The RHIC zero degree calorimeter. *Nucl. Instrum. Meth. A* **470**, 488. arXiv: [nucl-ex/0008005](https://arxiv.org/abs/nuc1-ex/0008005) (2001).
106. W. J. Llope *et al.* The STAR Vertex Position Detector. *Nucl. Instrum. Meth. A* **759**, 23. arXiv: [1403.6855 \[physics.ins-det\]](https://arxiv.org/abs/1403.6855) (2014).
107. J. Abele *et al.* The laser system for the STAR time projection chamber. *Nucl. Instrum. Meth. A* **499**, 692 (2003).
108. L. Adamczyk *et al.* Bulk Properties of the Medium Produced in Relativistic Heavy-Ion Collisions from the Beam Energy Scan Program. *Phys. Rev. C* **96**, 044904. arXiv: [1701.07065 \[nucl-ex\]](https://arxiv.org/abs/1701.07065) (2017).
109. L. Adamczyk *et al.* Azimuthal Anisotropy in U + U and Au + Au Collisions at RHIC. *Phys. Rev. Lett.* **115**, 222301 (2015).
110. G. Nigmatkulov. Recent STAR Results from Heavy-Ion and Polarized Proton Programs. *EPJ Web Conf.* **222** (eds D. Melikhov & I. Volobuev) 01004 (2019).
111. <https://drupal.star.bnl.gov/STAR/blog/tnonaka/centrality-definitions-2018>.
112. V. Fine & P. Nevski. *Proc. CHEP 2000* **143** (2000).
113. B. I. Abelev *et al.* Systematic Measurements of Identified Particle Spectra in pp , d^+ Au and Au+Au Collisions from STAR. *Phys. Rev. C* **79**, 034909. arXiv: [0808.2041 \[nucl-ex\]](https://arxiv.org/abs/0808.2041) (2009).
114. E. Schnedermann, J. Sollfrank & U. W. Heinz. Thermal phenomenology of hadrons from 200-A/GeV S+S collisions. *Phys. Rev. C* **48**, 2462. arXiv: [nucl-th/9307020](https://arxiv.org/abs/nuc1-th/9307020) (1993).
115. J. Adams *et al.* Identified particle distributions in pp and Au+Au collisions at $s(NN)^{(1/2)} = 200$ GeV. *Phys. Rev. Lett.* **92**, 112301. arXiv: [nucl-ex/0310004](https://arxiv.org/abs/nuc1-ex/0310004) (2004).
116. Y. Akiba *et al.* Particle production in Au + Au collisions from BNL E866. *Nuclear Physics A* **610**. Quark Matter '96, 139 (1996).
117. L. Ahle *et al.* Particle production at high baryon density in central Au+Au reactions at 11.6A GeV/c. *Phys. Rev. C* **57**, R466 (1998).

118. L. Ahle *et al.* An excitation function of K^- and K^+ production in Au+Au reactions at the AGS. *Physics Letters B* **490**, 53 (2000).
119. J. Barrette *et al.* Proton and pion production in Au+Au collisions at 10.8A GeV/c. *Phys. Rev. C* **62**, 024901 (2000).
120. L. Ahle *et al.* Proton and deuteron production in Au+Au reactions at 11.6A GeV/c. *Phys. Rev. C* **60**, 064901 (1999).
121. L. Ahle *et al.* Centrality dependence of kaon yields in Si + A and Au+Au collisions at relativistic energies. *Phys. Rev. C* **60**, 044904 (1999).
122. L. Ahle *et al.* An excitation function of K^- and K^+ production in Au+Au reactions at the AGS. *Physics Letters B* **490**, 53 (2000).
123. I. G. Bearden *et al.* Pseudorapidity Distributions of Charged Particles from Au+Au Collisions at the Maximum RHIC Energy, $\sqrt{s_{NN}} = 200\text{GeV}$. *Phys. Rev. Lett.* **88**, 202301 (2002).
124. S. V. Afanasiev *et al.* Energy dependence of pion and kaon production in central Pb+Pb collisions. *Phys. Rev. C* **66**, 054902 (2002).
125. T. Anticic *et al.* Energy and centrality dependence of deuteron and proton production in Pb + Pb collisions at relativistic energies. *Phys. Rev. C* **69**, 024902 (2004).
126. C. Alt *et al.* Energy and centrality dependence of \bar{p} and p production and the $\bar{\Lambda}/\bar{p}$ ratio in Pb+Pb collisions between 20A GeV and 158A GeV. *Phys. Rev. C* **73**, 044910 (2006).
127. C. Alt *et al.* Pion and kaon production in central Pb+Pb collisions at 20A and 30A GeV: Evidence for the onset of deconfinement. *Phys. Rev. C* **77**, 024903 (2008).
128. B. I. Abelev *et al.* Identified particle production, azimuthal anisotropy, and interferometry measurements in Au + Au collisions at $\sqrt{s_{NN}} = 9.2\text{ GeV}$. *Phys. Rev. C* **81**, 024911 (2010).
129. B. I. Abelev *et al.* Systematic measurements of identified particle spectra in pp , $d + \text{Au}$, and $\text{Au} + \text{Au}$ collisions at the STAR detector. *Phys. Rev. C* **79**, 034909 (2009).
130. S. S. Adler *et al.* Systematic studies of the centrality and $\sqrt{s_{NN}}$ dependence of the $dE_T/d\eta$ and $dN_{\text{ch}}/d\eta$ in heavy ion collisions at midrapidity. *Phys. Rev. C* **71**, 034908 (2005).
131. M. Kaneta & N. Xu. Centrality dependence of chemical freeze-out in Au+Au collisions at RHIC. 17th International Conference on Ultra Relativistic Nucleus-Nucleus Collisions (Quark Matter 2004) (2004). arXiv: [nucl-th/0405068](https://arxiv.org/abs/nucl-th/0405068).

132. J. Cleymans *et al.* Centrality dependence of thermal parameters deduced from hadron multiplicities in Au + Au collisions at $\sqrt{s(NN)}^{1/2} = 130\text{-GeV}$. *Phys. Rev. C* **71**, 054901. arXiv: hep-ph/0409071 (2005).
133. Y. Akiba *et al.* Particle production in Au + Au collisions from BNL E866. *Nuclear Physics A* **610**. Quark Matter '96, 139 (1996).
134. L. Ahle *et al.* Proton and deuteron production in Au + Au reactions at 11.6/A-GeV/c. *Phys. Rev. C* **60**, 064901 (1999).
135. L. Ahle *et al.* Excitation function of K+ and pi+ production in Au + Au reactions at 2/A-GeV to 10/A-GeV. *Phys. Lett. B* **476**, 1. arXiv: nucl-ex/9910008 (2000).
136. J. Barrette *et al.* Proton and pion production in Au + Au collisions at 10.8A-GeV/c. *Phys. Rev. C* **62**, 024901. arXiv: nucl-ex/9910004 (2000).
137. L. Ahle *et al.* Centrality dependence of kaon yields in Si + A and Au + Au collisions at the AGS. *Phys. Rev. C* **60**, 044904. arXiv: nucl-ex/9903009 (1999).
138. L. Ahle *et al.* An Excitation function of K- and K+ production in Au + Au reactions at the AGS. *Phys. Lett. B* **490**, 53. arXiv: nucl-ex/0008010 (2000).
139. J. L. Klay *et al.* Longitudinal flow from 2-A-GeV to 8-A-GeV Au+Au collisions at the Brookhaven AGS. *Phys. Rev. Lett.* **88**, 102301. arXiv: nucl-ex/0111006 (2002).
140. S. V. Afanasiev *et al.* Energy dependence of pion and kaon production in central Pb + Pb collisions. *Phys. Rev. C* **66**, 054902. arXiv: nucl-ex/0205002 (2002).
141. T. Anticic *et al.* Energy and centrality dependence of deuteron and proton production in Pb + Pb collisions at relativistic energies. *Phys. Rev. C* **69**, 024902 (2004).
142. C. Alt *et al.* Energy and centrality dependence of anti-p and p production and the anti-Lambda/anti-p ratio in Pb+Pb collisions between 20/A-GeV and 158/A-GeV. *Phys. Rev. C* **73**, 044910 (2006).
143. C. Alt *et al.* Pion and kaon production in central Pb + Pb collisions at 20-A and 30-A-GeV: Evidence for the onset of deconfinement. *Phys. Rev. C* **77**, 024903. arXiv: 0710.0118 [nucl-ex] (2008).
144. B. I. Abelev *et al.* Identified particle production, azimuthal anisotropy, and interferometry measurements in Au+Au collisions at $\sqrt{s(NN)}^{1/2} = 9.2\text{-GeV}$. *Phys. Rev. C* **81**, 024911. arXiv: 0909.4131 [nucl-ex] (2010).
145. B. Abelev *et al.* Centrality dependence of π , K, p production in Pb-Pb collisions at $\sqrt{s_{NN}} = 2.76\text{ TeV}$. *Phys. Rev. C* **88**, 044910. arXiv: 1303.0737 [hep-ex] (2013).
146. E. V. Shuryak. *Physics Reports* **61**, 71 (1980).

147. K. Adcox *et al.* [Formation of dense partonic matter in relativistic nucleus-nucleus collisions at RHIC: Experimental evaluation by the PHENIX collaboration.](#) *Nucl. Phys. A* **757**, 184. arXiv: [nucl-ex/0410003](#) (2005).
148. B. Back *et al.* [The PHOBOS perspective on discoveries at RHIC.](#) *Nuclear Physics A* **757**. First Three Years of Operation of RHIC, 28 (2005).
149. S. Ejiri. [Canonical partition function and finite density phase transition in lattice QCD.](#) *Phys. Rev. D* **78**, 074507 (2008).
150. Z.-W. Lin *et al.* [Multiphase transport model for relativistic heavy ion collisions.](#) *Phys. Rev. C* **72**, 064901 (2005).
151. E. Schnedermann, J. Sollfrank & U. Heinz. [Thermal phenomenology of hadrons from 200A GeV S+S collisions.](#) *Phys. Rev. C* **48**, 2462 (1993).
152. Y. J. Ye *et al.* [\$\Omega\$ and \$\phi\$ in Au + Au collisions at \$\sqrt{s_{NN}} = 200\$ and 11.5 GeV from a multiphase transport model.](#) *Chin. Phys. C* **41**, 084101. arXiv: [1706.00894 \[nucl-th\]](#) (2017).
153. A. Nandi, L. Kumar & N. Sharma. [Constraining the particle production mechanism in Au+Au collisions at \$\sqrt{s_{NN}} = 7.7, 27,\$ and 200 GeV using a multiphase transport model.](#) *Phys. Rev. C* **102**, 024902 (2020).
154. K. Tiwari & M. Nasim. [Constraining input parameters of AMPT model with meson production.](#) *Nuclear Physics A* **999**, 121751 (2020).
155. X.-N. Wang & M. Gyulassy. [hijing: A Monte Carlo model for multiple jet production in pp, pA, and AA collisions.](#) *Phys. Rev. D* **44**, 3501 (1991).
156. B. Zhang. [ZPC 1.0.1: A Parton cascade for ultrarelativistic heavy ion collisions.](#) *Comput. Phys. Commun.* **109**, 193. arXiv: [nucl-th/9709009](#) (1998).
157. J. Xu & C. M. Ko. [Pb-Pb collisions at \$\sqrt{s_{NN}} = 2.76\$ TeV in a multiphase transport model.](#) *Phys. Rev. C* **83**, 034904 (2011).
158. B. Andersson, G. Gustafson, G. Ingelman & T. Sjostrand. [Parton Fragmentation and String Dynamics.](#) *Phys. Rept.* **97**, 31 (1983).
159. Y. He & Z.-W. Lin. [Improved quark coalescence for a multi-phase transport model.](#) *Phys. Rev. C* **96**, 014910 (2017).
160. K. Gopal, C. Jena & K. Nayak. [Energy dependence of particle production in Au+Au collisions at \$\sqrt{s_{NN}} = 7.7-200\$ GeV using a multiphase transport model.](#) arXiv: [2406.13520 \[nucl-th\]](#) (2024).
161. G. Wilk & Z. Włodarczyk. [Interpretation of the Nonextensivity Parameter \$q\$ in Some Applications of Tsallis Statistics and Lévy Distributions.](#) *Phys. Rev. Lett.* **84**, 2770 (2000).

162. J. Adam *et al.* Strange hadron production in Au + Au collisions at $\sqrt{s_{NN}} = 7.7, 11.5, 19.6, 27, \text{ and } 39 \text{ GeV}$. *Phys. Rev. C* **102**, 034909 (2020).
163. *Properties of QCD Matter at High Baryon Density* (eds X. Luo, Q. Wang, N. Xu & P. Zhuang) (Springer, 2022).
164. R. Lacasse *et al.* Hadron yields and spectra in Au+Au collisions at the AGS. *Nuclear Physics A* **610**. Quark Matter '96, 153 (1996).
165. L. Ahle *et al.* Particle production at high baryon density in central Au+Au reactions at 11.6A GeV/c. *Phys. Rev. C* **57**, R466 (1998).
166. L. Ahle *et al.* An excitation function of K⁻ and K⁺ production in Au+Au reactions at the AGS. *Physics Letters B* **490**, 53 (2000).
167. J. Barrette *et al.* Energy and charged particle flow in 10.8A GeV/c Au+Au collisions. *Phys. Rev. C* **55**, 1420 (1997).
168. L. Ahle *et al.* Proton and deuteron production in Au+Au reactions at 11.6A GeV/c. *Phys. Rev. C* **60**, 064901 (1999).
169. L. Ahle *et al.* Centrality dependence of kaon yields in Si + A and Au+Au collisions at relativistic energies. *Phys. Rev. C* **60**, 044904 (1999).
170. J. L. Klay *et al.* Longitudinal Flow of Protons from (2 – 8) A GeV Central Au + Au Collisions. *Phys. Rev. Lett.* **88**, 102301 (2002).
171. B. I. Abelev *et al.* Systematic measurements of identified particle spectra in pp, d + Au, and Au + Au collisions at the STAR detector. *Phys. Rev. C* **79**, 034909 (2009).
172. <https://drupal.star.bnl.gov/STAR/starnotes/public/sn0648>.
173. E.-C. Aschenauer *et al.* The RHIC Cold QCD Plan for 2017 to 2023: A Portal to the EIC. *arXiv:1602.03922 [nucl-ex]*. Preprint available on arXiv:1602.03922 [nucl-ex]. arXiv: 1602.03922 [nucl-ex].
174. J. Brandenburg. STAR Forward Rapidity Upgrade. *PoS HardProbes2020*, 179 (2021).
175. J. C. Collins. *Nucl. Phys. B* **396**, 161 (1993).
176. J. C. Collins, S. F. Heppelmann & G. A. Ladinsky. *Nucl. Phys. B* **420**, 565 (1994).
177. https://drupal.star.bnl.gov/STAR/files/TeChuan_DNP2019_v4.pdf.
178. https://drupal.star.bnl.gov/STAR/system/files/yezhenyu_STAR_20190808_v1.pdf.

179. I. Abt, D. Emeliyanov, I. Gorbounov & I. Kisel. [Cellular automaton and Kalman filter based track search in the HERA-B pattern tracker](#). *Nuclear Instruments and Methods in Physics Research Section A: Accelerators, Spectrometers, Detectors and Associated Equipment* **490**, 546 (2002).
180. I. Kisel. *Fast tracking in the CBM experiment. 11th Workshop on Electronics for LHC and Future Experiments (LECC 2005)* (2005), 78.
181. E. Prencipe. [Customization of the GENFIT2 Fitting Package in PANDA](#). *EPJ Web Conf.* **127** (eds R. Frühwirth, E. Brondolin, B. Kolbinger & W. Waltenberger) 00013 (2016).
182. T. Bilka *et al.* Implementation of GENFIT2 as an experiment independent track-fitting framework. arXiv: [1902.04405 \[physics.data-an\]](#) (2019).

